UNIVERSITY OF SOUTHAMPTON

FACULTY OF PHYSICAL SCIENCES AND ENGINEERING

Physics and Astronomy

Penetration of Gold Nanoparticles through the Skin

by

Rute Fabiana Martins Fernandes

Thesis for the degree of Doctor of Philosophy

September 2014

UNIVERSITY OF SOUTHAMPTON

ABSTRACT

Penetration of Gold Nanoparticles through the Skin

by

Rute Fabiana Martins Fernandes

The assessment of nanoparticle penetration through skin is of increasing importance not only to evaluate the toxicity associated with occupational or environmental exposure to nanoparticles, but also to design rules for the fabrication of new types of transdermal drug delivery or diagnostics approaches. While these have been the subject of much research, the lack of a systematic approach in the penetration experiments has created controversial results regarding whether nanoparticles do or not penetrate the skin.

The aim of the research presented in the thesis is to investigate the penetration of gold nanoparticles through human and mouse skin, focusing on the effect of surface charge, morphology and specific functionalisation. To study this, a penetration protocol using organ culture was designed and tested to assure the maintenance of the skin integrity in the course of our experiments. Skin samples incubated with gold nanoparticles were characterized for penetration by NPs using inductively coupled plasma atomic emission spectroscopy, transmission electron microscopy, energy-dispersive X-ray spectroscopy and photoluminescence microscopy. Furthermore, epithelial cell monolayers were exposed to the gold nanoparticles to evaluate the transport through the cellular barrier. Transmission electron microscopy, light microscopy and trans epithelial electric resistance were used to characterise the cell monolayers exposed to gold nanoparticles.

Results obtained are important to enhance our understanding of the interaction of gold nanoparticles with skin, providing valuable information for the design of new nanoparticle-based transdermal delivery systems.

Table of Contents

List of figures

List of schemes

List of tables

DECLARATION OF AUTHORSHIP

I, Rute Fabiana Martins Fernandes, declare that this thesis and the work presented in it are my own and has been generated by me as the result of my own original research.

Penetration of Gold Nanoparticles through the Skin

I confirm that:

1. This work was done wholly or mainly while in candidature for a research degree at this University;
2. Where any part of this thesis has previously been submitted for a degree or any other qualification at this University or any other institution, this has been clearly stated;
3. Where I have consulted the published work of others, this is always clearly attributed;
4. Where I have quoted from the work of others, the source is always given. With the exception of such quotations, this thesis is entirely my own work;
5. I have acknowledged all main sources of help;
6. Where the thesis is based on work done by myself jointly with others, I have made clear exactly what was done by others and what I have contributed myself;
7. Parts of this work have been published as:

Fernandes, R.; Smyth N.; Kanaras, A. G. (2014). Interactions of gold nanoparticles with biological structures. Proc. SPIE 8955-25, *Colloidal Nanoparticles for Biomedical Applications IX*, 8955.

Fernandes, R.; Smyth, N. R.; Muskens, O. L.; Nitti, S.; Heuer-Juengemann, A.; Ardern-Jones, M.; Kanaras, A. G.. (2014) Interactions of Skin with Gold Nanoparticles of Different Surface Charge, Shape and Functionality. *Small*. (Accepted)

Signed: .....

Date: .....

Acknowledgements

The contents of this thesis are the product of the efforts of many people, to whom I would like to thank, though I can only name a few in the acknowledgments:

Firstly I would like to thank Dr. Antonios Kanaras, for giving me the opportunity to work on this interesting project, and for his guidance and supervision.

I also want to express my deepest gratitude to Dr. Neil Smyth for sharing with me his experience in the skin field, for the discussions especially in the time of new ideas and difficulties and for spending a lot of effort and time on this work. His interest and insightful support had a considerable impact on the success of this project.

I would like to thank Dr. Otto L. Muskens for assembling the PL microscopy setup and also his inputs and constructive comments on my work.

I wish to thank Dr. Anton Page, Patricia Goggin and Dr. David Johnston for their technical assistance, constant support and insightful advices. I also thank Patricia Goggin for the EDX analysis.

I am grateful to Dr. Peter Lackie for letting me use his laboratory facility and equipment.

I must thank Dr. Micheal Ardern-Jones for the supply of human skin and Simone Nitti for the ICP-AES measurements.

I would also like to express my gratitude to Dr. Liberato Manna, at the IIT in Genoa, for giving me the opportunity to work in his group.

I must acknowledge the University of Southampton, in particular physics and Astronomy, for the Mayflower scholarship.

I would like to thank my entire working group, for always acting like a team and helping in numerous ways, and also all my friends who helped me, in one way, or another.

I would like to specially thank Amelie Heuer-Jungemann for her constant support through all the stresses, struggles, and for always believing in me. I was very lucky to have her as colleague and most of all, to have her as a friend.

Finally, I am short of words for the immeasurable support of my parents and my brother. I hope they understand the importance they had, and the inspiration and strength they gave me to complete this work.

Definitions and Abbreviations

Abbreviation	Definition
BSPP	Bis(p-sulfonatophenyl)phenylphosphine dihydrate dipotassium
CALNN	cysteine-alanine-leucine-asparagine-asparagine
$CALNNR_7$	cysteine-alanine-leucine-asparagine-asparagine-arginine-arginine-arginine-arginine-arginine-arginine-arginine
CALNNTat	cysteine-alanine-leucine-asparagine-asparagine-glycine-arginine-lysine-lysine-arginine-arginine-glutamine-arginine-arginine-arginine-proline-glutamine
CPP	Cell-penetrating peptide
CTAB	Hexadecyltrimethylammonium bromide
DLS	Dynamic light scattering
DMEM	Dulbecco's modified Eagle's medium
EDTA	Ethylenediaminetetraacetic acid
EDX	Energy-dispersive X-ray spectroscopy
FBS	Fetal bovine serum
g	Gravitational acceleration
ICP-AES	Inductively coupled plasma atomic emission spectroscopy
JAMs	Junctional adhesion molecules
LM	Light microscopy

MDCK	Madin-Darby canine kidney
Mw	Molecular weight
NP	Nanoparticle
NR	Nanorod
NS	Nanosphere
PBS	Phosphate buffered saline
PEG	Polyethylene glycol
PIPES	Piperazine-N,N′-bis(2-ethanesulfonic acid)
PL	Photoluminescence
ppm	Part per million
rpm	Rotation per minute
RPMI	Roswell Park Memorial Institute
SC	Stratum corneum
SE	Standard Error
SH-PEG-COOH	Alpha-Thio-omega-carboxy polyethylene glycol
SH-PEG-NH_2	Alpha-Amino-omega-mercapto polyethylene glycol hydrochloride
TEER	Trans Epithelial Electric Resistance
TEM	Transmission electron microscopy
Tween20	Polyethylene glycol sorbitan monolaurate

UV	Ultraviolet
ZO	Zonula occludens

Chapter 1 Introduction

Nanotechnology is a rapidly growing field of research with an increasing impact on our everyday lives. The potential of nanoparticles (NPs) to penetrate the skin has made their study highly topical. The assessment of NP penetration through skin is of increasing importance for three major reasons: i) to evaluate NP toxicity associated with their use in consumer products, specifically in the cosmetic industry; ii) the health risk of those exposed to NPs in an industrial or research environment; iii) to design rules for the fabrication of new types of transdermal drug delivery or diagnostic approaches.

While these have been the subject of much research, the lack of a systematic approach in the penetration experiments has created controversial results regarding whether NPs do or not penetrate the skin.[1] Parameters such as skin type and condition (*e.g.* intact skin or skin either chemically or mechanically treated to enhance penetration), skin surface application area, exposure time, skin integrity maintenance during the experiment, galenic formulation (*e.g.* solvent, emulsion) and NP concentration and type (*e.g.* material, size, shape and surface functionalisation) all play key roles in the evaluation of NP penetration through the skin and must be considered in order to obtain consistent results.

Therefore, the overarching goal of the present work is to investigate the effect of the charge, shape and functionalization of the NPs in their penetration through skin, using a well-designed skin penetration experiment.

Among the inorganic nanoparticles, gold NPs were chosen based on their unique physicochemical properties, their relatively easy modification in terms

of size, topology and surface charge and their ability to be functionalise with targeting ligands. Seven types of gold NPs synthesized and fully characterized before being used in the penetration experiments. Spherical gold NPs (15 nm, diameter) and rod-shaped gold NPs (20 x 55 nm, width x length) were synthesised and coated with thiol-containing polyethylene glycol (PEG) molecules, with either an amino (positively charged) or a carboxyl (negatively charged) termini. Furthermore, spherical gold NSs (15 nm, diameter) were functionalised with three different peptides: cysteine-alanine-leucine-asparagine-asparagine (CALNN) and two CALNN-containing cell-penetrating peptides (CPPs), cysteine-alanine-leucine-asparagine-asparagine-glycine-arginine-lysine-lysine-arginine-arginine-glutamine-arginine-arginine-arginine-proline-glutamine (CALNNTat) and cysteine-alanine-leucine-asparagine-asparagine-arginine-arginine-arginine-arginine-arginine-arginine-arginine ($CALNNR_7$).

In the present thesis, the skin penetration experiments were performed using excised human skin, as the gold standard for ex vivo skin penetration, and hairless mouse skin. This allowed comparison between the penetration through human and animal skin. Because the skin integrity is considered crucial in skin penetration studies, the penetration setups for both human and mouse skin were designed and tested to ensure the maintenance of the skin integrity in the course of our experiments.

Skin samples incubated with gold NPs were characterized for penetration by NPs using a wide range of techniques, namely Transmission electron microscopy (TEM), energy-dispersive X-ray spectroscopy (EDX), inductively coupled plasma atomic emission spectroscopy (ICP-AES) and photoluminescence (PL) microscopy.

Furthermore, the tight junctions of an epithelial cell monolayer were exposed to the same types of gold NPs to evaluate the transport through the cellular barrier. TEM, light microscopy (LM) and (trans epithelial electric resistance) TEER were used to characterise the cell monolayers exposed to gold NPs.

Findings obtained from this work are important for a better understanding of the interaction of NPs with the skin. It was shown that the penetration behaviour of gold NPs was dependent on their physicochemical characteristics: size, shape and surface functionalization, with the latter being the most

significant factor. This can be applied on the designing of topical and transdermal delivery nanocarriers for biomedical, pharmaceutical and cosmetic applications. Additionally, results here presented are of high importance for the toxicology field, either related with occupational or environmental exposure.

1.1 Thesis outline

Chapter 2 – comprises a theoretical review of the skin structure and function, as well as of the theoretical background behind the synthesis of gold NPs. This chapter also contains a summary of the recent evidence on whether inorganic NPs penetrate the skin, discussing the pilot studies in the area, and an overview of the factors that may affect the NPs penetration. Chapter 3 – describes in detail the experimental protocols and techniques used in conducting this research. Chapter 4 – covers the research related with the colloidal gold NPs, from their synthesis and functionalisation to their characterization by different analytical techniques. Chapter 5 – comprises the results of the study of the interactions of gold NPs with Madin-Darby canine kidney-II (MDCK-II) cell monolayers. Chapter 6 – is dedicated to the investigation of the penetration of gold NPs through human and mouse skin. It comprises the results of the research on skin penetration by gold NPs. Includes the assessment of the penetration setups for the maintenance of skin integrity and TEM, EDX, ICP-AES and PL microscopy analysis of the skin samples exposed to gold NPs. Chapter 7 – contains a synopsis of the important findings of the present research and recommendations for future work.

Chapter 2 Background, context and state-of-art

2.1 Skin

2.1.1 Structure and function

The skin is the external membranous integument of vertebrates. Although it has many secondary roles such as in temperature regulation, its primary function is the maintenance of the epidermal barrier: this acts both in an inside out manner, to prevent water loss; and an outside-in way, to protect the body from environmental insults and pathogenic challenges.

Skin has a multilayered architecture consisting of the dermis, a collagenous connective tissue layer, and an outer epidermis, which differentiates to an outermost SC, which is metabolically inert and provides the skin with its remarkable barrier properties. Skin appendages (such as hairs, fingernails, sebaceous and sweat glands) develop as specializations of the epidermis (Figure 2.1). Both dermis and epidermis alter their thickness with the age and sex of the individual and with the region of the body.[2]

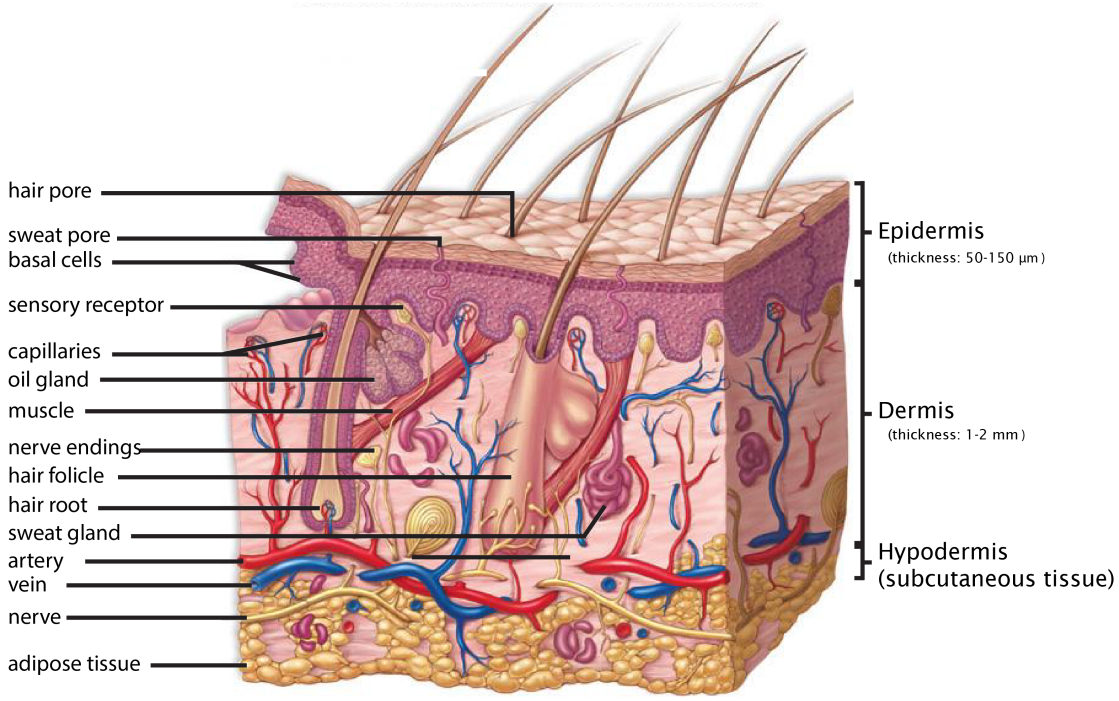

Figure 2.1 Schematic diagram of human skin.

The dermis is the innermost portion of the skin. Although it is vascularized, and provides nutrients and removes waste products to and from the epidermis, it is relatively acellular being mostly populated by fibroblasts. It consists mainly of extracellular matrix in a loose connective tissue with fibrillar collagens, primarily collagens type I and III with lesser amounts of non-fibrillar FACIT collagen types (V, VI, and XII).[3] These molecules give the tensile strength to the skin. They are embedded into a water retaining gel produced by glycosaminoglycans and proteoglycan complexes, predominantly the large and highly sugar substituted molecule versican. These molecules carry highly negatively charged sulphated sugar groups, which become hydrated and thus provide turgor and this along with elastin proteins gives compressive strength to the skin.

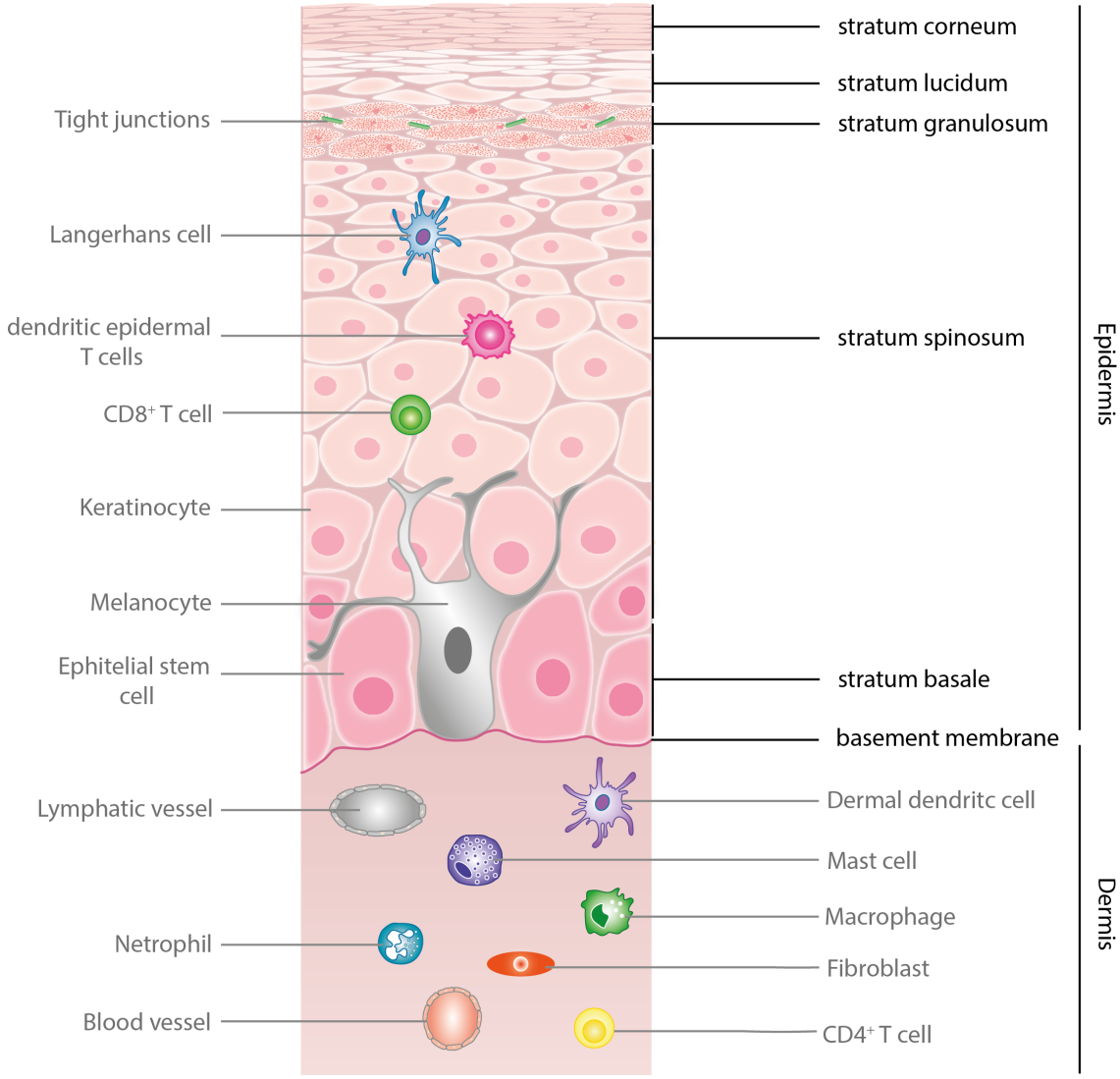

Figure 2.2 Schematic illustration of the different cells populating the skin.

The dermis is separated from the epidermis by the skin basement membrane; this is a ~100 nm thick highly defined form of extracellular matrix acting as a functional attachment site for the epidermis.[4] It consists of the network forming collagen IV, the cell adhesion molecule laminin, and the heparin sulphate containing proteoglycan perlecan. This results in a high negative charge density in this structure.

The basement membrane is directly below the epidermis. The skin epidermis is a multi-layered (stratified) epithelium composed primarily of keratinocytes, which synthesize keratins, the intermediate filament proteins, which give the epidermis its toughness. Unlike the dermis there is little if any extracellular matrix in the epidermis.[5]

The basal cells, which are in contact with the basement membrane, include epidermal stem cells; these are responsible for maintaining the proliferative potential of the epidermis. These cells actively divide and in doing so leave their contact from the basement membrane, this event blocks further division and induces the terminal differentiation of the keratinocytes. The keratinocytes undergo a highly regulated differentiation process; with the cells directly above the basal layers expressing many desmosomes giving them a spinous appearance (spinous layer) when prepared for LM. As the cells are pushed further superficially, they express keratohyalin granules. In this the granular layer the cells start to lose their nucleus and cytoplasmic organelles, through a degradative mechanisms that involves partial activation of the machinery of apoptosis. These cells express high levels of tranglutaminase enzymes (also seen in apoptosis) and disulphide isomerase, which respectively form isopeptide and disulphide cross-links between intracellular proteins, so forming a strong covalently linked protein network. This has a result the condensing of the cell structure and in this way the cells are transformed into the keratinized squames, *i.e* the resilient dead (methabolically inactive) corneocytes of the SC.

During the latter stages of differentiation there are also changes in the plasma membrane, the bilayer being gradually lost, the cells membrane in the granular layer containing ceramide, rather than membrane phospholipids (Figure 2.3). These relatively uncharged lipids are secreted at the surface of the cells where they form repeating layers in palisade-like structures and are maintained at the cell surface by the action of trangluaminases, which cross-link the ceremides to the condensed protein matrix of the cell, this produces the “so-called” cornified cell envelope observed in the SC. This is quite different in structure and components to other cell membranes and is essential for the barrier function of the skin. Unlikely most plasma membrane phospholipids, the corneocyte ceramide’s tail is fully saturated (Figure 2.3) and so forms a very stable semi-

crystalline structure in the cell membrane, which acts as a far greater barrier for water loss when compared to the conventional plasma membrane.

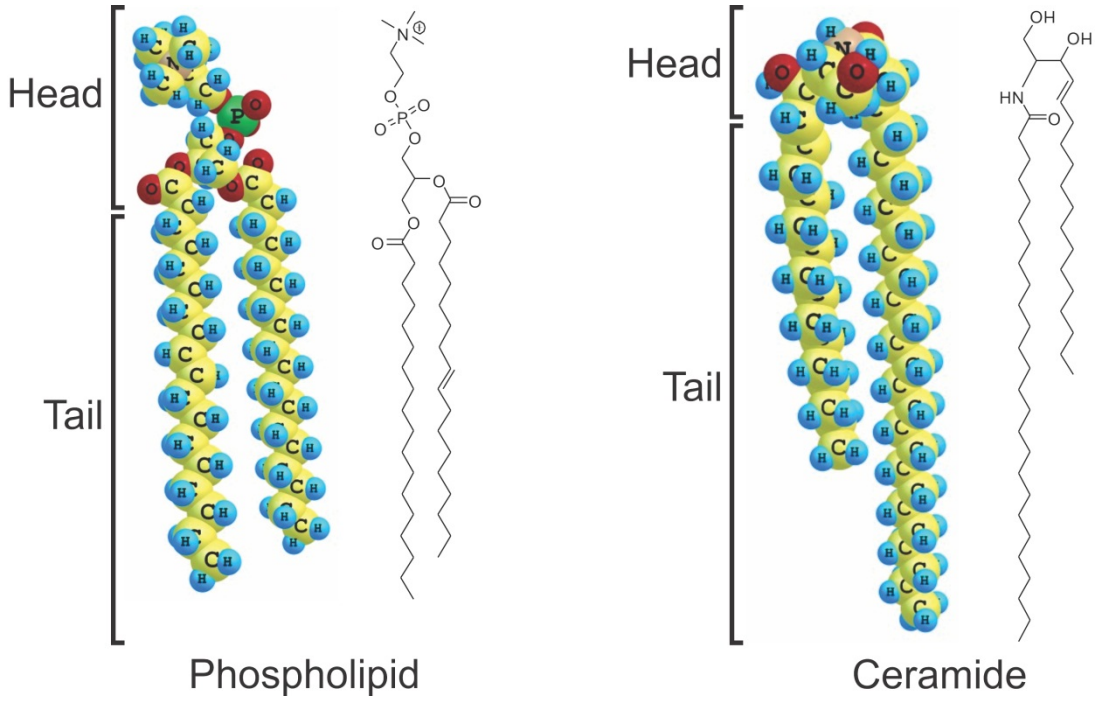

Figure 2.3 Space-filling representative models and the respective chemical structures of a phospholipid (left had side) and a ceramide (right hand side) with hydrophilic (slightly polar) head and hydrophobic fatty acid tail.

Ceramides account for approximately 50% of the total stratum corneum (SC) lipid mass and are crucial for the lamellar organization of the barrier. The other lipids in the SC are cholesterol and free fatty acids, comprising approximately 25% and 15% of the total lipid content, respectively. An alteration of the concentration of any of these lipid species compromises the barrier integrity of the SC.

The water in the SC is associated with the corneocyte proteins, which in principle would make the transcellular pathway the preferential route of penetration of hydrophilic molecules.[6] However, paracellular transport of hydrophilic molecules cannot be disregarded due to the presence of polar

channels between the oriented polar head groups of remaining phospholipids in the lipid lamella, which may allow the transport of hydrophilic substances.[7]

There are many factors – both internal and external – that affect skin health and consequently its barrier function.[8] The internal factors include: genetics, which determine the biological ageing and predisposition to skin diseases such as atopic dermatitis[9] and psoriasis,[10] hormones and specific conditions such as diabetes.[11] The external factors involve the exposure to ultraviolet (UV) radiation[12] or extreme temperatures, contact with certain substances[13] (*e.g.* ethanol), administration of particular medicines (*e.g.* diuretics) and medical procedures (*e.g.* radiotherapy and dialysis).

Some typical morphological differences between healthy and unhealthy skin are shown in Figure 2.4 and Figure 2.5.

Figure 2.4 shows LM images of hematoxylin and eosin stained sections of healthy human skin (Figure 2.4, Image A) and human skin treated with different amounts of an irritant (Figure 2.4, Images B, C and D).

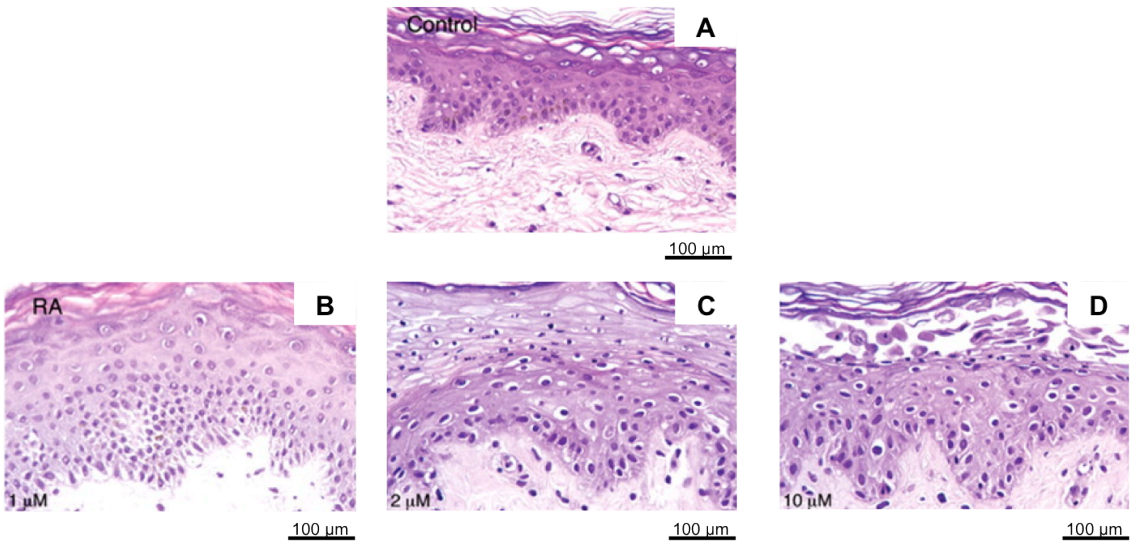

Figure 2.4 LM images of healthy human skin (A) and human skin after incubation for 8 days in organ culture in the presence of different amounts of an irritant (all-trans retinoic acid): 1 µM (B), 2 µM (C) and 10 µM (D). Image adapted from Varani *et al.*[14].

Epidermal hyperplasia can be observed in skin treated with 1 μM of irritant (Figure 2.4, Image B). With increasing concentrations of irritant, 2 μM and 10 μM, there are abnormalities in the upper epidermis including, incomplete keratinization, loss of the granular layer, loss of the intercellular connections and separation of the upper layers from the lower layers of epidermal cells (Figure 2.4, Images C and D).

Figure 2.5 shows TEM micrographs of healthy mouse skin (Figure 2.5, Image I and II) and mouse skin after the application of a pharmaceutical formulation used for treatment of non-melanoma skin cancer (Aldara) (Figure 2.5, Image III, IV and V). Starting at 12 h, Aldara application massively disturbed the epidermal integrity and led to keratinocyte apoptosis as demonstrated by the presence of pyknosis, nuclear fragmentation and residual bodies (Figure 2.5).

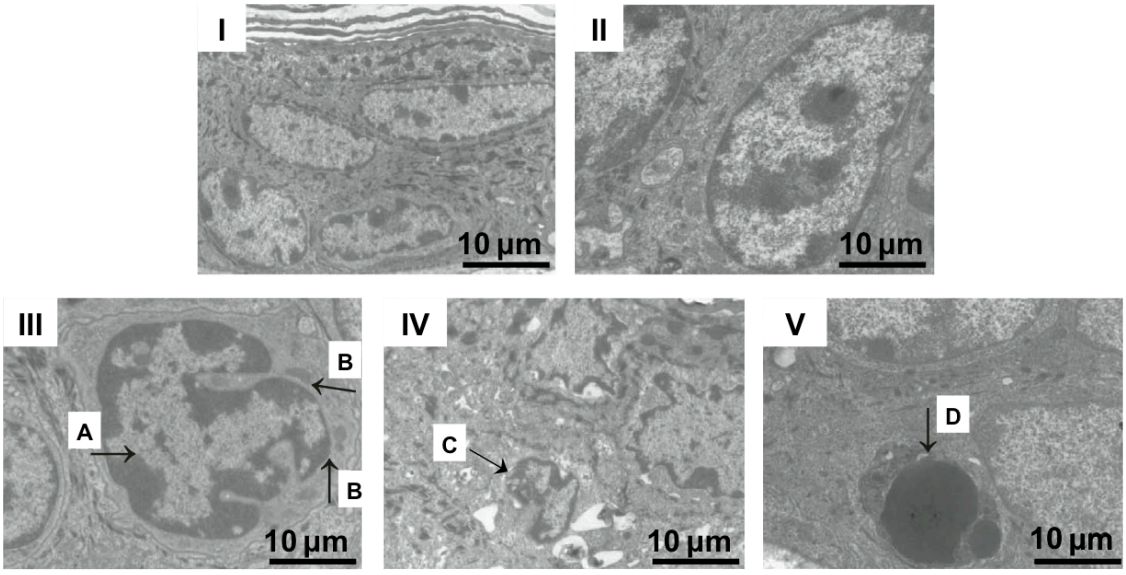

Figure 2.5 TEM of healthy mouse skin (I and II), 12 hours (III) and 24 hours (IV and V) after one topical application of a pharmaceutical formulation used for treatment of non-melanoma skin cancer (Aldara). The arrows indicate: (A) early-stage apoptotic pyknotic constricted nucleus, (B) intact mitochondria, (C) late-stage apoptotic pyknotic constricted nucleus and (D) residual body. Image adapted from Walter *et al.*[15].

2.1.2 Skin tight junctions: MDCK-II cells

Tight junctions form a belt at the apical side of the keratinocytes of the stratum granulosum (green line segments in Figure 2.2), providing an additional barrier beneath the SC that controls fluid loss and protects against pathogens.[16]

Each tight junction sealing strand is composed of a long row of transmembrane adhesion proteins embedded in each of the two interacting plasma membranes, the extracellular domains of these proteins adhere directly to one another to occlude the intercellular space. These transmembrane proteins include claudins, occludin, junctional adhesion molecules (JAMs), and tricellulin as well as numerous cytoplasmic zonula occludens (ZO) proteins, such as ZO-1, ZO-2, ZO-3, cingulin, 7H6 and symplekin.[17-20]

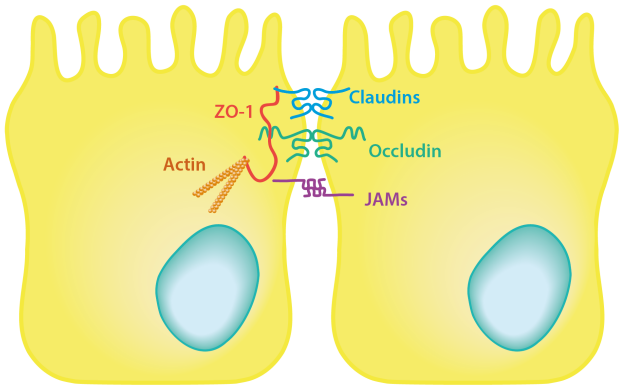

Figure 2.6 Schematic diagram of the molecular organization of epithelial tight junctions.

Figure 2.6 illustrates the organization of the tight junctions transmembrane proteins.

Claudins are the major transmembrane proteins forming tight junctions. They are essential for their formation and function. The claudin family consists of 24 distinct members in human and mice. Different members of the claudin family are expressed in different tissues, conferring different permeability properties

on the various epithelial sheets. Claudins are linked to the actin cytoskeleton through binding to the scaffolding proteins (ZO-1 and ZO- 2).

Occludings are the second major transmembrane proteins of the tight junctions. They interact with a variety of cellular signalling molecules and may contribute to the signal transduction at the junction. However, their function is still unclear. Occludin directly binds to ZO-1, and the phosphorylation of some tyrosine residues prevents both the interaction with ZO-1 and the assembly at tight junctions.

The third major tight junctions transmembrane proteins are tricellulins, which are required to seal cell membranes together and prevent leakage at the points where three cells meet.

Claudin and occludin span the plasma membrane four times; each protein contains two extracellular loops, one intracellular loop with the C- and N-termini being cytosolic. The extracellular loops of adjacent cells bind to each other and generate close membrane proximity. The carboxyl termini of both occludin and claudin are associated with the guanylate kinase homologues ZO-1, ZO-2 and ZO-3.

Tight junctions participate in the establishment and maintenance of apical-basal polarity of cells that is controlled by a network of protein and lipid regulators.[21]

TEER measurements are typically used to evaluate this apical-basal polarity. TEER is an indirect assessment of tight junction stability and consequently, a direct measure of the functionality of barrier function in epithelial tissue, reflecting the overall resistance and quality of the barrier.[22]

TEER measurements may be performed on vital cell cultures in a label-free manner. By exceeding certain TEER threshold, researchers can conclude that the cell layer is confluent and the formation of tight cell-cell junctions has occurred.[23]

Traditionally, chopstick-type electrodes of different lengths are used to measure the electric resistance of barrier-forming cell cultures on transwell inserts.[17] The shorter electrode should be suspended in the fluid of the apical

compartment, while the longer electrode should touch the bottom of the basolateral compartment (Figure 2.7).

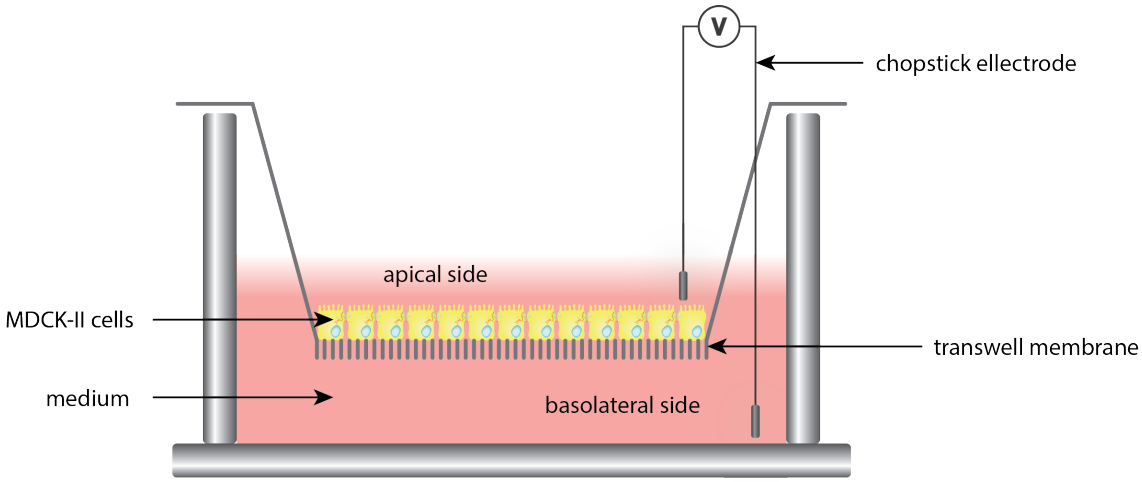

Figure 2.7 Schematic illustration of the MDCK-II cell culture and the position of the electrodes for TEER measurements.

An epithelial voltohmmeter passes 10 μA alternating current of 12.5 MHz frequency through two chopstick Ag/AgCl electrodes and records the resistance.[22] This current is non-destructive; therefore multiple readings can be performed on the same cell monolayer at different time points. TEER measurements are temperature-dependent, thus the readings should always be made at a constant temperature to avoid undesired fluctuations on the resistance readouts.

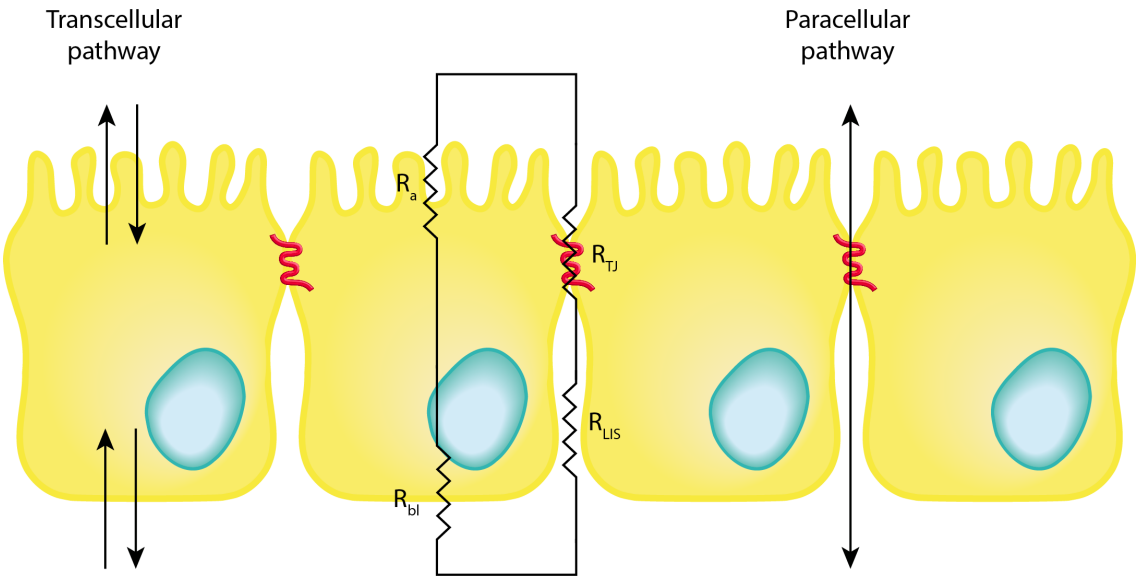

Figure 2.8 Electrical circuit models of the series and paracellular resistances across the trans- and para- cellular pathways of an epithelial cell monolayer. R_a is the apical resistance, R_{bl} the basolateral resistance, R_{LIS} the lateral intercellular space resistance and R_{TJ} the tight junction resistance.

The cell membranes are generally of very high apical resistance (R_a) and basolateral resistance (R_{bl}). The resistance of these series elements is typically much higher than that of the parallel elements of the paracellular pathway. Thus, the overall resistance of an epithelium is defined by the tight junction resistance (R_{TJ}), which is defined by the composition of claudins in the tight junction (Figure 2.6). Theoretically, the lateral intercellular space (R_{lis}) could contribute a resistance in series with the tight junction, but there is little evidence that this is physiologically significant.[24]

MDCK-II cells are widely used as models for studying epithelia as they have clear apico-basolateral polarity, well defined cell junctions, a rapid growth rate, are suitable for confocal imaging and will polarise in 2D and 3D cell culture. MDCK II cells with cell junctions display TEER values in the order of 100-150 $\Omega \cdot cm^2$.[25]

2.2 Penetration of molecules and nanoparticles through skin

Transdermal drug delivery involves the application of an active pharmaceutical ingredient into the skin with the purpose of reaching the systemic circulation. In general, once a molecule crosses the SC barrier, the diffusion into deeper skin layers and systemic uptake occurs relatively quickly and easily.[26]

When compared with intravenous or oral drug delivery routes, the transdermal route has several advantages such as, the avoidance of hepatic first pass metabolism, fewer side effects, the ability to promptly discontinue administration and the enhancement of therapeutic efficiency and the maintenance of constant systemic concentrations throughout the duration of use. Although the skin is one of the most extensive and readily accessible organs, delivery of drug molecules into and through the skin is challenging.

Generally, transdermal delivery of molecules into the skin is a passive process governed by Fick's law:

$$\mathrm{J} = -\mathrm{D}\frac{\partial \phi}{\partial \mathrm{x}} \tag{2.7}$$

where J is the diffusion flux, *i.e.* the amount of substance that diffuses per unit area per unit time, D the diffusion coefficient, ϕ the concentration of the substance and x the length of the diffusion pathway.[27] In other words, the rate of a substance transport across the skin depends not only on the physicochemical characteristics of the substance, *i.e.* aqueous solubility, oil/water partition coefficient, concentration in the galenic formulation, but also on the surface area of the skin to which it is exposed and the thickness of the SC.[28]

Dermal absorption of a substance is highly dependent on both, the physiologic characteristics of the skin[29] (*e.g.* species, gender, age, site of application, condition of the skin, skin thickness, hydration, and temperature) and the physicochemical properties of the compound (*e.g.* lipophilicity, polarity, volatility, volubility, concentration, galenic formulation) that comes into

contact with the skin.[30] Apart from these factors, technical aspects of the respective *in vitro* or *in vivo* test can also be reflected in the dermal absorption of a substance.[31]

Significant effort has been made to develop strategies to overcome the low permeability of intact human skin and increase the bioavailability of transdermal formulations. These strategies involve the use of chemical enhancers (*i.e.* alcohols, amides, glycols and surfactants), physical enhancers (*i.e.* iontophoresis, electroporation, phonophoresis, microneedles and jet-injectors) or certain galenic formulations (*i.e.* toluene, buffer organic solution).[32] Among these strategies is the use of NPs, which properties such as increased drug absorption, target delivery, controlled drug release and outstanding therapeutic index, makes them promising candidates to effectively deliver drugs across the skin.

There are two main pathways for the penetration of any substance through the skin: along the skin appendages: hair follicles and pilosebaceous pores or sweat gland pores – transappendageal route; or transport through the SC and the underlying layers - transepidermal route (Figure 2.9).[27]

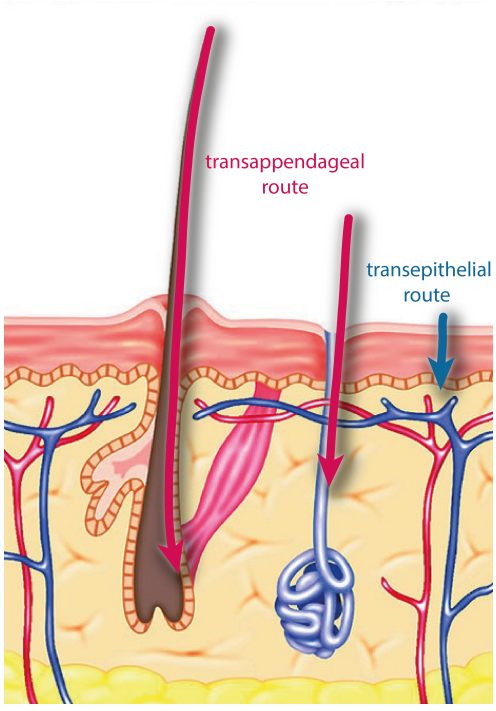

Figure 2.9 Routes of penetration through the skin: trasappendageal (red) and transepidermal (blue).

The transepidermal route can be divided into the transcellular and paracellular route (Figure 2.10).

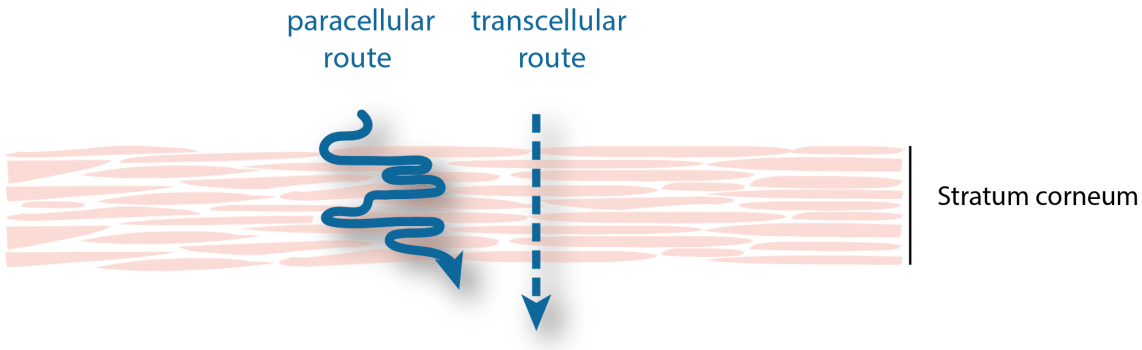

Figure 2.10 Transepithelial routes of skin penetration: paracellular and transcellular

Through the transcellular route, the materials cross the skin passing through both the lipid structures of the SC and the cytoplasm of the dead keratinocytes. This is the shortest penetration route, but the substances face significant resistance to penetration because they have to cross both lipophilic and hydrophilic structures. Through the paracellular route, the substances overcome the SC traveling between the corneocytes. This route appears to be the dominant route for the entry of substances unto the skin.

The exact mechanics of skin penetration by inorganic NPs is still unknown. However, a closer look into the skin architecture might provide a suggestion for such mechanism. Typically, lipids arrange themselves into a bilayer, with all their hydrophobic tails pointing inwards and their hydrophilic heads outwards. However, the lipid molecules in the SC are stretched-out, so that the two tails of each molecule point in opposite directions. The molecules are stacked on top of each other in an alternating fashion way, forming a structure which is much more impermeable than a normal bilayer. The lipophilic pores formed by tail-to-tail configuration of the lipids are estimated to be smaller or equal to 6.94 nm. Meanwhile, the aqueous pores, *i.e.* hydrophilic regions delimited by lipid heads, have been estimated to have a diameter of 2.8 ± 1.3 nm.[33] However, it has been suggested that the skin may contain different types of

aqueous pores, whose dimensions of superficial openings (0.4–36 nm) may not be maintained in the internal channel.[34] These aqueous pores provide a possible route for penetration of hydrophilic substances. However, it has been reported that the penetration of water and polar molecules through this route is poor,[35] which may further question if the penetration of inorganic NPs could nonetheless happen through this pores or not.

The analysis of SC structure and nanoporosity suggests that, in healthy skin NPs have to be smaller than 5–7 nm to have possibilities to diffuse throughout the fluid portion of the lipidic bilayers,[36] or smaller than 36 nm to potentially diffuse through the aqueous pores.[33-35]

For instance, Zhang *et al.*[37] studied the penetration of QD though porcine skin, showing that most PEG- coated QD were located in the intercellular lipids of the outermost layers of the SC. Thereby they concluded that those NPs penetrate the skin via the paracellular pathway, suggesting that because the outer PEG-coating is a soft coating, it allows the NPs to squeeze through the intercellular spaces. In contrast, Lee *et al.*[38] showed that on application of 4.6-10 nm diameter iron oxide NPs on skin after superficial skin incision of 1 μm width, the NPs were located in both the intercellular and intracellular spaces of the SC and viable epidermis near the area of incision. However in an area 30 μm deeper from the incision, the NPs were located only in the intracellular spaces of the viable epidermis. These results suggest that 4.6-10 nm diameter iron oxide NPs, when in contact damaged skin, can readily diffuse into the viable epidermis through the intracellular route.

The follicular pathway is also a possible pathway for skin penetration of inorganic NPs. However, the skin appendages occupy only a small fraction (0.1%) of the skin total surface area and their contribution for the penetration is not considered significant.[39] Even if substances may enter the skin through its appendages: hair follicles, pilosebaceous pores (10 - 70 μm) or sweat gland pores (60 - 80 μm), they still have to penetrate the respective tissue, crossing the epithelial skin barrier.[40] For instance, Lekki *et al.*[41] have studied the possible role of the follicular pathway on the percutaneous uptake of titanium dioxide NPs of 20 nm in width and 100 nm in length. Although these NPs were found as deep as approximately 400 nm inside the hair follicle, no particles were found in the surrounding viable tissue.

Independently of their penetration pathway, the potential of inorganic NPs to penetrate the skin make them ideal for therapeutic and drug delivery applications. On the other hand, they also may cause toxicological effects in the skin. One of the skin functions, apart from acting as a physical barrier, is to provide an active immune response, which involves immune-competent skin cells and soluble biologic response modifiers including cytokines. The dermis contains most of the lymphocytes in the skin, other migrant leukocytes, mast cells, and tissue macrophages, involved by a network of lymphatic and blood vessels. Although, before reaching the dermis, any transdermally delivered substance needs to cross the epidermis. The epidermis has no direct access to the blood or lymphatic circulation. Nevertheless, the epidermis is equipped with immune-competent cells such as, Langerhans cells, the macrophage-like antigen-presenting cells; keratinocytes, epithelial cells with immune properties; dendritic epidermal T lymphocytes, resident cells that may serve as a primitive T-cell immune surveillance system; epidermotropic lymphocytes, migrants from vessels in the dermis; and melanocytes, epidermal pigment cells with immune properties.[42]

Having said that, once the NPs have penetrated the top keratinous layer of the skin, possible phagocytosis by macrophages, Langerhans cells and keratinocytes may occur, triggering the skin immune system response.[43, 44] Although the distribution of NPs is more likely to remain localized, a possible distribution in the rest of the body might occur if the NPs reach deeper layers of the skin in sufficient concentrations.[45] A study by Kim *et al.*[46] found that near infrared quantum dots (15-20 nm) intradermal injected in mouse and porcine skin were located in lymph nodes. The suggested transport mechanism was via skin macrophages and Langerhans cells mediated by phagocytosis.[47] It should be noted that these quantum dots were intradermal injected into the skin and therefore they were not exposed to the skin natural barrier, the SC.

Apart from triggering the immune response, the penetration of inorganic through the skin may also produce an adverse impact in the epithermal stem cells in the niche. These epithelial stem cells are responsible for maintaining tissue homeostasis, regenerating hair, and repairing the epidermis after injury.[48] Despite of the importance of the epithelial stem cells for the maintenance of skin structure and functions; there is a serious lack of information concerning the biological activity of NPs in epithelial stem cells.

Sengstock *et al.*[49] evaluated cellular uptake of 80 nm silver NPs by mesenchymal stem cells, *i.e.* multipotent stromal cells that can differentiate into a variety of cell types including: osteoblasts (bone cells), chondrocytes (cartilage cells), and adipocytes (fat cells); and to assess their effect on stem cell viability and differentiation. They found that subtoxic concentrations of 80 nm silver NPs and silver ions reduced the adipogenic and osteogenic differentiation of human mesenchymal stem cell in a concentration-dependent manner, whereas chondrogenic differentiation was unaffected after 21 days of incubation. Silver NPs of 80 nm of diameter were taken up after 24 hours of incubation. These NPs were mainly found as aggregates in the endolysosomal cell compartment. In contrast, Samberg *et al.*[50] showed that exposure of human adipose-derived stem cells to 10 and 20 nm silver NPs either prior to differentiation, or following 14 days of differentiation, resulted in no significant or minimal cytotoxicity to undifferentiated stem cells. The cellular uptake of silver NPs into adipose-derived stem cells did not alter their ultrastructural morphology, or influence their differentiation.

Further studies are needed to investigate the effects of different inorganic NPs in directing stem cell behaviour, including assays for epidermal stem cells immunophenotype preservation or DNA stability, cytokine release, or the effects of multiple NPs exposures during differentiation.

Once the NPs overcome the SC, they may penetrate to deeper skin layers where they may reach the systemic circulation by entering the lymphatic or blood vessels, which are involved in the dermal or cutaneous clearance.[51] Dermal clearance is highly related to physiology of the blood vessels and physicochemical properties of the NPs. Parameters such as the thickness of blood vessel, area, distance between blood vessels and blood flow rate are likely to alter the dermal clearance.[52] Apart from dermal clearance, a substance may also be effectively removed through metabolism in the skin.[53]

Aside from the understanding of the exact mechanism of Inorganic NPs penetration through the skin, their toxicological effects and clearance, it is important to recognize whether NPs potentially penetrate the skin passively, due to the effect of their size, or under the influence of other factors. These will be further discussed in section 2.2.1.

2.2.1 Penetration of inorganic nanoparticles through the skin

Inorganic NPs exhibit unique physicochemical properties that have make them the central components in an array of emerging technologies, and they are now incorporated in many commercial products.[54]

Recent advances in nanotechnology result in potential body exposure to NPs. The most likely routes of entry into the body are the respiratory and gastrointestinal tracts and the skin.[55] Dermal toxicity, *i.e.* the adverse effects occurring as result of the exposure of skin to a substance, is therefore of particular relevance after occupational or environmental exposure to NPs. Skin is also exposed to NPs in cosmetics and is the preferred route of administration for topically applied drugs targeted either locally, for dermatological applications, or transdermally, for systemic therapy.[56, 57]

Among the inorganic NPs, gold NPs are particularly attractive for dermatological applications due to their unique physicochemical properties and their relatively easy modification in terms of size, topology and surface charge. Additionally, their high surface area provides sites for drug loading and enhances the solubility and stability of loaded drugs.[58, 59] Further, the ability to functionalise gold NPs with targeting ligands increases their therapeutic potency, decreases side effects, and offers the possibility of multivalent interactions with cell surface receptors or other biomolecules.[60]

Currently, the interaction of NPs with skin has been receiving significant attention, mainly because of the increasing use of nano-sized particles in consumer products, such as stain-resistant clothing, cosmetics, and sunscreens. Nonetheless, the question of whether or not NPs can penetrate the skin is not only important from an environmental and occupational health and safety viewpoint,[61] in which the NP exposure is not intentional and their penetration is undesired; but also from the therapeutic and diagnostic perspective, in which the NPs must be able to penetrate the skin barrier, deliver the drugs, and clear from the body without adverse side effects.

Despite the interest of researches, the ability of inorganic NPs to overcome the SC and reach deeper skin layers is controversial among the research community. An overview of the reported studies focused on the penetration of inorganic NP through skin is presented in Table 2.1.

Table 2.1 Overview on the studies focused in the skin penetration by inorganic NPs.

NP type	**Shape**	**Size**	**Coating**	**Skin type** (*in vitro*/ *in vivo*)	**Setup**	**Enhance approach**	**Time** (hours)	**Characterization assays**	**Outcome**	**Ref**
Zinc oxide	Spherical	26 nm 30 nm	polymethylsilsesquioxane (3 different formulations)	Human abdominal epidermis (*in vitro*)	Franz diffusion cells	-	24	•ICP-mass spectroscopy •TEM sectioning	No penetration.	Cross *et al.*[62]
Zinc oxide	Spherical	10-80 nm	dimethoxydiphenylsilane/ triethoxycaprylylsilane in formulation	Human skin (*in vitro*)	Not stated	Tape-stripping	48	•Proton induced X-ray spectroscopy scanning •Transmission ion microscopy cryosectioning	No penetration either in intact or damaged skin.	Szikszai *et al.*[63]
Titanium dioxide	Lanceolate shape	length: 45-150 nm width: 17-35 nm	Not stated (four formulations)	Shaved Porcine (*in vitro*)	Applied by allergy test plasters	-	8 24 48	•Proton-induced X-ray emission •Rutherford backscattering •Scanning transmission ion microscopy •Elastic recoil detection analysis •Secondary electron imaging •TEM cryosectioning	Penetration after 8 hours of application.	Menzel *et al.*[64]

NP type	Shape	Size	Coating	Skin type (*in vitro*/ *in vivo*)	Setup	Enhance approach	Time (hours)	Characterization assays	Outcome	Ref
Quantum dots CdSe/ZnS core/shell Quantum dots CdTe/ZnS core/shell	Spherical	20 nm 33 nm	dihydrolipoic acid in formulation (50% dihydrolipoic acid, 50 % glycerol)	Mouse (*in vivo*)	Mouse was fitted with a pet cone to prevent removal/ingestion of applied NPs.	UV radiation exposure	24	•Transepidermal water loss •TEM cryosectioning	Low penetration for both, but higher on UV exposure.	Mortensen *et al.*[65]
Quantum dots (composition not stated)	Spherical Ellipsoid	4.6 nm 6 x 12 nm (minor axis x major axis)	PEG in borate buffer pH 8.3 PEG-amine in borate buffer pH 8.3 Carboxylic acid in borate buffer pH 9.0	Porcine (*in vitro*)	Franz diffusion cells	-	8 24	•Fluorescence quantification •Confocal microscopy	Penetration of spherical quantum dots (all coatings) and ellipsoidal PEG and PEG-amine by 8 h. Ellipsoidal carboxylic acid-coated quantum dots penetrate only at 24 h.	Ryman-Rasmussen *et al.*[66]
Quantum dots CdSe/CdS Core/shell	Nail shaped	5.78 x 8.4 width x length (39 ± 1 hydrodynamic diameter)	poly (maleic anhydride-alt-1-octadecene) and amino poly (ethylene glycol) methyl ether in water	Porcine-dermatomed (*in vitro*)	Franz diffusion cells	-	24	•Fluorescence quantification •Confocal microscopy •ICP-AES •TEM sectioning	No penetration.	Zhang *et al.*[37]

NP type	**Shape**	**Size**	**Coating**	**Skin type** (*in vitro/ in vivo*)	**Setup**	**Enhance approach**	**Time** (hours)	**Characterization assays**	**Outcome**	**Ref**
Quantum dots CdSe/CdS Core/shell	Spherical	6 ± 2 nm	Carboxylic acid	Rat (*in vitro*)	Franz diffusion cells	Flexion Tape-stripping Abrasion	8 24	•Fluorescence microscopy •ICP-AES	No penetration in intact or tape stripped skin. Penetration into deeper into the dermal layers in abraded skin.	Zhang and Monteiro-Riviere[67]
Silver NPs	Spherical	25 ± 7.1 nm	Polyvinylpirrolidone in ethanol	Human abdominal skin (*in vitro*)	Franz diffusion cells	Abrasion	24	•electro thermal atomic absorption spectroscopy •TEM sectioning	Low penetration, but higher on abraded skin.	Larese *et al.*[68]
Silver NPs	Spherical	20 nm 50 nm 80 nm 25 nm 35 nm	Uncoated Carbon coated	Porcine (i*n vivo*)		-	336 (14 days)	•TEM sectioning •EDX	No penetration.	Samberg *et al.*[69]
Iron oxide NPs	Spherical	4.9 ± 1.3 nm	Sodium bis(2-ethylhexyl) sulfosuccinate	Human skin (*in vitro*)	Franz diffusion cells	-	3 6 12 24	•ICP-AES •TEM cryosectioning •EDX	Penetration through hair follicle and SC, occasionally reaching the viable epidermis.	Baroli *et al.*[70]

NP type	**Shape**	**Size**	**Coating**	**Skin type** (*in vitro/ in vivo*)	**Setup**	**Enhance approach**	**Time** (hours)	**Characterization assays**	**Outcome**	**Ref**
Gold NPs	Spherical	15 nm 102 nm 198 nm	Citrate	Rat skin (*in vitro*)	Franz diffusion cells	-	0.5 1 2 3 4 6 12 24	•ICP •TEM sectioning •EDX	Penetration was size-dependent: 15 nm gold NPs the highest and 198 nm gold NPs lowest penetration.	Sanovane *et al.*[71]
Gold NPs	Spherical	10 nm	-	Epidermal membrane from human skin (*in vitro*)	Franz diffusion cells	ppulsed electromagnetic field	4 8	•multiphoton microscopy •fluorescent lifetime imaging microscopy	No penetration through intact human skin, however the SC penetration was enhanced by the pulsed electromagnetic filed.	Krishnan *et al.*[72]
Gold NPs	Spherical	12.6±0.9 nm	Citrate	Human (in vitro)	Franz diffusion cells	Abrasion	24	•TEM •ICP-mass spectroscopy	Penetration of NPs through both damaged and intact skin, but significantly higher through damaged skin.	Filon *et al.*[73]

NP type	Shape	Size	Coating	Skin type (*in vitro*/ *in vivo*)	Setup	Enhance approach	Time (hours)	Characterization assays	Outcome	Ref
Gold NPs	Spherical	4.6±1.5 nm	11-mercapto-1-undecanesulphonate	Porcine skin (full- and split-thickness) (*in vitro*)	Franz diffusion cells	Ultrasound Sodium lauryl sulphate	24	•ICP-mass spectroscopy	Penetration was higher through pig split-thickness skin than through pig full-thickness skin. Ultrasound and sodium lauryl sulphate enhanced penetration.	Seto *et al.*[74]
Gold NPs	Spherical	6.0 ± 0.8 nm 14.9 ± 1.8 nm	6 nm coated with Dodecanethiol in toluene 6 nm coated with Lecithin in water 15 nm coated with Citrate in water 15 nm coated with Cetrimide In toluene	Human epidermal sheet	Franz diffusion cells	Tape-stripping	0.5 2 6 24	•Multiphoton microscopy	Penetration of 6 nm NP was higher than of 15 nm NPs. Surface hydrophobicity favours penetration.	Labouta *et al.*[75]

NP type	Shape	Size	Coating	Skin type (*in vitro/ in vivo*)	Setup	Enhance approach	Time (hours)	Characterization assays	Outcome	Ref
Gold NPs	Spherical	6.0 ± 0.8 nm 14.9 ± 1.8 nm	6 nm coated with dodecanethiol in toluene 15 nm coated with citrate in water	Abdominal human skin	Franz diffusion cells	-	4 24	•Reflectance confocal microscopy multiphoton tomography with fluorescence lifetime imaging microscopy •TEM cryosectioning	Penetration of 6 nm NPs in toluene after 24 hours. 15 nm NPs in water aggregate in the skin surface.	Labouta *et al.*[76]
Gold NPs	Spherical	14.9±1.8 nm	Citrate in water Cetrimide in toluene	Abdominal human skin	Franz diffusion cells	chemical enhancers: urea sodium lauryl sulphate polysorbate 80 dimethyl sulfoxide	24	•Multiphoton laser microscopy	Penetration of citrate coated NPs using dimethyl sulfoxide as chemical enhancer. Cetrimide-coated NPs aggregate in the SC after pre-treatment of the skin with dimethyl sulfoxide.	Labouta *et al.*[77]
Gold NPs	Not stated	Not stated	Not stated	Human SC (*in vitro*)	transdermal delivery chip system	Electrophoresis	1	•TEM sectioning	Penetration of NPs through skin increased with the electric field intensities.	Chen *et al.* [78]

NP type	**Shape**	**Size**	**Coating**	**Skin type** (*in vitro/ in vivo*)	**Setup**	**Enhance approach**	**Time** (hours)	**Characterization assays**	**Outcome**	**Ref**
Gold NPs	Spherical	5 nm (11.6 nm hydrodynamic diameter)	Polyvinylpyrrolidone Mixture of gold NP with proteins	Mouse skin (*in vivo*)	Applied in the dorsal clipped skin.	-	3	•TEM cryosectioning •Elisa •MTT	Penetration of gold NPs and proteins to deeper skin layers.	Huang *et al.*[79]
Gold NPs	Spherical	13 nm	siRNA	Human skin equivalents and mouse skin (*in vitro*)	Franz diffusion cells	-	24	•ICP-mass spectroscopy	Penetration through mouse skin and human epidermis within 3 hours.	Zheng *et al.*[80]

The inconsistent outcome of these studies is clear, with some studies showing NPs permeation,[64-68, 70-80] while in others NPs penetration was not observed.[37, 62, 63, 67, 69]

The reported studies are highly diversified in terms of skin type and condition (*e.g.* intact skin, or skin chemically or mechanically treated to enhance penetration), skin application area, exposure time, skin integrity maintenance during the experiment, galenic formulation (e.g. solvent, emulsion) and NP concentration and type (e.g. material, size, shape and functionalisation). This wide diversity of the experimental parameters, together with limitations in characterization techniques available to detect isolated NPs in such complex tissues as skin, may be the cause of the contradictory results.

Typically, the parameters that influence the skin penetration by inorganic NPs can be subdivided in 3 subsections: structural and physical characteristics of the skin, physicochemical attributes of the NPs and experimental features. These subsections are further developed in the following paragraphs.

Structural and physical characteristics of the skin

Skin type

Although excised human skin is preferred for *in vitro* skin penetration studies especially for human dermal risk assessment,[81] human skin has limited availability. Consequently, many research studies focused in skin penetration of inorganic NPs are conducted on animal skin (*e.g.* pig, mouse, and rat skin), either *in vitro* or *in vivo*. However, structural and morphological differences between human and animal skin, in terms of the density of the hair follicles, thickness of SC, the amount of skin lipids, in addition to variations among animal species, could certainly result in different penetration outcomes.[81, 82]

Skin treatment

Different skin treatments have been adopted in NP penetration experiments. These treatments include non-intentional approaches, such as hair removal before topical application of NPs and the used of different formulation ingredients, or intentional approaches of either physical or chemical nature, used to enhance skin penetration by NPs.

For instance, when the animal species used for conducting particle penetration experiments is a hairy animal, the hair is usually removed before application of the formulation. Hair removal can be done by clipping, applying cosmetic-grade hair removal cream, or by shaving before the penetration experiment. Huang *et al.*[79] investigated the co-administration of protein drugs with 11.6 nm polyvinylpyrrolidone-coated gold NPs in clipped mice skin. Results showed that these gold NPs are skin permeable, ability presumably attributed to the nano-bio interaction with skin lipids and the consequent induction of transient and reversible openings on the SC. Furthermore, when a mixture of gold NPs and protein drugs was applied, both were able to penetrate the skin barrier and migrate into the deeper skin layers, avoiding the complicated process of gold NP drug-functionalization. On the other hand, Labouta *et al.*[77] reported no penetration of gold NPs, having nearly the same size, 15 nm, through abdominal human skin *in vitro*. Therefore, hair removal should be taken into consideration especially when assessing the safety of NPs.

As mentioned previously, intentional skin approaches of either physical or chemical nature have been adopted for enhancing skin penetration by NPs.

Physical or mechanical enhancement includes techniques such as UV exposure, iontophoresis, dermaportation, sonophoresis, tape stripping, dermabrasion, skin flexion and massage.

UV radiation can have a harmful effect on the skin barrier function.[83] Titanium dioxide and zinc oxide NPs are often used in sunscreen formulations that are applied when skin is exposed to UV radiation. Thus, studying particle penetration into the skin when the latter is exposed to UV radiation is of the utmost importance. For instance Mortensen *et al.*[65] reported higher penetration quantum dots through mouse skin when skin was exposed to UV radiation

than through intact mouse skin. Penetration happened mostly in defected areas in the SC or around hair follicles.

Iontophoresis offers an enhancement penetration mechanism of hydrophilic and charged molecules across the skin by application of a constant low intensity electric current.[84] Using this approach, Chen *et al.*[78] investigated a transdermal delivery chip system for delivering gold NPs into human SC. This study hypothesized that a transdermal delivery chip system could provide electrostatic force to drive gold NPs through the human SC via paracellular route. Basically, various direct current voltages (3, 6, and 9 V) were applied to generate electric fields of different intensities (3.2~9.8 V/cm) in order to drive gold NPs into the human SC. Results showed that at zero voltage, gold NPs were localized on the surface of the SC. On application of 6 V, gold NPs were shown to pass through the paracellular route of the SC. Although the size, shape or functionalisation (charge) of the gold NPs was not stated, their results showed permeability of the skin increases with the electric field intensities.

Dermaportation is a novel transdermal drug delivery technology that uses pulsed electromagnetic fields to enhance the transport across the skin. Krishnan *et al.*[72] induced the skin penetration of gold NPs through human skin by dermaportation using a pulsed electromagnetic field. Results showed that 10 nm gold NPs do not penetrate intact human skin, however the SC penetration was enhanced by the pulsed electromagnetic filed.

Sonophoresis, defined as the application of ultrasound, particularly at low frequency (20–100 kHz), has been shown to greatly enhance the skin permeability of a variety of drugs.[85] Seto *et al.*[74] investigated the simultaneous application of ultrasound and sodium lauryl sulphate to full- and split-thickness pig skin as a synergistic mechanical and chemical approach to enhance the penetration of gold NPs. Results showed that after the ultrasound and sodium lauryl sulphate treatment the delivery of 4.6 nm gold NPs was greater through pig split-thickness skin than through pig full-thickness skin, due to the thicker dermis in the full-thickness skin that acts as a transdermal diffusion barrier to macromolecules.

Because the skin barrier function resides primarily in the SC, its total or partial removal by tape stripping or dermabrasion can disrupt the skin barrier, enhancing the transport of NPs across the skin. Tape stripping has been

commonly used to enhance drug delivery across the skin, and to obtain information about the SC function. Many studies have reported the use of the tape-stripping method for the removal of the SC in the study of NP penetration through skin. For instance, Labouta *et al.*[75] studied the penetration of four different types of gold NPs through human skin, which had been previously tape-stripped for complete removal of the SC, using multiphoton microscopy. NPs used in this study, namely: 15 nm gold NPs in water, 6 nm gold NPs coated with dodecanethiol in toluene, 6 nm gold NPs coated with lecithin in water and 15 nm gold NPs coated with cetrimide in toluene; differ in their surface polarity and the nature of the NPs dispersion medium. Results showed that skin exposure time had a critical impact on the penetration, and that an incubation time of at least 6 hours was required to observe a significant penetration extent. On the other hand, Szikszai *et al.*[63] who investigated the penetration of zinc oxide NPs into the skin after removal of the SC by tape stripping, reported that zinc oxide NPs remained on the surface of skin and did not penetrate into deeper dermal layers.

Dermabrasion is another technique that involves the removal or disruption of the upper skin layers to facilitate the skin permeation of several drugs.[86-88] Based on this, Filon *et al.*[73] induced the skin penetration of gold NPs through human skin by dermaportation using dermabrasion. Filon's group reported the penetration of 12.9 nm gold NPs through human skin. Their TEM investigation showed the presence of gold NPs either in the dermis and epidermis. ICP-mass spectroscopy results showed that a significantly higher gold amount was found in damaged skin compared to the intact skin. Larese *et al.*[68] showed that the penetration of polyvinylpyrrolidone-stabilised 25 nm silver NPs through intact and abraded human abdominal skin, despite of being low, was higher in abraded skin than in intact skin.

The impact of mechanical stress on the barrier function of the skin has also affects the NPs penetration through the skin. For instance, Zhang and Monteiro-Riviere[67] studied the effect of mechanical flexion on skin penetration of 6 nm quantum dots through rat skin. They showed that spherical and ellipsoid quantum dots penetration increased when additional enhancement approaches – dermabrasion, tape-stripping and flexion – were applied. Abraded and flexed skin samples were more permeable to quantum dots than the tape-stripped and intact specimens.

Most of the intentional approaches typically used to enhance skin penetration by NPs are physical methods. Nevertheless, the use of chemical enhancers has also been explored. Chemical permeation enhancers are defined as agents that promote drug diffusion through the SC and the epidermis. These agents have been extensively studied and used as enhancers in favouring transdermal drug permeation. They work mainly by temporarily reducing the barrier function of the SC allowing for more drug transport. However, their efficacy with regard to the delivery of high-molecular-weight drugs remains somehow limited.[89] Few studies have focused on the use of these enhancers for skin delivery of inorganic NPs. Labouta *et al.*[77] published a study on penetration of 15 nm gold NPs in the presence of several chemical enhancers – urea, sodium lauryl sulphate, polysorbate 80 and dimethyl sulfoxide – through human skin. Their results showed that among the tested chemical enhancers, dimethyl sulfoxide could induce the penetration of hydrophilic (citrate-stabilised) gold NPs of no intrinsic penetration ability in a concentration-dependent manner. Pre-treatment of the skin with dimethyl sulfoxide, resulted in aggregation of (cetrimide-coated) gold NPs in the top layers of the SC limiting penetration into the deeper skin layers. The NPs-galenic formulation interaction and the stability of the NPs in the applied formulation were shown to be a critical parameter in transdermal delivery of NPs.

Physicochemical attributes of the NPs

The physicochemical attributes of NPs such as, shape, size, charge and galenic formulation are key factors governing their skin penetration.

To study these effects of size and charge of quantum dots on skin penetration, Ryman-Rasmussen *et al.*[66] exposed the skin to two core/shell quantum dots, spherical of 4.6 nm diameter and ellipsoidal, of 12 nm major axis and 6 nm minor axis with three types of surface coatings: neutral, anionic and cationic. Their results demonstrated that spherical quantum dots with neutral and anionic coatings penetrated only up to epidermal layers, while cationic charged spherical quantum dots were localized in dermis within 8 h. In contrast, neutral and cationic charged ellipsoidal quantum dots penetrated into the skin

within 8 hours but anionic charged ellipsoidal quantum dots needed 24 hours to show penetration.

Regarding the NPs coating, Zhang *et al.*[37] showed that nail-shaped, PEG-coated quantum dots with diameter less than 40 nm could penetrate into uppermost layers of SC lipids and outer root sheath of hair follicles. Recently Zheng *et al.*[80] at Northwestern University investigated the skin penetration by 13 nm siRNA-based spherical nucleic acid gold NP conjugates, which were originally developed by Chad Mirkin for gene regulation in cells.[90, 91] Data showed that siRNA-functionalised NPs freely penetrate almost 100% of keratinocytes *in vitro*, mouse skin, and human epidermis within 3 hours after application.

Aside from the shape and surface functionalisation of the NPs, the nature of the galenic formulation may affect the barrier state of the skin and thus the NP penetration thought skin. Labouta *et al.*[76] studied the penetration and metabolic effects of ion-stabilised, polar, 15 nm gold NPs in aqueous solution and sterically stabilised, non-polar, 6 nm gold NPs in toluene on excised human skin. Data showed that 15-nm gold NPs in aqueous solution tended to aggregate on the superficial SC after 24 hours exposure, while 6-nm gold NPs in toluene penetrated through SC and into epidermal layers of human skin. Toluene was shown to have an effect on the barrier function of the SC by means of lipid extraction. However, there were no drastic changes in the intercellular lipid composition of the skin after toluene application under the reported experimental conditions. In fact, ceramides, known as the most important component of the SC multilamellar lipid structure with definite physicochemical properties necessary for the barrier function of the skin,[92] were not extracted by toluene. Additionally, Menzel *et al.*[64] investigated the penetration of four different formulations containing titanium dioxide NPs with lanceolate shape (17-35 width; 45-150 length) into porcine skin. They showed that micronised titanium dioxide particles from all formulations tested penetrated through intercellular spaces in the SC into the living stratum granulosum within the first 8 hours after application.

Experimental parameters

Apart from the skin penetration enhancement treatments and the NPs physicochemical properties, parameters related with the experimental procedure, such as skin exposure time, experimental setup and diffusion area play a key role in the NPs penetration through skin.

Skin exposure time to NPs significantly varies among studies. Penetration of particles was tracked over a period of as short as a few hours up to several days (Table 2.1). However, unlike in the studies of penetration of drug molecules through the skin, it is not possible to generate appropriate pharmacokinetic parameters for NPs, including the flux for normalizing the effect of exposure time, due to absence or a scarce concentration of NPs penetrating into the skin. Nevertheless, Baroli *et al.*[70] evaluated whether sodium bis(2-ethylhexyl) sulfosuccinate coated iron oxide NPs of 4.9 nm diameter could penetrate and eventually permeate excised human skin after 3, 6, 12 and 24 hours. NP penetration was reported starting from 6 hours of skin exposure time. The results of this study showed that NPs were able to penetrate through hair follicle and SC, occasionally reaching the viable epidermis. However, NPs were unable to permeate the skin.

The experimental setup is equally important when evaluating the skin penetration of a NP or any other substance. Franz diffusion cells are the most used experimental setup in skin penetration studies. Briefly, the Franz diffusion cells are composed of a donor compartment and a receptor compartment between which the skin is positioned (Figure 2.11). The donor compartment, above the skin, contains the topically applied compound. The receptor compartment, below the skin, contains the receptor fluid. Samples of this fluid are collected through the sampling port. The receptor compartment is surrounded by a water jacket maintained at a constant temperature.

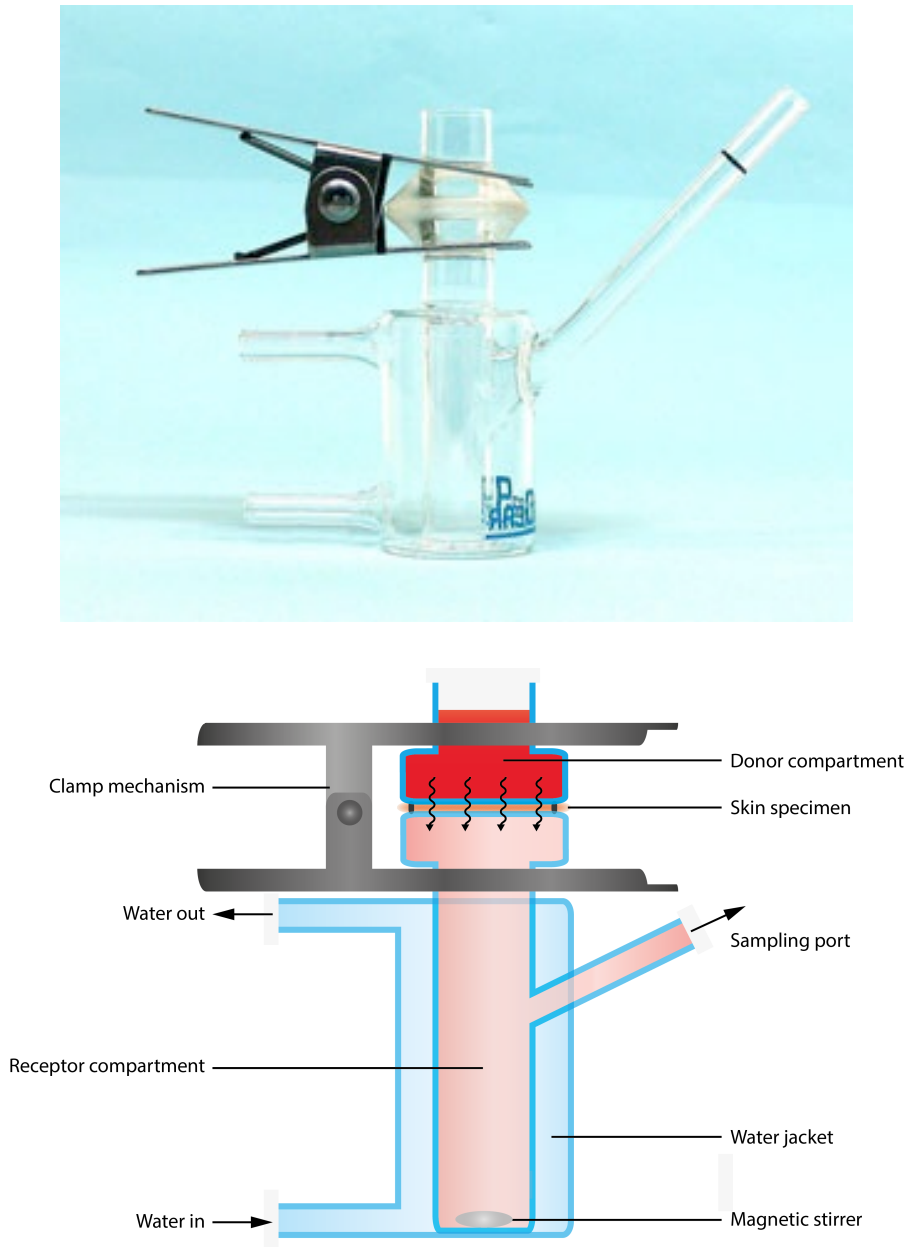

Figure 2.11 Photography (top) (retrieved from: http://www.permegear.com/) and schematic illustration (bottom) of excised skin mounted in a Franz diffusion cell system.

Sonavane *et al.*[71] used Franz diffusion cells to study the penetration of 15 nm, 102 nm and 198 nm citrate-coated gold NPs through rat. In the study carried on by Sonavane and co-workers, TEM, EDX and ICP-AES analysis of the skin samples exposed to NPs showed that the penetration of gold NPs through rat skin is size-dependent, with greater penetration of 15nm gold NPs compared to 102 nm and 198 nm gold NPs. Labouta *et al.*[75] reported a similar size-

dependent penetration phenomenon for smaller gold NPs through human skin, where 6-nm particles could penetrate to a greater extent than 15-nm gold NPs.

Although the Franz diffusion cell is the most common setup for conducting penetration experiments, in a recent study Labouta and co-workers reported that the Franz diffusion cell was not a suitable setup for penetration studies carried on in reconstructed skin.[93] They showed that the Frank diffusion system applies excessive pressure on the tissue that leads to the detachment of the SC and loss of the skin barrier function. To avoid this, their experiments were run in six-well plates with transwell inserts in which the basolateral side was equivalent to the receptor compartment in the Franz diffusion cell, and NP dispersion was applied on the top of the specimen. Although the non-suitability of the Franz diffusion cells was only showed to reconstructed skin, in our studies we decided not to use this type of setup. Therefore, an altered version of the setup proposed by Labouta et al.[93], adapted to full-thickness mouse skin (Figure 3.3), was used in our experiments. The experiments with full-thickness human skin (Figure 3.2), due to its higher thickness compared to skin equivalents and mouse skin, were preformed in an simplified version of the setup described by Labouta *el al.*[93].

The application dose and volume, and the diffusion area are also important factors that would significantly affect the results of any penetration experiment. For instance Labouta *et al.*[75, 76] reported the inability of citrate-stabilized gold NPs to cross the whole depth of the SC of human skin into deeper skin alyers. This was contrary to the findings of Sonavane *et al.*[71] who showed permeation of gold NPs, prepared by the same method and of almost the same size, through the full skin thickness after only 1 hour of skin exposure. However, they used a volume of donor solution per square centimetre of skin surface (4 ml donor volume and 6.3 cm^2 diffusion area) that was 2.2 times greater than that the one used in Labouta study (0.5 ml and 1.76 cm^2).[75] This is in addition to using rat skin of different permeation and structural characteristics than human skin. Labouta *et al.*[76] also showed that the concentration of the nanodispersion applied and skin exposure time could greatly influence the skin penetration of NPs. They applied dodecathiol-coated 6 nm gold NPs on human skin with two different concentrations of gold (90 and 437 μg/mL), for exposure times of 0.5, 2, 6, and 24 hours. Both the amount of gold NPs penetrating into the deeper skin layers and the

penetration depth increased with higher concentration and longer skin exposure time.

All this makes it difficult to compare the published results by different research groups. Many on studies have contradictory results and a missing or not clear knowledge on the potential mechanism of inorganic NPs penetration through skin. The skin penetration determinants mentioned play key roles on the evaluation of NP penetration through the skin and must be considered in order to obtain reliable results. Therefore, further investigation on the penetration of inorganic NPs through skin, using an experimental system with unvaried skin penetration determinants is required for a better understanding of NPs skin penetration and a deeper insight into the NPs mechanism of penetration. These investigations should be focused on determining the conditions under which NPs may penetrate the SC barrier and how the NP physiochemical properties may influence their penetration and toxicity.[40, 94-99]

2.2.2 Interaction of gold nanoparticles with tight junctions

The potential of gold NPs to be used in biological applications has led to a strong interest in studying their behaviour in biological systems. Ultimately, most of biological applications of gold NPs require their introduction into a living system. The bloodstream of an organism, the cytoplasm of the cell, and even the media in which cells grow are all complex aqueous mixtures different components, such as electrolytes, serum proteins, essential amino acids and nutrients. These various components could interact with NPs and change their physiochemical properties such as size and aggregation state, surface charge, and surface chemistry.[100] In a biological medium, NPs may interact with biomolecules such as proteins, nucleic acids, lipids and even biological metabolites. These interactions may result in the colloidal NP aggregation.[101-104] Aggregation occurs when the van der Waals attractive forces between NPs are greater than the electrostatic repulsive forces that stabilise them.[105] Basically, high concentration of ions in biological media may decrease the screening length of charged chemical groups on the NP surface and eventually serum proteins will replace the molecules in the NP surface.[106] In fact, it has been reported that plasma proteins can be adsorbed into NP surface spontaneously

and that the surface chemistry of the NPs in growth media is not the same as the originally synthesized materials.[107, 108] Several studies have attempted to coat NPs with a stabilizing shell consisting of PEG, proteins or DNA in order to avoid the NPs aggregation in growth media. Although these stabilized NPs do not aggregate in the short term, several experiments have demonstrated eventual aggregation both *in vitro*[103] and *in vivo*.[109] The presence of these unwanted aggregates may affect the experimental reproducibility in biological applications and impede the targeting efficiency of NPs to cells and tissues. Furthermore, the aggregation of NPs can affect their uptake and toxicity to cells or biological tissues.

Much work is currently focused on the development of nanocarriers as noninvasive devices for transdermal delivery of drugs.[110] To be effective, the NPs must first cross the skin epithelial cell barrier and enter the bloodstream or even translocate to other organs of the body. The epithelial cell barrier serves as the frontline to protect the body from foreign substances, making delivery of molecules inefficient and difficult. There is little information on the translocation of NPs across the skin epithelial barrier and the effect of NPs on these cell barriers.

As mentioned before tight junctions form a belt at the apical side of the keratinocytes of the stratum granulosum, providing an additional barrier beneath the SC that controls fluid loss and protects against pathogens.[16] Thus epithelial cell monolayers with formed tight junctions are commonly used as *in vitro* models to predict the permeability of drugs or substances.[111]

A few *in vitro* studies have investigated the interaction of gold NPs with epithelial cell monolayers. Liang *et al.*[112] investigated the effect of size and surface properties of gold NP on their uptake into Caco-2 cells. In this study, densely packed polymer-coated gold NPs of 5 nm, 10 nm and 20 nm diameter were introduced to epithelial Caco-2 monolayers. Poly(acrylic acid) was used to provide the particles a negative charge, poly(2-aminoethyl- acrylamide a positive charge and poly(2,3-hydroxy- propylacrylamide) a neutral charge. PEG and a temperature responsive polymer poly(N-isopropylacrylamide) were also used to cover the NPs. Results showed that the negatively charged gold NPs were taken up by cells in higher number than the neutral charged NPs, however the positively charged gold NPs gave the greatest uptake efficiency. It

was also reported that the surface charge was significantly more important than size on the cellular uptake, so the cationic and hydrophobic surfaces showed greatest uptake over neutral or negatively charged gold NPs. Following this study, the same group investigated the efficiency of the same type NPs to cross the Caco-2 epithelial barrier and evaluated whether these particles disrupt or not the tight junction barrier.[113] Results showed that positively charged and hydrophobic polymer-coated gold NPs have little or no translocation across the model Caco-2 monolayer, remaining either bound to the surface or being internalized within the cell. On the other hand, the neutral and negatively charged polymer-coated gold NPs with a size of 5 nm showed a significantly higher translocation. The decrease in the TEER values of the monolayers supported the changes observed in the tight junctions. These tight junctions fully recovered for most polymer-coated gold NPs 12 hours after removal of most polymer-coated gold NPs.

In a recent study by Chai *et al.*[114] the mechanisms adopted by monostearin solid lipid NPs, of approximately 100 nm in diameter, to cross the intestinal epithelial monolayer formed by MDCK-II cells were investigated. Monostearin solid lipid NPs were prepared by a novel solvent diffusion method in an acidic aqueous system. Fluorescein isothiocyanate-labelled octadecylamine was incorporated in the NPs and used as a fluorescence marker to investigate their interactions with MDCK-II cells monolayer. Results indicated that the solid lipid NPs transportation through the monolayer caused no effects on tight junctions, and that the transport of solid lipid NPs was rarely mediated via micropinocytosis. Furthermore, their results demonstrated that only approximately 2.5 % of the total NP was transported across the MDCK-II cells monolayer, and that the exocytosis of the lipid NPs from the apical side was more facile than that from the basolateral side. The lysosomes were the main destinations for the NPs. It was suggested that the endoplasmic reticulum, the Golgi complex and microtubules might play an important role in the transport of solid lipid NPs.

2.3 Gold Nanoparticles

Nanomaterials, of organic or inorganic nature, are characterized by unusual physicochemical properties that rise from their high surface-to-volume ratio. Nevertheless, inorganic nanomaterials possess some advantages over the organic nanomaterials: they are not subject to microbial attack, can be easily prepared, often have a low toxicity, and exhibit good storage stability.[115, 116]

Among inorganic NPs, gold NPs have attracted enormous attention because of their potential use in a wide range of biomedical applications, from labelling and delivery to hyperthermia and sensing.[117-119] Gold NPs are relatively easy to prepare in a wide range of sizes and shapes. Additionally, the surface of the gold NPs surface can be easily modified with molecules, including surfactants, polymers, and biomolecules, either by adsorption or chemical biding.[120] In many cases, the protecting shells not only stabilize the gold NPs, but can also be used for further functionalization.[121] Gold NPs high surface area, assures a large number of interaction sites available and the rate of interactions at the surface may, therefore, be higher. This has important implications for biomedical applications, such as drug delivery.[122, 123]

2.3.1 Synthesis of gold nanoparticles

Wet chemistry methods were employed in the synthesis of gold nanospheres (NSs) and gold nanorods (NRs). Basic principles and reaction mechanisms of their synthesis are described in the following subsections.

2.3.1.1 Synthesis of gold nanospheres

The unique optical properties of gold NPs have been exploited for scientists and artists for many centuries. The first applications of gold NPs date to the 4th century, where they were used to give vibrant colours, produced by their interaction with visible light, to ceramic porcelain and glass.[124] A piece of ancient art known as Lycurgus Cup is an example of the early application of the gold NPs plasmonic properties.[125] This cup consist of gold and silver NPs embedded into the glass, which makes it appear greenish when illuminated

from outside (light scattered by NPs defines the colour); or reddish when illuminated from inside (light transmitted by NPs defines the colour).

The first scientific literature on gold NPs formation was reported in 1857 by Michael Faraday who described the formation of a deep-red solution of colloidal gold by reduction of an aqueous chloroaurate solution using phosphorus in carbon disulfide.[126] However, great interests in preparing gold colloids was initiated when Turkevich in 1951 revisited Faraday's work and developed a protocol for the aqueous preparation of citrate-capped gold NPs.[127] Based on Turkevich protocol,[127] Frens in 1973 achieved the size-controlled preparation of monodisperse gold NPs within a range of diameters (16 – 147 nm) by controlling the reductant-to-stabiliser ratio.[128] The basic experimental route to make gold NPs following the Turkevich method is based on the reduction of tetrachloroauric acid using trisodium citrate at 100°C.

The formation of the gold NSs by the citrate reduction method can be summarized in three steps:[129] reduction of Au^{3+} in solution, disproportionation of Au^{+} to gold atoms and their nucleation, growth by disproportionation on particle surface, and coagulation. Oxidation of citrate results in the formation of dicarboxy acetone, which aids nucleation but also decomposes into side products.

The initial step of the synthesis is the oxidation of citrate, which yields decarboxy acetone:

$$C_6H_5O_7^- \rightarrow C_5H_4O_5 + CO_2 + H^+ + 2e^- \quad (2.1)$$

Then the auric salt is reduced to aurous salt:

$$AuCl_3 + 2e^- \rightarrow AuCl + 2Cl^- \quad (2.2)$$

In the second step, the aurous species are disproportionated to gold atoms:

$$3AuCl \rightarrow 2Au^0 + AuCl_3 \quad (2.3)$$

Finally, in the third step the gold atoms adsorb Au^+ complexes and form large aggregates. The absorption of Au^+ by the gold atoms leads to the formation of aggregates, by complexation with dicarboxy acetone.

The overall reduction reaction can be written as:

$$2AuCl_3 + 3C_6H_5O_7^- \rightarrow 2Au^0 + 3C_5H_4O_5 + 6Cl^- + H^+ + 3CO_2 \quad (2.4)$$

Citrate binds electrostatically to the gold surface, which allows the easy functionalisation by other ligands with stronger binding affinity with gold *via* ligand exchange reaction.

Typically, gold NSs display a sharp single UV-Visible absorption peak in the visible spectroscopy range, between 520 nm and 540 nm. This peak is size dependent and shifts to a longer wavelength with increasing the size of NSs.[130]

2.3.1.2 Synthesis of gold nanorods

The physicochemical properties of gold NPs are determined by their size and morphology. The anisotropic gold NPs that have drawn the most attention from the research community are gold NRs. As a result of the rod-shape structure, gold NRs exhibit unique optical properties, such as radiative elastic Raman scattering, inelastic Raman scattering and PL properties.[131] These features make them very interesting candidates for applications in the biological and biomedical sciences.[59]

Gold NRs show different colours depending on their aspect ratio, which is due to the two intense surface plasmon resonance peaks, *i.e.* longitudinal surface plasmon peak and transverse surface plasmon peak corresponding to the oscillation of the free electrons along and perpendicular to the long axis of the rods, respectively. The transverse peak is independent of the of the NRs

length, while the longitudinal peak is redshifted with an increasing of the NRs length.[132]

Various methods have been established for the synthesis of gold NRs. These methods are based in either an electrochemical, seedless or seeded growth approach.[133]

The seed mediated method to synthesize gold NRs was first developed by Murphy and co-workers.[134] In this method, a growth solution is prepared by adding gold salt, a weak reducing agent (ascorbic acid), a silver salt (silver nitrate) and a surfactant, hexadecyltrimethylammonium bromide (CTAB). In this solution, due to the high CTAB concentration and low pH (2.5), the ascorbic acid is unable to reduce the gold to the metallic state. The reduction of Au^{+} to metallic gold happens when citrate gold NPs seeds of about 3 nm in diameter are added to the growth solution. The metallic gold is catalyzed by the surface of the seeds and leads to the gradual change in shape from spherical to rod-like.

The NRs solutions obtained by Murphy's method present a relatively low number of rod-shaped NPs when compared with the spherical-shaped ones. In order to overcome this drawback, El-Sayed and coworkers modified Murphy's method by replacing the citrate-capped seeds by CTAB-capped seeds NPs, synthesized by chemical reduction of a gold salt with sodium borohydride.[135] This reduction reaction can be written as:

$$AuCl_4 + NaBH_4 \rightarrow Au^0 + B(OH)_3 + NaCl + H^+ \qquad (2.5)$$

Additionally, El-Sayed group added silver nitrate to the growth solution. These changes improved considerably the yield in shape in the production of gold NRs.[135] The position of the LSPR of gold NRs can be tuned by changing the concentration of seeds, ascorbic acid, silver nitrate, gold salt or CTAB in the solution.

2.3.2 Physicochemical properties of gold nanoparticles

In 1908, Gustav Mie solved Maxwell's equations for the absorption and scattering of electromagnetic radiation by spherical noble metal NPs, explaining the remarkable correlation between size and colour presented by these gold colloids.[136] He showed that when the radius of the noble metal NPs is smaller than the wavelength of light, they exhibit a strong absorption band in the visible region. This phenomenon was attributed to a small particle effect, absent in bulk metals and individual atoms. Incoming electromagnetic radiation induces the formation of a dipole in the NP, a restoring force is then set up to compensate it. This results in a resonant plasma frequency matching the electron oscillation within the NP. These oscillation modes are known as surface plasmons and are characterized by a strong field enhancement at the interface between metal and dielectric. For spherical metal NPs, much smaller than the wavelength of the exciting light, only the dipole absorption of Mie equation contributes to the extinction cross section, σ_{ext}, of the NPs.[136] The Mie theory then reduces to the following relationship:

$$\sigma_{ext} = 9\frac{\omega}{c}\epsilon_m{}^{3/2}V\frac{\epsilon_2(\omega)}{[\epsilon_1(\omega)+\epsilon_2(\omega)]^2+[\epsilon_2(\omega)]^2} \quad (2.6)$$

where $V = (4\pi/3)R^3$ is the volume of the spherical particle, ω is the angular frequency of the exciting radiation, c is the velocity of light, and ε_m is the dielectric constant of the surrounding medium (assumed to be frequency independent). $\varepsilon_1(\omega)$ and $\varepsilon_2(\omega)$ are the real and imaginary part of the dielectric function of the particle material,[137] respectively ($\varepsilon(\omega) = \varepsilon_1(\omega) + i\varepsilon_2(\omega)$).[138] Equation (2.6) shows that resonance occurs if $\varepsilon_1(\omega) \approx -2\varepsilon_m$ if ε_2 is small or weakly dependent on ω.[138]

In some metal NPs, such as gold NPs, the conduction band electron transitions push the plasma frequency into the visible part of the spectrum. Typically, a broadening of the electronic absorption spectra is observed, as a function of the aggregation state of the NPs. For aggregated NPs, Mie theory's assumption of non-interacting NPs breaks down. Instead near-field coupling between particles in close proximity and far-field dipolar coupling interactions dominate

the spectral response. The dipolar fields resulting from the plasmonic oscillation of a single NP induce plasmonic oscillations in adjacent NPs.

For non-spherical metallic NPs such as gold NRs, the plasmon resonance splits into a higher and lower energy bands corresponding to the transverse and longitudinal oscillations, respectively (Figure 2.12).[138, 139]

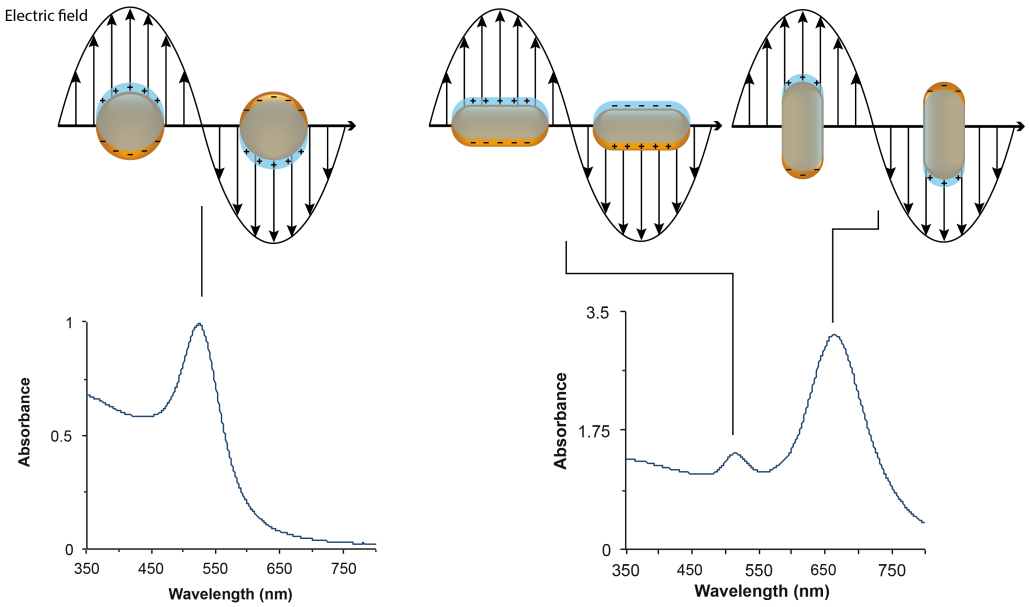

Figure 2.12 Schematic illustration of the surface plasmon resonance (top) in gold NSs and gold NRs. Corresponding electronic absorption spectra of samples in water (bottom). The orange spheres and rods represent the metal NPs and the blue represents the electron cloud.

It is hypothesised that the shift in the surface plasmon resonance occurs when the particles deviate from spherical geometry. In this case, the longitudinal and transverse dipole polarizability no longer produces equivalent resonances. Consequently, two plasma resonances appear: a broadened and redshifted longitudinal plasmon resonance and a transverse plasmon resonance. According to study by Gans, for gold NRs, the plasmon absorption splits into two bands corresponding to the oscillation of the free electrons along and perpendicular to the long axis of the rods.[140] The transverse mode shows a resonance at about 520 nm, which is co-incident with the plasmon band of

spherical particles, while the resonance of the longitudinal mode is redshifted and strongly depends on the length of the NRs.[141]

2.3.3 Surface functionalisation of gold nanoparticles

Ligand molecules that bind to the surface of the NPs are able to control the growth of the particles and are also to stabilise them, preventing them from aggregation.[142] The repulsive forces responsible for the NP stability can be of electrostatic and/or steric nature. The ligand molecules bind to the NP surface by chemisorption, electrostatic attraction or physisorption.

In order to improve the stability of the inorganic NPs, the ligand molecules on the surface of the NP can be exchanged by other ligands that bind stronger to the NP surface. This type of ligand exchange approach is commonly used on citrate-coated gold NPs, where the negatively charged citrate ions adsorbed on NP surface, stabilising the NP by electrostatic repulsion.[120]

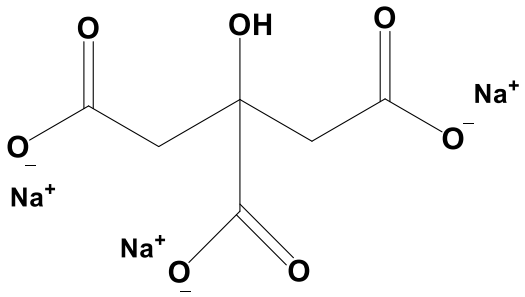

Scheme 2.1 Molecular structure of trisodium citrate.

Citrate gold NPs are stable, but they cannot be concentrated and they aggregate irreversibly in the presence of salts. The citrate coating can be replaced by ligands that bind stronger to the gold surface. In the present work, the ligands used to replace the citrate coating were: a sulphonated phosphine, Bis(p-sulfonatophenyl)phenylphosphine dihydrate dipotassium (BSPP) (Scheme 2.2), thiol-terminated PEG molecules (Scheme 2.4) and cysteine-terminated peptides (Table 4.1).

BSPP have been used to stabilise gold NPs within a wide sizes.[143, 144] BSPP-coated NPs can be precipitated by salt-induced aggregation and redispersed again in low salt concentrations. This stability allows obtaining highly concentrated solutions of NPs.

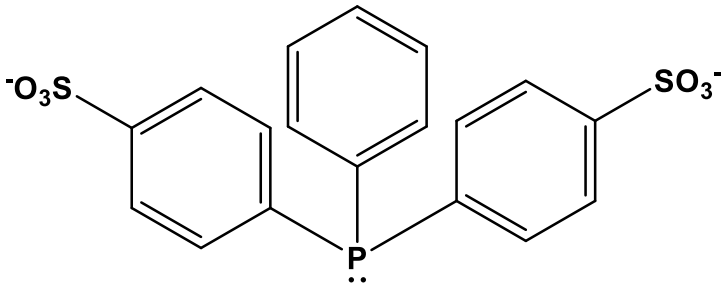

Scheme 2.2 Molecular structure of BSPP.

Furthermore, thiol-containing ligands or cysteine-terminated peptides can replace the phosphine, since the thiol groups show highest affinity to the gold surface than the phosphorus group in the phosphines.[120]

When gold NPs are coated with CTAB (Scheme 2.3), this binds to the NP surface electrostatically as a bilayer structure, which is difficult to remove and highly cytotoxic, thus limiting many potential biomedical applications.[145]

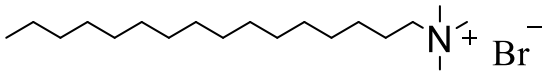

Scheme 2.3 Molecular structure of CTAB.

The NP stability is highly influenced by how densely the ligands are packed around their surface, which is determined by the molecular geometry of the ligands.

2.3.3.1 Polyethylene glycol capping based ligands

PEG is a polymer compound composed of repeating ethylene glycol units: $-CH_2-CH_2-O-$ which has several chemical properties that make it especially useful in various biological, chemical and pharmaceutical applications. PEG molecules are non-toxic and non-immunogenic – it can be attached to NP surface or conjugated to other molecules without interfering with cellular functions or target immunogenicities;[146, 147] they are soluble in a number of organic polar and non-polar solvents, as well as in water where it is heavily hydrated – it can be attached to proteins and other biomolecules decreasing their aggregation and increasing their solubility. Furthermore, NPs coated with PEG molecules show less non-specific binding to proteins and cells when compared with non-PEGylated NPs.

Heterofuctional PEG molecules, such as Alpha-Thio-omega-carboxy polyethylene glycol (SH-PEG-COOH) and (Alpha-Amino-omega-mercapto polyethylene glycol hydrochloride) SH-PEG-NH_2, can be used to confer the surface of the NPs with a negative and positive charge, respectively.

A

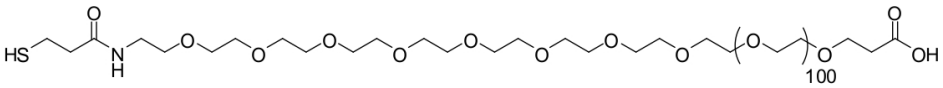

B

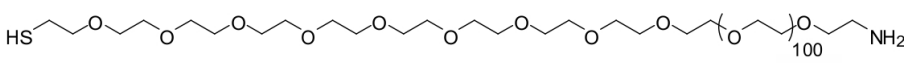

Scheme 2.4 Chemical structure of SH-PEG-COOH (A) and SH-PEG-NH_2 (B).

2.3.3.2 Cysteine-alanine-leucine-asparagine-asparagine peptide based ligands

Peptide-functionalised gold NPs combine the unique physicochemical properties of the NPs, *e.g.* optical properties of gold NPs and the ability of peptides for highly specific binding by molecular recognition. This clearly

makes peptide-functionalised NPs interesting tools for basic research and medical applications that make use of the specific functions of peptides.

Conjugation of peptides to NPs can be achieved by physisorption or chemisorption of peptides to the surface of the NPs.[120]

Levy *et al.*[148] designed a pentapeptide ligand, CALNN, which replaces the citrate ligand on the surface of the gold NPs, increasing considerably NP stability. The peptapetide, CALNN, was designed to have a strong affinity to the gold surface. Thus, the thiol group in the N-terminal cysteine of CALNN attaches covalently to the gold surface. The presence of the charged ammonium group in the vicinity of the thiol in the cysteine (C) accelerates the adsorption kinetics of a thiol group on the gold NP surface.[149] Alanine (A) and leucine (L) in positions 2 and 3 have hydrophobic side chains promote the self-assembly of the peptide on the NP surface. The C-terminal of the asparagine (N), an uncharged, but hydrophilic amino acid due to the amide group on the side chain, in position 5 can bear a negative charge due to the carboxyl termini. Additionally, CALNN-coated gold NPs retain a self-assembled dense coating that excludes water due to the presence of the hydrophobic aminoacids (A and L).[148]

Chapter 3 Materials and methods

3.1 Gold nanoparticles

The preparation of the gold NPs samples used in this thesis is described in a separate chapter, Chapter 4, which also contains their characterization.

3.2 MDCK cells experiments

3.2.1 MDCK cell culture

MDCK-II cells grown on transwell membranes form polarized monolayers with tight junctions in a short culture time, exhibiting microvilli on their apical surface.[150]

MDCK-II monolayers have been widely used to study tight junction formation and establishment of epithelial cell polarity,[151] as well as *in vitro* models to predict the permeability of drugs.[111] Furthermore, it has been show that tight junctions are crucial for the barrier function of the stratified epithelium of mammalian skin.[152] Thus, in this study MDCK-II cells were used as an *in vitro* modem system to investigate the penetration of gold NPs through skin.

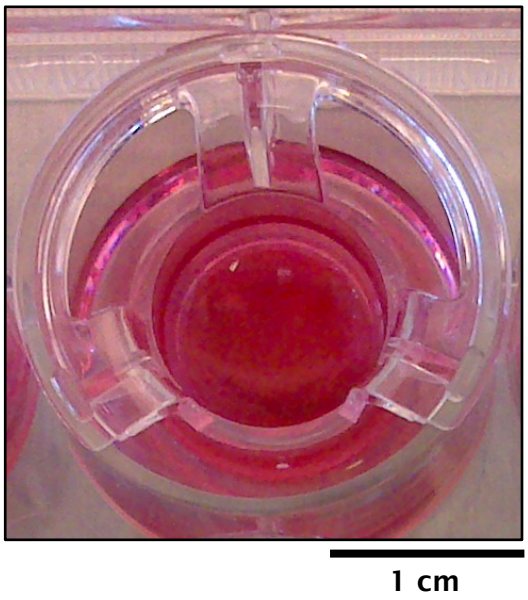

Figure 3.1 Phoptography of the MDCK-II cell culture setup.

MDCK cells were cultured in Dulbecco's modified eagle's medium (DMEM) supplemented with 10% fetal bovine serum (FBS), 2.5 mM L-glutamin and 1% Penicillin/Streptomycin. Every three days, the cells medium was replaced by fresh medium. MDCK-II cells were passaged by trypsinisation when at 80-90% of confluence. Essentially, the medium was aspirated and the cells were rinsed twice with phosphate buffered saline (PBS). A solution of trypsin/ ethylenediaminetetraacetic acid (EDTA) (0.025% trypsin and 0.01% EDTA in PBS) (2ml) was then added to the cells and the cells were incubated at 37˚C in 5% CO_2 /air for 5-10minutes to allow cell monolayer to detach. The cell resuspension was then transferred to a conical centrifuge tube and centrifuged at 1000 rotation per minute (rpm) for 3 minutes. The cells pellet was resuspended in fresh culture medium at a density of 5 x 10^5 cells/ml.

3.2.2 Exposure of MDCK-II cells to gold nanoparticles (pre-monolayer formation)

After feeding the cells into the transwell inserts, 100 µl of gold NPs solution were added to the cells on apical chamber at a density of 1 x 10^7 NPs/cell in

the case of spherical gold NPs (16.67 nM) or 1 x 10^6 NP/cell in the case of NRs (1.67 nM).

Every 24 hours, medium in the basolateral chamber was aspirated and replaced by fresh medium (600 μl).

As a control, no gold NP solution was added to one the cell wells. Instead, 100 μl of medium was added to the cells on the apical chamber, to have an equivalent volume to the other wells. As blank control, no NPs or cells, where added to one of the inserts. Instead 1.1 ml of medium was added to the cells on the apical chamber, in order to have an equivalent volume to the other chambers. Control wells underwent identical culturing and washing procedures as other wells.

TEER was measured over 10 days.

3.2.3 Exposure of MDCK-II monolayer to gold nanoparticles (post-monolayer formation)

After feeding the cells into the transwell inserts and incubated for 9 days, 100 μl of gold NPs were added to the cells on apical chamber of the transwell system at a density of 1 x 10^7 NPs/cell in the case of spherical gold NPs (16.67 nM) or 1 x 10^6 NPs/cell in the case of NRs (1.67 nM).

Every 24 hours, medium in the basolateral chamber was aspirated and replaced by fresh medium (600 μl).

Control experiments similar to the ones described in 3.2.2 were performed.

TEER was measured over 10 days and samples were analysed by TEM.

3.2.4 Transepithelial electric resistance measurements

TEER measurements on MDCK-II cells were performed using Transwell inserts on 12-well plates. In detail, 600 μl of DMEM supplemented with 10% FBS supplemented and 1% Penicillin/Streptomycin was added to each well of a 12-

well plate. Transwell inserts were placed on the reservoir and 1 ml of cell suspension (5 x 10^5 cells/ml) was seeded into each apical chamber of the transwell system. For each TEER measurement, transwell systems were removed from the incubator and allowed to equilibrate to room temperature (approximately 30 minutes). The TEER meter probe was then placed into each well (short probe in the apical chamber of the transwell insert and long probe into the basolateral chamber) (Figure 2.7) and the resistence was recorded. After the measurement, the medium in the basolateral chamber was aspirated and replaced by fresh medium (600 μl) and the transwell system was returned to the incubator. The resistance reading was corrected by subtracting the reading of the blank sample (no cells or NPs) and adjusted for the area to which the current was delivered, by multiplying by surface area of the transwell insert (1.1 cm^2). The TEER values reported are the average of three reading across each insert. Between measurements, the TEER meter probe was rinsed first with ethanol, then with Milli-Q water and finally with DMEM supplemented with 10% FBS supplemented and 1% Penicillin/Streptomycin.

TEER measurements were made every 24 hours, over 10 days for the experiments stated in Section 3.2.2 and Section 3.2.3.

3.2.5 Preparation of nanoparticle-MDCK-II cellS samples for TEM

Samples from experiment described in 3.2.3 were analysed by TEM and LM. After 24 hours of incubation with NPs, the medium in the basolateral and apical chambers were aspirated. The apical chamber was washed once with PBS and fixative (glutaraldehyde (3%) and formaldehyde (4%) in piperazine-N,N′-bis(2-ethanesulfonic acid) (PIPES) buffered (0.1 M, pH 7.2) was added to the basolateral (1ml) and apical (1ml) chambers. After overnight fixation, the fixative was removed, cell monolayers were washed twice in PIPES (0.1 M, pH 7.2) and postfixed for 1 hour in a solution containing Osmium (VIII) Oxide buffered (2%) in PIPES (0.1 M, pH 7.2). After, cell monolalyers were washed twice in PIPES buffer (0.1 M, pH 7.2) and treated with uranyl acetate for 20 minutes, dehydrated in an ascending ethanol series (30% (10 minutes), 50% (10 minutes), 75% (10 minutes), 95% (10 minutes) and 100% ethanol (twice 20 minutes)). The transwell membrane with the cells was removed from the insert

and embedded in acetonitrile for 10 minutes, 50:50 acetonitrile:Spurr resin overnight and Spurr resin for 6 h. The cell monolayers were then polymerised in fresh Spurr resin for 16 hours at 60°C and thin-sectioned into 90 nm slices, mounted 3.05 mm diameter Palladium coated, 200 mesh Copper grids and imaged on a FEI Technai12 TEM, operating at 80 kV.

3.3 Skin penetration experiments

3.3.1 Skin preparation

3.3.1.1 Preparation of human skin

Full thickness abdominal human skin was obtained from surgical resection, after having received written consent with approval by the Southampton and South West Hampshire Research Ethics Committee in adherence to Helsinki Guidelines (NRES 07/Q1704/59). The experiments were carried on immediately after skin was excised. The subcutaneous fat was carefully removed with a blade and the skin washed with PBS. For the entire study skin samples from four different donors were utilized. The skin was divided for experiments into pieces of about 915 mg each. Skin samples from 2 donors were used in the histological studies; 2-4 sections were investigated for each sample.

3.3.1.2 Preparation of mouse skin

C57/BL6 mice were bred at the University of Southampton (Certificate of designation number 70/2906). Dorsal skin was removed from 1 day old mice after euthanasia by a schedule one method following the UK Animals (Scientific Procedures) Act 1986. Briefly, a cut was made at the base of the mouse torso with sterile scissors. The scissors were then used to gently peel away the skin toward the frontal part of the mouse. Mouse skin was then washed with PBS

buffer and used in further experiments. For the entire study, the skin of 22 mice was used. The skin was divided for experiments into pieces of about 45 mg each. Skin samples from 6 mice were used in the integrity studies; 2-4 sections were investigated for each sample.

3.3.2 Assessment of skin integrity

3.3.2.1 Assessment of integrity of human skin penetration setup

Human skin, cleaned and divided into small pieces of about 915 mg, was placed in a 6-well microplate with culture medium (Roswell Park Memorial Institute (RPMI) medium + 5% Penicillin/Streptimycin + 10% Foetal Calf Serum; 600 µl per well) was added in order to immerse the dermis and leave the epidermis at the air-medium interface (Figure 3.2). Samples were then incubated for 12, 24 and 48 hours at 37˚C in 5% CO_2 /air. A control sample, *i.e.* human skin immediately processed for TEM or LM analysis after excision, was also prepared.

3.3.2.2 Assessment of integrity of mouse skin penetration setup

The same penetration setup used for human skin (Figure 3.2) was tested using mouse skin for the period 24 h. Mouse skin, cleaned and divided into small pieces of about 19 mg, was placed in a 6-well microplate with culture medium (RPMI medium + 5% Penicillin/Streptimycin + 10% Foetal Calf Serum; 300 ul per well) was added in order to immerse the dermis and leave the epidermis at the air-medium interface. Samples were then incubated for 24 hours at 37˚C in 5% CO_2 /air. The setup illustrated in Figure 3.3 was tested for periods of 6 and 24 h. Essentially, the cleaned mouse skin was evenly cut into smaller pieces and placed in 12 mm transwell insert with DMEM medium (DMEM + 5% Penicillin/Streptimycin + 10% Foetal Calf Serum; 400 µl per well) in the basolateral chamber. Samples were then incubated for 6 and 24 hours at 37˚C in 5% CO_2 /air. A control sample, *i.e.* mouse skin immediately processed tor TEM or LM analysis after excision, was also prepared.

3.3.2.3 Preparation of skin samples for Transmission electron microscopy and light microscopy

For histological studies, human and mouse skin, previous cleaned and divided into small pieces, was fixed with 10% formaldehyde, embedded in paraffin, hematoxylin and eosin stain stained, cut into 0.5 µm sections, mounted in glass slides and observed in a Nikon Eclipse 600 equipped with a Nikon Coolpix 950 digital camera. For TEM studies, the skin was cut into small pieces of about 3-4 mm^3 each. To avoid contamination of the deeper layers of the skin with NPs found in the surface of the skin, the following cutting procedure was followed: skin was orientated with the epidermis facing down and each transversal cut was made from the dermis to the epidermis using a clean sterilized blade for each cut. Skin pieces were then fixed overnight in a solution containing glutaraldehyde (3%) and formaldehyde (4%) in PIPES buffered (0.1 M, pH 7.2). Tissues were then washed twice in PIPES (0.1 M, pH 7.2) and postfixed for 1 hour in a solution containing Osmium (VIII) Oxide buffered (2%) with PIPES (0.1 M, pH 7.2). Next, tissues were washed twice in PIPES buffer (0.1 M, pH 7.2) and treated with uranyl acetate for 20 minutes. Tissues were dehydrated in an ascending ethanol series (30% (10 minutes), 50% (10 minutes), 75% (10 minutes), 95% (10 minutes) and 100% ethanol (twice 20 minutes)) and embedded in acetonitrile for 10 minutes, 50:50 acetonitrile:Spurr resin overnight and Spurr resin for 6 h. Samples were then polymerised in fresh Spurr resin for 16 hours at 60˚C. Specimens were subsequently thin-sectioned into 90 nm slices, mounted 3.05 mm diameter Palladium coated, 200 mesh Copper grids and imaged on a FEI Technai12 TEM, operating at 80 kV.

3.3.3 Assessment of gold nanoparticles penetration through skin

Skin penetration experiments were performed using different penetration setups and incubation times for human and mouse specimens. The reason for that was that mouse skin did not maintain its integrity when cultured using the same setup and incubation time as human skin

Chapter 6, section 6.2, shows an extensive evaluation of the human and mouse skin integrity when cultured using different setups an incubation times.

The optimized setups ensured that human and mouse skin integrity was preserved, for the designated incubation times.

3.3.3.1 Incubation of human skin with gold NPs

A rubber O-ring (I.D. = 4.34 mm ± 0.13 mm; W = 3.53 mm ± 0.10 mm) was secured with seal Vaseline on the top of each piece of human skin of about 915 mg. Human skin pieces were then placed in a 6-well microplate with culture medium (RPMI medium + 5% Penicillin/Streptimycin + 10% Foetal Calf Serum; 600 µl per well) was added to immerse the dermis and leave the epidermis at the air-medium interface (Figure 3.2).

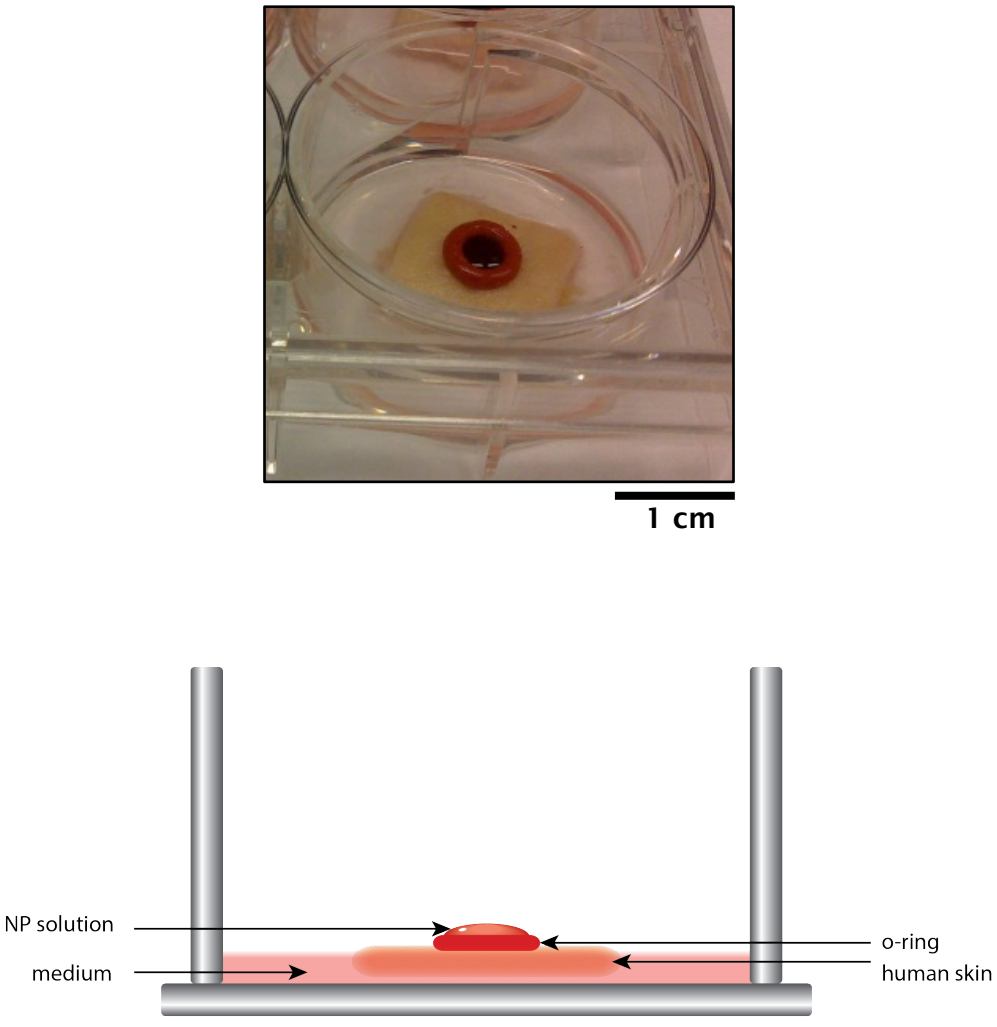

Figure 3.2 Photography (top) and schematic illustration (bottom) of the penetration setup used for human skin.

Each O-ring was filled with 20 µl of either 100 nM gold NSs or 14 nM gold NRs solutions. One of the skin pieces was used as a control; the O-ring was filled with Milli-Q water and exposed to the same conditions as the NP-treated skin pieces. The skin was then incubated for 24 hours at 37°C in 5% CO_2 /air.

3.3.3.2 Incubation of mouse skin with gold NPs

A rubber O-ring (I.D. = 4.34 mm ± 0.13 mm; W = 3.53 mm ± 0.10 mm) was secured with seal Vaseline on the top of each piece of mouse skin of about 45 mg. Mouse pieces were then placed in 12 mm transwell insert with DMEM medium (DMEM + 5% Penicillin/Streptimycin + 10% Foetal Calf Serum; 400 µl per well) in the basolateral chamber (Figure 3.3).

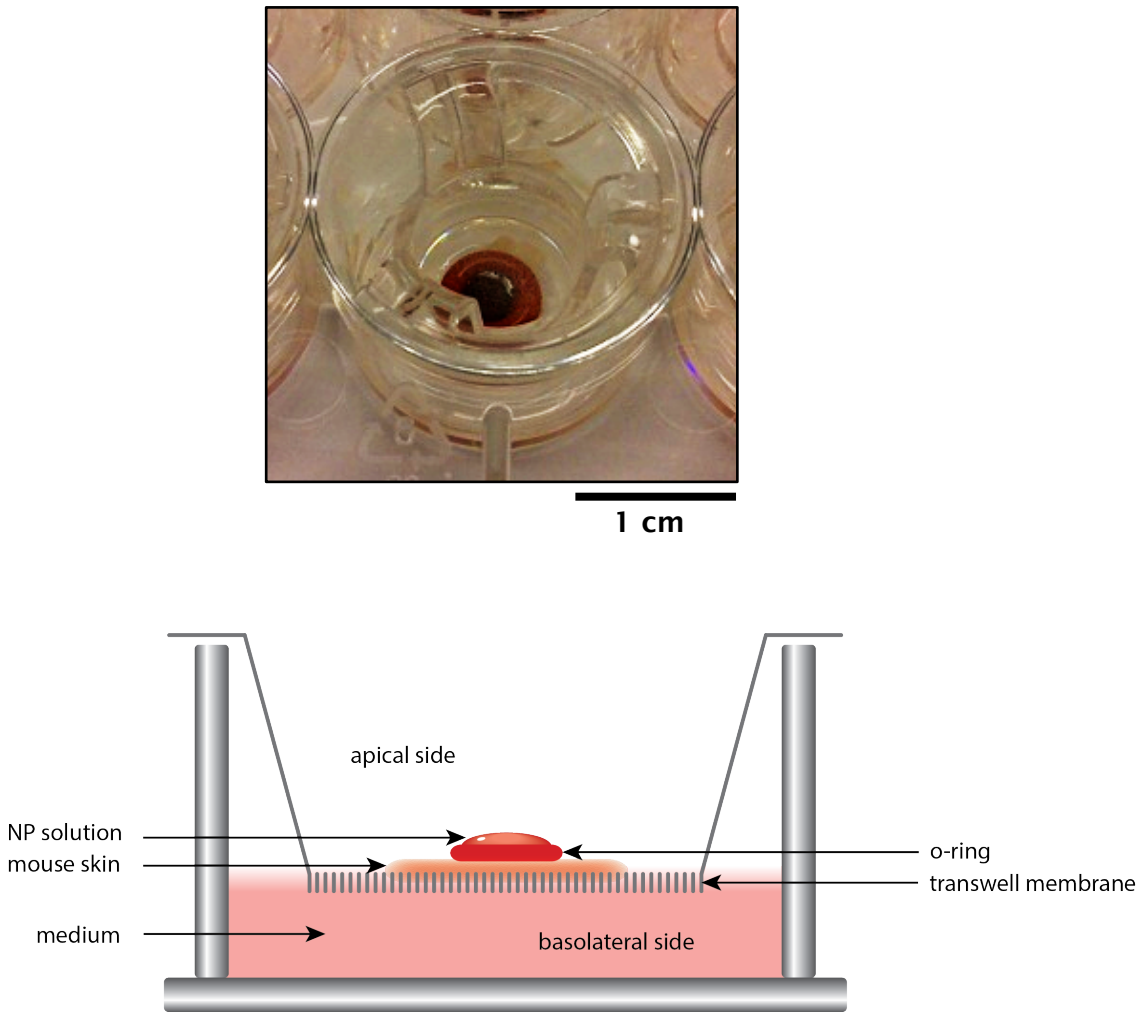

Figure 3.3 Photography (top) and schematic illustration (bottom) of the penetration setup used for mouse skin.

Similarly to the human skin experiment (section 3.3.3.1), each O-ring was filled with 20 μl of either 100 nM spherical gold NPs or 14 nM gold NRs solutions and also one of the skin pieces was used as a control; the O-ring was filled with Milli-Q water and exposed to the same conditions as the NP-treated skin pieces. The skin was then incubated for 6 hours at 37°C in 5% CO_2 /air.

3.3.3.3 Inductively coupled plasma atomic emission spectroscopy of gold nanoparticle-treated mouse and human skin

After incubation, the gold NPs solution that remained in the ring was collected and the skin was washed twice with 20 μl of Milli-Q water. The ring was carefully removed from the skin and the skin underneath the ring was separated. For ICP-AES measurements, the skin was then tape-stripped 6 times with 3M™ Micropore™ Medical Tape and dissolved in aqua regia (10%). For the human skin, a microwave digester was used to facilitate the process. Once the samples were digested, Milli-Q water was used to dilute them to 10 ml each. Finally, ICAP 6300 duo Spectrophotometer was used to measure the amount of gold present in the skin specimens and gold NP solutions in part per million (ppm).

3.3.3.4 Preparation of nanoparticle-skin samples for TEM imaging and EDX analysis

Gold NPs skin penetration after was investigated by TEM. After mouse and human skin were treated with gold NP for 6 and 24 hours, respectively, the skin samples underneath the O-ring was cut into small pieces of about 3-4 mm^3 each. To avoid contamination of the deeper layers of the skin with NPs found in the surface of the skin, the following cutting procedure was followed: skin was orientated with the epidermis facing down and each transversal cut was made from the dermis to the epidermis using a clean sterilized blade for each cut. For electron microscopy, tissue specimens were fixed overnight in a solution containing glutaraldehyde (3%) and formaldehyde (4%) in PIPES buffered (0.1 M, pH 7.2). Tissues were then washed twice in PIPES (0.1 M, pH

7.2) and postfixed for 1 hour in a solution containing Osmium (VIII) Oxide buffered (2%) with PIPES (0.1 M, pH 7.2). Next, tissues were washed twice in PIPES buffer (0.1 M, pH 7.2) and treated with uranyl acetate for 20 minutes. Tissues were dehydrated in an ascending ethanol series (30% (10 minutes), 50% (10 minutes), 75% (10 minutes), 95% (10 minutes) and 100% ethanol (twice 20 minutes)) and embedded in acetonitrile for 10 minutes, 50:50 acetonitrile:Spurr resin overnight and Spurr resin for 6 h. Samples were then polymerised in fresh Spurr resin for 16 hours at 60˚C. Specimens were subsequently thin-sectioned into 90 nm slices, mounted 3.05 mm diameter Palladium coated, 200 mesh Copper grids and imaged on a FEI Technai12 TEM, operating at 80 kV. For EDX analysis, sections were mounted on 3.05 mm diameter 200 mesh Nickel grids and the gold content was analysed on a on a FEI Technai12 TEM equipped with EDAX X-ray spectrometer.

3.3.3.5 Photoluminescence microscopy of gold nanoparticle-treated mouse skin

After the mouse skin was treated for 6 hours with gold NP the skin samples were fixed for 24 hours in a 10% buffered formalin solution at room temperature, using 10 times the volume of fixative to the volume of specimen. Tissues were dehydrated in an ascending ethanol series (50% (1 hour), 70% (1 hour), 90% (1 hour) , 100% (twice 1 hour) and 100% ethanol (twice 2 hours)) and then placed in Xylene (three times 1 hour and 30 minutes each) and then in paraffin (1 hour and 30 minutes followed by three times 1 hour each). Finally samples were embedded into a block and let to set for 1 hour in a freezer plate. Specimens were subsequently thin-sectioned into 14 μm slices, mounted in cover slips and let dry overnight. Sections were dewaxed in Xylene (twice 10 minutes), 100% ethanol (twice 5 minutes), 70% ethanol (twice 5 minutes) and water (5 minutes). Slides were then dried at room temperature and coverslips were mounted on the top of the glass slides with Mowiol.

Paraffin sections where used rather than frozen sections because paraffin blocks yield better histological preservation, allow the used of larger pieces of tissue and are easier to storage.[153]

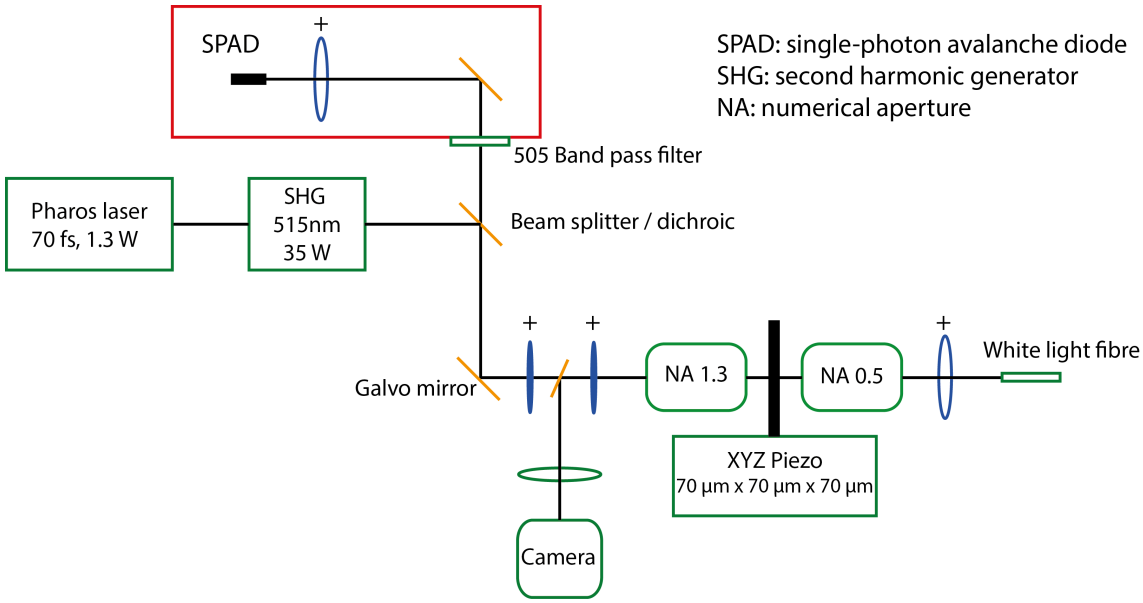

Figure 3.4 Schematic illustration of the PL microscope.

PL measurements were performed using the custom-built near infrared laser scanning PL microscope illustrated in Figure 3.4.

Illumination was done at 515nm using the second-harmonic of a 1030nm single-unit integrated femtosecond laser (Pharos, Light Conversion Ltd.) emitting pulses of 100 fs duration at 76 MHz repetition frequency. Emitted light was spectrally filtered using a bandpass filter between 500nm-510nm to detect the anti-Stokes fluorescence emission mediated by the surface plasmon resonance of the gold NSs. This emitted light was collected by a single photon avalanche diode (Perkin Elmer Inc.). Labview program was used to control the piezo, acquire the counts and construct the image. Emission from a single gold NS corresponds to approximately 100 counts in the image.

The PL microscopy setup was assembled by Dr. Otto L. Muskens from the Faculty of Physical and Applied Sciences, University of Southampton, UK.

Chapter 4 Synthesis and characterization of gold nanoparticles

Seven types of gold NPs were used to study the interaction between gold NPs and MDCK-II cells, as well as NP penetration through human and mouse skin. These particles differ between each other in terms of charge, shape and surface functionalisation.

Gold NSs (15 nm, diameter) and gold NRs (20 x 55 nm, width x length) were prepared following well-established protocols[135, 154] and coated with thiol-containing PEG molecules, with either an amino (positively charged) or a carboxyl (negatively charged) termini. Furthermore, gold NSs (15 nm, diameter) were functionalised with CALNN and CALNN-containing CPPs.

In the present chapter, the synthesis and characterization of the colloidal NPs are addressed.

4.1 Preparation of gold nanoparticles

4.1.1 Synthesis of gold nanoparticles

4.1.1.1 Synthesis of spherical gold nanoparticles

Sodium citrate-stabilised gold NS with 15 nm diameter were prepared using the Turkevich method.[127] In detail, a solution of trisodium citrate (19.5 mM, 2.5 ml) was brought to boil and quickly added into a boiled solution of sodium tetrachloroaurate (III) dihydrate (0.5 mM, 25 ml) while stirring vigorously. The colour of the solution changed from pale yellow to colourless, then to purple and finally to deep red indicating the formation of gold NSs. The reaction mixture was boiled and stirred for additional 5 minutes, cooled down at room temperature while stirring and purified by filtration through a 0.45 μm syringe filter. Citrate-coated gold NSs were capped with BSPP *via* ligand exchange reaction. Basically, BSPP (10 mg; molecular weight (Mw) = 498.6 g/mol) was added to a solution of citrate-stabilised gold NPs (27.5 ml) and the mixture was stirred overnight at room temperature. BSPP-coated NSs were precipitated with sodium chloride (50 mg), purified by one centrifugation step (3500xg (gravitational acceleration), 5 minutes, 20 °C) and redispersed by sonication in 100 μl of Milli-Q water. BSPP-coated gold NPs were characterised by TEM using 3.05 mm diameter Carbon coated 400 mesh Copper grids, UV-Visible spectroscopy dynamic light scattering (DLS) and zeta potential. The concentration of 15 nm gold NP was determined using the Beer-Lambert law by measuring the maximum UV-Visible absorption of the gold colloid and using an extinction coefficient of 3.6×10^8 cm^{-1} M^{-1}.[155, 156]

4.1.1.2 Synthesis of gold nanorods

Gold NRs were synthesised using an optimized seed mediated growth method.[135] In detail, a seed solution was prepared by mixing CTAB (0.2 M, 1

ml) with sodium tetrachloroaurate (III) dihydrate (5 mM, 1 ml). Then, an ice-cold solution of sodium borohydride (0.01 M, 0.5 ml) was added dropwise to the mixture while stirring vigorously. The colour of the solution changed from dark yellow, to colourless and then to light brown, indicating the formation of the spherical gold NPs. The solution was stirred for 2 minutes and used immediately after. A growth solution was prepared by mixing an aqueous solution of CTAB (0.2 M, 14.24 ml) with sodium tetrachloroaurate (III) dihydrate (5 mM, 2 ml) and silver nitrate (5 mM, 0.18 ml) at 35 °C. While stirring at 250 rpm, a L-ascorbic acid solution (78.8 mM, 160 μl) was added to the mixture. The colour of the growth solution changed from dark yellow to colourless. 30 seconds after the L-ascorbic acid addition, 16 μL of the seed solution were injected into the growth solution. The solution was kept unstirred at 35 °C for 4 hours. The colour of the solution changed from colourless to blue/green over that period. The gold NR solution was purified by two centrifugation steps (10000xg, 20 minutes, 22 °C) and redisperse in 5 ml of Milli-Q water. Gold NRs were characterised by TEM using 3.05 mm diameter Carbon coated 400 mesh Copper grids and UV-Visible spectroscopy.

4.1.2 Surface capping of gold nanoparticles

4.1.2.1 Capping with polyethylene glycol capping based ligands

4.1.2.1.1 Spherical gold nanoparticles

A freshly prepared SH-PEG-COOH or SH-PEG-NH_2 aqueous solution (5 mg/ml, 200 μl, Mw = 5000 Dalton) was added to a solution of BSPP-coated gold NSs (5 nM, 10 ml), while stirring. The mixture was incubated for 2 hours at room temperature while shaking at 500 rpm and then overnight at 4 °C. Functionalised gold NPs were purified by three steps of centrifugation (25000xg, 15 minutes, 10 °C) and redispersed by sonication in 100 μl of Milli-Q water. Functionalised gold NSs were characterised by TEM using 3.05 mm diameter Carbon coated 400 mesh Copper grids, UV-Visible spectroscopy, DLS and zeta potential. The concentration of 15 nm gold NP was determined using

the Beer-Lambert law by measuring the maximum UV-Visible absorption of the gold colloid and using an extinction coefficient of 3.6×10^8 cm^{-1} M^{-1}.[155, 156]

4.1.2.1.2 Gold nanorods

A freshly prepared SH-PEG-COOH or SH-PEG-NH_2 aqueous solution (0.5 mg/ml, 2 ml, Mw = 5000 Dalton) was added to a 2 ml solution of gold NRs (section 4.1.1.2), while shaking at 500 rpm. The mixture was sonicated for 30 seconds and shaken overnight at 500 rpm at room temperature. After, the excess of PEG was purified by one centrifugation step (10000xg, 16 minutes, 20°C) and redispersed in a freshly prepared aqueous solution of SH-PEG-COOH or SH-PEG-NH_2 (0.25 mg/ml, 4 ml, Mw = 5000 Dalton). The mixture was incubated for 4 hours at room temperature while shaking at 500 rpm. Finally, PEGylated gold NRs were purified by two steps of centrifugation/decantation (10000xg, 16 minutes, 20°C) and redispersed by sonication in 100 μl of Milli-Q water. Functionalised gold NRs were characterised by TEM using 3.05 mm diameter Carbon coated 400 mesh Copper grids, UV-Visible spectroscopy and zeta potential.

4.1.2.2 Functionalisation with CALNN peptide-based ligands

The surface of spherical gold NPs was functionalised with CALNN, 99% CALNN - 1% CALNNTat and 99% CALNN – 1 % CALNNR_7 peptides, characterised in Table 4.1, through the thiol group of the cysteine. In all the cases a 5000:1 peptide to NP molar ratio was used. Briefly, the following aqueous solutions: CALNN (0.5 mg/ml, 133.4 μl), CALNN - CALNNTat mixture (CALNN (0.5 mg/ml, 132.0 μl) + CALNNTat (0.1 mg/ml, 26.7 μl)) and CALNN - CALNNR_7 misture (CALNN (0.5 mg/ml, 132.0 μl) + CALNNR_7 (0.1 mg/ml, 20.35 μl)) were injected into a solution of BSPP-coated gold NSs (5 nM, 5 ml) whilst shaking at 500 rpm. In order to avoid non-specific biding, an aqueous solution of polyethylene glycol sorbitan monolaurate (Tween20) (1 wt%, 150 μl) was added to the NP solution immediately after the addition of the peptides. After 4 hours shaking at room

temperature, the reaction mixture was centrifuged (25000xg, 10 minutes, 22˚C) and redisperse in 5 ml of water and CALNN (0.5 mg/ml, 133.4 μl), or CALNNTat (CALNN (0.5 mg/ml, 132.0 μl) + CALNNTat (0.1 mg/ml, 26.7 μl) or CALNNTat (CALNN (0.5 mg/ml, 132.0 μl) + $CALNNR_7$ (0.1 mg/ml, 20.35 μl). Again, an aqueous solution of Tween20 (1 wt%, 150 μl) was then added to the mixtures. The solutions were incubated overnight at room while shaking at 500 rpm and purified from the excess peptide by three centrifugation steps (25000xg, 15 minutes, 22˚C) and redispersed in phosphate buffer (0.01M, pH=7.2) prior to the characterisation. Functionalised gold NSs were characterised by TEM using 3.05 mm diameter Carbon coated 400 mesh Copper grids, UV-Visible spectroscopy and gel electrophoresis. The concentration of 15 nm gold NP was determined using the Beer-Lambert law by measuring the maximum UV-Visible absorption of the gold colloid and using an extinction coefficient of 3.6×10^8 cm^{-1} M^{-1}.[155, 156]

Table 4.1 Characterization of the peptides: CALNN, CALNNTat and $CALNNR_7$.

Peptide	Single letter code	Molecular weight	Isoelectric point	Net charge
CALNN	CALNN	533.61 g/ml	5.33	0
CALNNTat	CALNNGRKKRRQRRRPQ	2137.51 g/ml	12.71	8
$CALNNR_7$	CALNNRRRRRRR	1626.92 g/ml	12.80	7

4.2 Characterization of spherical gold nanoparticles

4.2.1 Characterization of BSPP-stabilised gold nanoparticles

Spherical gold NPs were prepared following the citrate reduction method,[126-129, 154, 157-159] as described in section 4.1.1.1. The synthesis involved the addiction of trisodium citrate to a boiled solution of tethracloroauric acid. Immediately after the addition of the sodium citrate solution, the colour of the tethracloroauric acid solution changed from deep-yellow to colourless, indicating that the gold ions (Au^{3+}) were reduced to neutral gold atoms (Au^{0}).[160] In the following 5 minutes of reaction, the solution became dark blue and then wine-red, indicating the formation of stable gold NPs[126-128]. The reaction between the trisodium citrate and the tetrachoaurate acid was terminated within 5 minutes and the wine-red colour of the solution remained unchanged after that period.

Turkevich method[127] allows the synthesis of NSs with different diameters, by simply adjusting the molar ratio between the gold precursor and the citrate reductant in the reaction.[129, 157] The pH of the reacting mixture and the gold salt concentration have an important role in the formation of gold NPs. Ji *et al.*[157] reported that initial solutions with different citrate-to-gold ratios displayed different pH values, which affected the reaction mechanism of the NPs formation. It was found that pH ≥ 6.5 led to more monodisperse gold NPs through a reaction mechanism that did not involve aggregates as intermediates. Moreover, Zabetakis *et al.*[161] studied the effect of high gold salt concentrations on the size and dispersity of gold NPs. They showed that an initial concentration of gold salt lower than 0.6 mM leads to the formation of highly monodispersed gold NSs for a citrate-to-gold ratio of 3.5 to 17.[161] They presume that this occurs because, at gold salt concentrations lower than 0.6 mM, the total electrolyte concentration is still low enough at high citrate-to-gold ratios, so that there is no occurrence of coagulation, which would lead to size increase.

Here, the synthesis of gold NPs was carried on using a concentration of gold salt of 0.5 mM and a citrate-to-gold ratio of 3.9. A representative TEM image, corresponding size-distribution histogram and UV-Visible spectrum of those NPs are shown in Figure 4.1 (top row). The size-distribution histogram was obtained using ImageJ software, by measuring the diameter the NPs in TEM images. The average diameter of the citrate-stabilised gold NS was 14.82 ± 0.02 nm (average ± standard error (SE)).

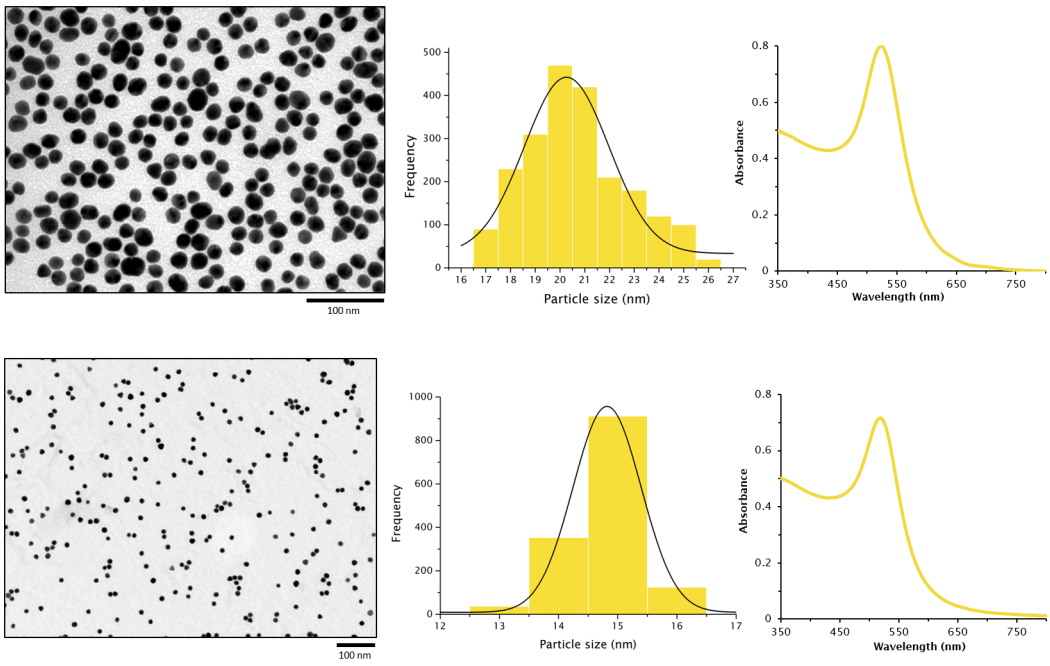

Figure 4.1 TEM image, size-distribution histogram and UV-Visible spectrum of citrate-stabilised gold NSs prepared using a citrate-to-gold ratio of 2.5 (top row) and 3.9 (bottom row).

The UV-Visible spectrum of the citrate-coated gold NPs exhibits a unique and sharp extinction peak at 519 nm, well-reported characteristic of mono-dispersed 15 nm gold NPs.[130, 136, 158, 162, 163]

In general, for concentrations of gold salt lower than 0.8 mM, the NSs diameter increases or decreases with the decreasing or increasing amount of citrate in

solution, respectively.[161] Decreasing the size of the NPs by adding a higher amount of citrate, reduces almost all precursor instantaneously in solution, leading to nucleation. Since almost all the nuclei are formed together, the size of the NPs formed is smaller and the citrate concentration being in excess should cap the NPs, producing stable monodispersed spherical NPs. However, it has been shown that the experimental results are not in agreement with this theoretical expectation, showing the lower polydespersity of gold NPs when the citrate-to-gold ratio is lower than 3.5.[161] This implies that some other factor is also contributing to morphological control of NPs, possibly the rate of citrate addition, and consequently the reaction pH, since the synthesis is not only thermodynamically controlled but also kinetically.[157]

Figure 4.1 (bottom row) shows a representative TEM image, size-distribution histogram and UV-Visible spectrum of gold NPs synthesized using a citrate-to-gold ratio of 2.5.

The size-distribution histogram showed an average diameter of 20.72 ± 0.14 nm (average ± SE) for the citrate-stabilised gold NSs using a citrate-to-gold ratio of 2.5. The TEM image and size-distribution histogram confirm the poly-dispersity of the sample.[136, 159, 163] The slightly redshift of the extinction peak, from 519 nm to 523 nm, when the size of the gold NSs increases from 15 nm to 20 nm is, according to Mie's theory, the result from the NPs larger diameter.[136]

Increasing the size of the NPs by adding a lower amount of citrate, reduces the number of nucleation sites[129, 154] Since less amount of gold precursor is involved in the nuclei formation, more gold precursor is available for the growth phase, resulting in the formation of larger NSs. Increasing the size of the NPs, boosts the NPs diameter-to-ligand length ratio. This, in conjunction with a lower overall number of citrate capping ions, can lead to insufficient stabilisation of the NPs surface. It has been shown that non-stable NPs will eventually clump together, resulting in NP aggregation.[161]

The criteria used to judge the stability of all gold NPs samples used in this thesis included: a) the experimental observation for large aggregates in

sample, *i.e.* visible aggregates floating in the sample or particles settle down with time, b) the UV-Visible spectroscopy examination for changes (*e.g.* redshift, broadening) in the plasmon band and c) the TEM investigation for smaller aggregates and size or shape alterations.

As it has been shown, the Turkevich method[127] allows the fast and easy synthesis of size-monodespersed gold colloids, when using certain citrate-to-gold ratios.[161] However, citrate-stabilised gold NPs can easily aggregate irreversibly in PBS buffer, losing their unique physicochemical properties[136, 159, 164] This aggregation is caused by the weak electrostatic stabilisation of the NPs surface by the citrate ions.[164, 165] Basically, in the presence of salts (*e.g.* sodium chloride), citrate-coated NPs surface charge becomes neutral, causing NPs to aggregate irreversibly. As a result, the solution colour changes from red to blue.

To retain NPs stability, the versatile surface chemistry of gold NPs allows them to be coated, *via* ligand exchange reaction,[164, 165] with ligands that can strongly bind to the gold surface. Schmid *et al.*[166] showed that replacing the citrate ions (Scheme 2.1) by BSPP ligand (Scheme 2.2) results in NPs with improved stability, when compared to the citrate-coated NPs. In BSPP-coated gold NPs, the phosphorous group of the BSPP contributes two electrons to the gold surface to make a bond. This bond is not as strong as a thiol bond, but it is also not electrostatic, as in the case of citrate.[167, 168] For this reason, when the NSs are coated with BSPP the aggregation in the presence of NaCl is reversible,[169, 170] *i.e.* the NPs can be brought back to solution upon addition of water, recovering their distinguishing physicochemical properties. Hence one can redissolve the particles once precipitated with salt. The initially aggregation happens because the charge on the sulphonate groups is screened by the salt. Once the salt concentration is reduced, this screen is lost and the particles recover their stability. Therefore, to increase the NPs stability and increase their concentration in solution, 15 nm citrate-coated NSs, were capped with BSPP.

Figure 4.2 shows representative TEM images, size histograms and UV-Visible spectrum of gold NPs coated with BSPP.

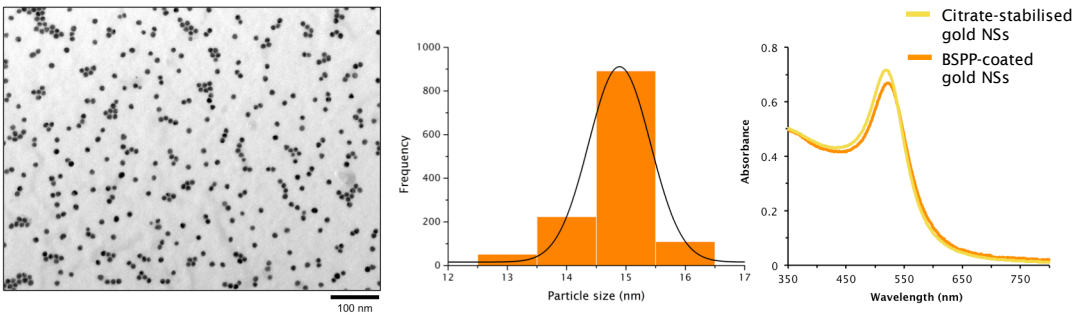

Figure 4.2 TEM image, size-distribution histogram and UV-Visible spectrum of 15 nm BSPP-coated gold NSs.

The replacement of citrate with BSPP resulted in a subtle redshift of the plasmon band[159] of gold NSs, from 519 to 521 nm (UV-Visible spectrum in Figure 4.2), as predicted by Mie's theory[136]. The gold core size of the gold NPs was unaltered with the ligand exchange, as it can be seen in the TEM image and respective size-distribution histogram, with an average of 14.82 ± 0.02 nm (average ± SE).

4.3 Characterization of gold nanorods

NRs were synthesised following a seeded surfactant-mediated protocol.[135] In detail, small gold NSs are prepared using a strong reducing agent (sodium borohydride) and CTAB (Chapter 2, Scheme 2.3), as a stabiliser. These seeds are added to a solution of tetrachloroauric acid, a weak reducing agent (ascorbic acid), silver nitrate, as well as a cationic surfactant (CTAB). Briefly, the ascorbate anion transfers electrons to the seeds, which then reduce the gold ions to form a gold shell, which grows in a longitudinal direction producing a rod-like shape.[171]

The mechanism of formation of the NRs is not yet established. $AuCl_4^-$ can be reduced to Au^0 via two different pathways: reduction of $AuCl_4^-$ to $AuCl_2^-$ via reaction 4.1, followed by spontaneous desprotonation of $AuCl_2^-$ in the gold surface (reaction 4.2); or by the direct discharge of $AuCl_2^-$ via electron transfer at the surface of the gold seeds (reaction 4.3).[171]

$$AuCl_4^- + 2e^- \rightleftarrows AuCl_2^- + 2Cl^- \quad (4.1)$$

$$3AuCl_2^- + 2e^- \rightleftarrows AuCl_4^- + 2Au^0 + 2Cl^- \quad (4.2)$$

$$AuCl_2^- + e^- \rightleftarrows 2Au^0 + 2Cl^- \quad (4.3)$$

In the presence of CTAB, ascorbic acid can reduce $AuCl_4^-$to $AuCl_2^-$, however, no colloidal gold is formed, disproportionation of $AuCl_2^-$–CTAB does not occur (reaction (4.2)) and the solution of $AuCl_2^-$-CTAB remains stable. Consequently, the reduction of $AuCl_2^-$ should happen through electron transfer at the surface of the electron-rich gold seeds (reaction 4.3). The reduction of $AuCl_2^-$ in the presence of CTAB can be described by the reaction:

$$AuCl_2^- - CTAB_{mic} + Au_m^- \rightleftarrows Au_{m+1} - CTAB_{mic} + CTAB_{mic} + 2Cl^- \quad (4.4)$$

A simple approach for the NRs formation is described in the following paragraphs. The $AuCl_4^-$ ions are bound to the CTAB micelles, displacing the Br^- ions. The $AuCl_4^-$ ion is reduced to $AuCl_2^-$ by ascorbate on the micelle surface. The transport of gold ions to the growing seed particles is controlled by the collision of $AuCl_2^-$-loaded cationic micelles with the micelle-coated gold seed. Those interactions may discharge the gold ions.[171] The rate of this reaction is controlled by the collision of micelles, which is faster at the tips

than the sides of the NR, leading to the longitudinal growth of the NR. It has been hypothesized that Ag^+ is adsorbed at the particle surface in the form of silver bromide (Br^- coming from CTAB) and restricts the growth of the $AgBr$ passivated crystal facets.[171]

By adjusting the concentration of the gold seeds, gold salt, silver salt and ascorbic acid, the aspect ratio of gold NRs can be tuned. An increase in the amount of gold seeds or gold salt concentration produces a redshift in the longitudinal plasmon band position.[133] An increased concentration of ascorbic acid leads to a decreased NR length and shape yield. By adjusting the silver salt or gold seed concentration, the longitudinal plasmon band can be tuned up to 825nm, corresponding to an aspect ratio of approximately 4.5. Adjusting the NRs size will cause variations in their optical properties, which will be reflected in the colour of the NRs colloidal solutions.[133]

In this study, the gold seeds were prepared by sodium borohydride reduction in CTAB. The concentration of CTAB used was 0.2M and the gold-to-sodium borohydrade molar ratio was 1. The typical size of these seeds is 2-4 nm in diameter with plasmon peak at around 510 nm, giving a characteristic brown colloidal solution.[135]

NRs growth solution was prepared using again a CTAB concentration of 0.2 M and molar ratios of 1.26 and 0.09 of ascorbic acid-to-gold precursor and silver-to-gold precursor, respectively. The characterization of the CTAB-stabilised NRs is shown in Figure 4.3.

The synthesised NRs had average length of 55.29 ± 0.36 nm (average ± SE) and width of 21.48 ± 0.13 nm (average ± SE) (length x width). The NRs were reasonably monodisperse, as it can be seen on the TEM image and confirmed by the size-distribution histograms. Only a very small number of spherical or cubical NPs were found in the samples, when compared with the number of NR, demonstrating the high yield of the reaction.

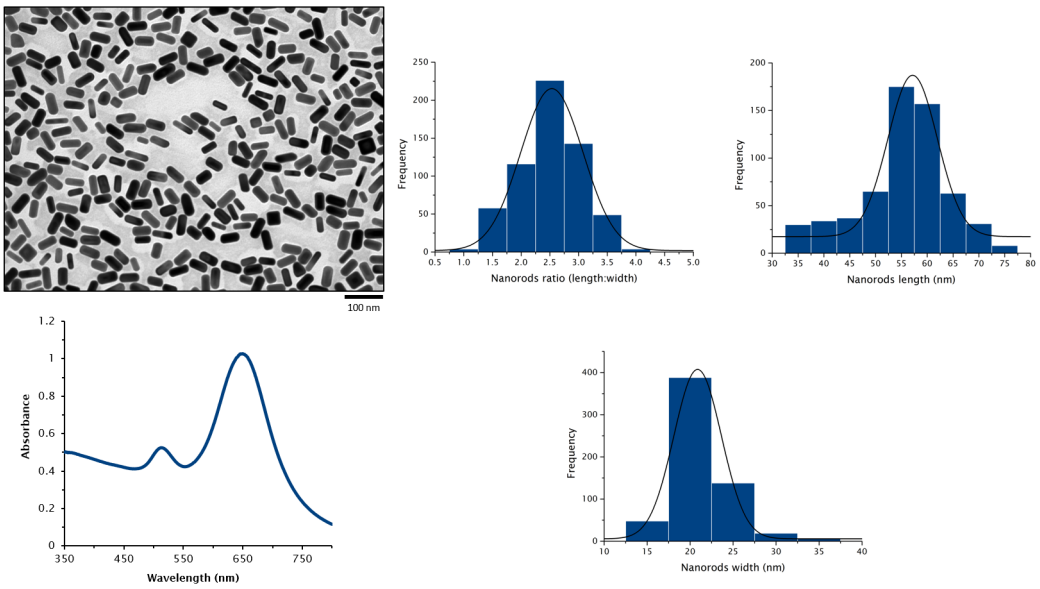

Figure 4.3 TEM image, size-distribution histograms and UV-Visible spectrum of CTAB-stabilised gold NRs.

4.4 Characterization of surface capped gold nanoparticles

The biomedical applications of gold NPs, requires that their surface is protected and/or modified as uncoated NPs may agglomerate and are rapidly cleared out from the body by the mononuclear phagocyte system.[172]

Modification of gold NPs can tailor the surface properties, such as surface charge, biocompatibility and solubility. Various functional ligands have been used to coated gold NPs, including citrate,[173] amines,[174] nucleic acids,[175] peptides,[176] antibodies,[177] and lipids,[178] as well as several polymers such as polysaccharides, polyacrylamide, poly(vinyl alcohol), poly(N-vinyl-2-pyrrolidone), poly(ethyleneglycol) (PEG), and PEG-containing copolymers.[179-181]

In the present work, gold NPs were capped with different types of ligands. Gold NSs and NRs were coated with PEG-containing molecules (section 4.4.1) and

additionally gold NSs were functionalised with CALNN based peptides (section 4.4.2).

The results obtained from the capping procedures are described in the following sections.

4.4.1 Characterization of PEGylated gold nanospheres and nanorods

PEG and PEG-copolymers are the most used polymers coat NPs to achieve increased solubility and stability, as well as to modify the NPs surface charge.[142, 182, 183] PEG-coated NPs show additional stability, improved water solubility, and the capacity of modifying the NP surface charge.[142, 178, 182, 183]

Bifunctional PEG molecules, such as SH-PEG-COOH and SH-PEG-NH_2 (Scheme 2.4), can be used to modify the NPs surface charge, as well as an anchor to attach new functional groups on the surface through conjugation chemistry.[184]

In this study, gold NSs and NRs were modified with hetero bifunctional PEG, *i.e.* a thiol-containing PEG molecules with either an amino (HS-PEG-NH_2, positively charged) or a carboxyl (HS-PEG-COOH, negatively charged) termini.

The PEGylation strategy used involved the binding of the thiol group of the PEG molecule to the gold NP surface (Scheme 4.1), due to the very high specific binding affinity of gold to thiol groups (the S-Au bond energy is 418 ± 25 kJ/mol).[185] Both PEG-containing molecules used had a molecular weight of 5000 Da, since short-chain (lower molecular weight) PEG gives improved NP surface coverage when compared with long-chain (higher molecular weight) PEG.[142]

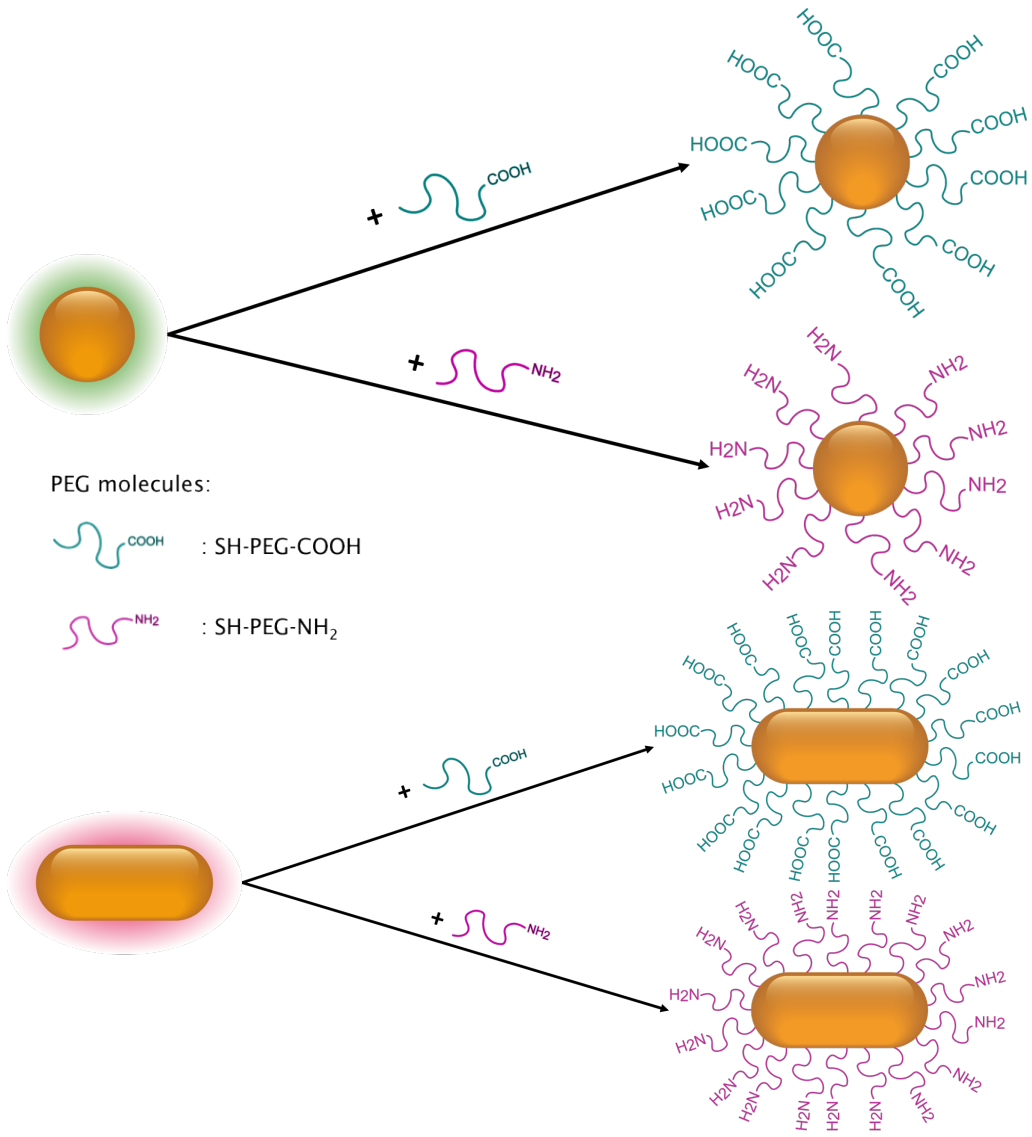

Scheme 4.1 Schematic illustration of the ligand exchange reaction between BSPP and PEG in gold NSs and between CTAB and PEG in gold NRs.

Gold NSs with a narrow size-distribution were prepared following the Turkevich method[127] and afterwards coated with BSPP. The PEGylation of the BSPP-coated gold NS was performed over 24 hours, the first 2 hours at room temperature and the following 22 hours at 4ºC. The concentration of PEG molecules used was 5 PEG/nm^2 of NP surface. Removal of unreacted PEG, was achieved by centrifugation followed by re-dispersion in water. The average size of the gold

core of the SH-PEG-COOH and SH-PEG-NH_2 -coated gold NSs obtained from TEM analysis was 14.83 ± 0.02 nm (average ± SE), and 14.71 ± 0.04 nm (average ± SE), respectively, showing that the size of the gold core remain unchanged relatively to the BSPP-coated gold NSs (14.82 ± 0.02 nm (average ± SE)).

Figure 4.4 shows a representative TEM image, size histograms and UV-Visible spectra of PEGylated gold NSs.

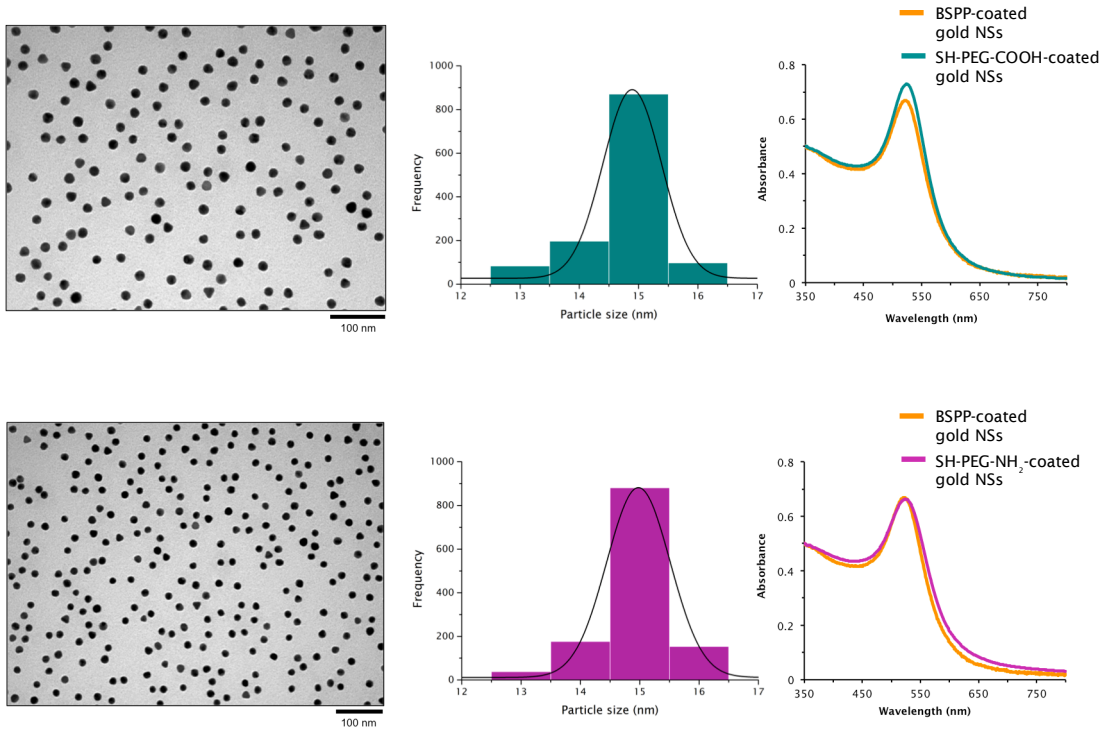

Figure 4.4 TEM images, size-distribution histograms and UV-Visible spectra SH-PEG-COOH (top row) and SH-PEG-NH_2 (bottom row) -coated gold NSs.

The redshift in the UV-Visible spectrum of PEG-SH-COOH and PEG-SH-NH_2 -coated NSs from 521 nm to 524 nm, relatively to BSPP-coated gold NSs indicates the presence of the PEG molecules in the surface of the NPs.

TEM images and size-distribution histograms demonstrate the monodispersity of the PEGylated gold NS.

Table 4.2 shows DLS and zeta potential measurements of BSPP, SH-PEG-COOH and SH-PEG-NH_2 -coated gold NSs in Milli-Q water. DLS of the PEG-coated NSs revealed an increase in hydrodynamic diameter when compared with the BSPP-coated gold NSs. This increased confirmed the PEG monolayer formation on the NS surface.

Table 4.2 Zeta potential and hydrodynamic diameter of BSPP, SH-PEG-COOH and SH-PEG-NH_2 -coated gold NS in Milli-Q water. Values presented are averages ± SE.

Gold NP type	Zeta potential (mV)	Hydrodynamic diameter (nm)
BSPP-coated gold NS	-27.43±0.81	21.05±0.08
SH-PEG-COOH-coated gold NS	-30.70±0.13	39.24±0.13
SH-PEG-NH_2-coated gold NS	23.47±0.03	42.64±0.37

Different approaches were tested to successfully PEGylate gold NRs. The same one-step protocol used to PEGylate NSs, using different amounts of PEG, was tested for gold NRs but the coating was unsuccessful. From the experimental observations, it was found that the removal of CTAB from the NRs surface and PEG attachment must happen simultaneously. The removal of CTAB prior to the PEG attachment to the NRs surface, results in NRs aggregation. This is in agreement with the recent results of Kinnear *et al.*[145] who reported that the exchange of CTAB by PEG likely occurs first, at the ends of the NRs followed by a partial exchange on the NRs longitudinal sides.

The major challenge in the replacement of CTAB by thiolated ligands is the destabilisation of the protective CTAB bilayer upon initial functionalisation, which leads to aggregation. To overcome this, the CTAB concentration in the NRs solution was reduced and the addition of thiolated PEG was done simultaneously in a two-step protocol. This allowed the concurrent desorption of CTAB and adsorption of PEG,[145] avoiding aggregation due to absence of enough CTAB coating molecules.

In detail, PEGylation of gold NR was performed in a two-step procedure over 28 hours at room temperature, using a concentration of 10 PEG/nm^2, the minimum concentration recommended to stabilise NR.[145] The fist PEGylation step was carried on over 24 hours after which the excess unreacted PEG was removed by centrifugation with the pallets re-dispersed in mixtures of PEG and water. This second PEGylation step was performed over 4 hours, after which the excess of PEG was again removed by centrifugation followed by re-dispersion in in water.

The PEGylation procedure should guarantee the complete removal of CTAB molecules from the surface of the gold NRs. However, Kinnear *et al.*[186] confirmed the presence of a small quantity of CTAB in the PEGylated gold NRs by nuclear magnetic resonance spectroscopy. This small quantity of CTAB is most likely intercalated into the PEG coating because of the well-know interactions of PEG with surfactants.[187, 188] Nevertheless, Kinnear an co-workers showed that the PEG coating avoided adverse biological effects from CTAB.[186]

Representative TEM image, size-distribution histogram and UV-Visible spectrum of the PEG-coated gold NR are shown in Figure 4.5.

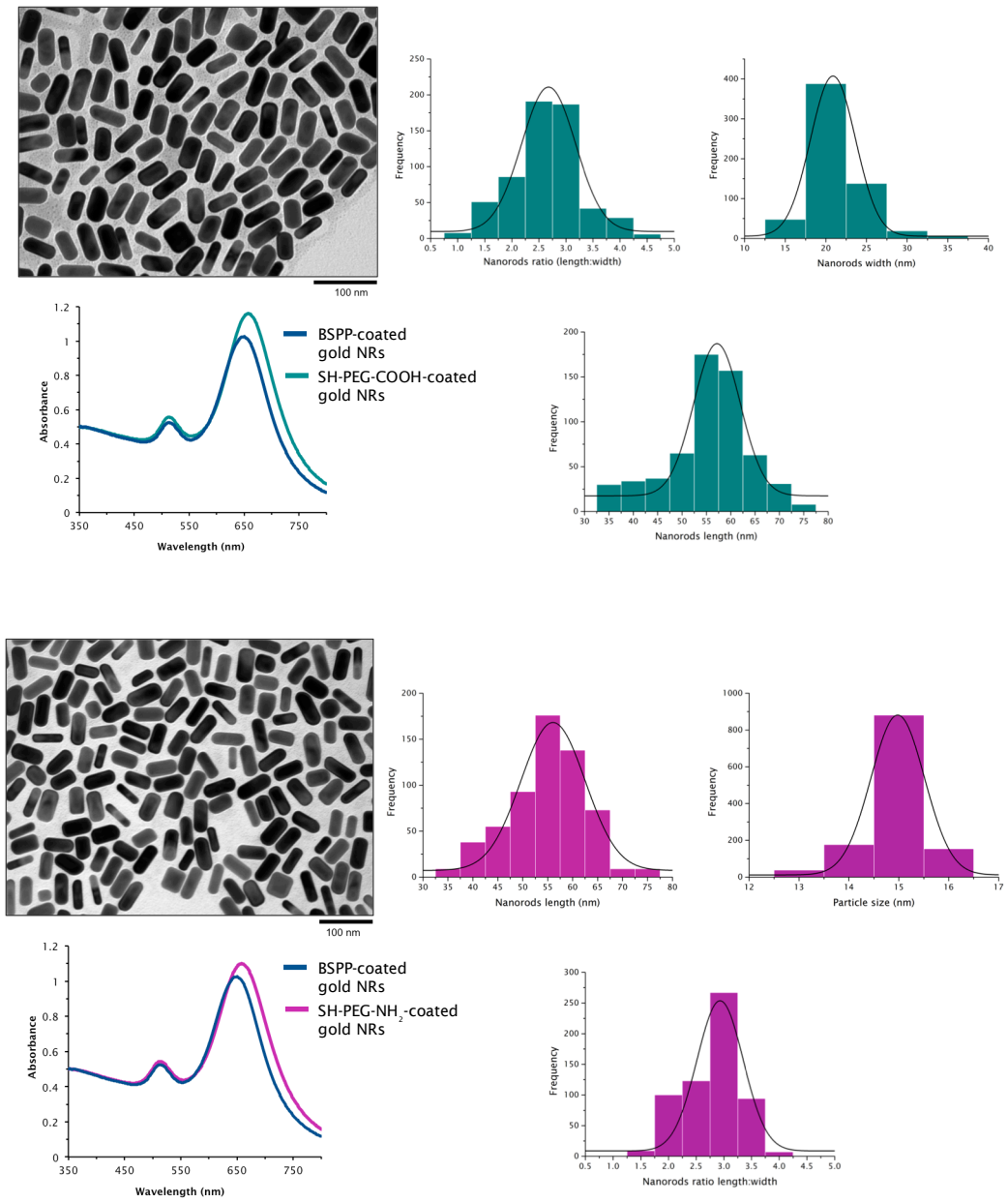

Figure 4.5 TEM images, respective size-distribution histograms and UV-Visible spectrum SH-PEG-COOH (top rows) and SH-PEG-NH_2 (bottom rows) -coated gold NRs.

The redshift of the longitudinal peak in the UV-Visible spectrum of PEG-SH-COOH and PEG-SH-NH_2 -coated NRs from 651 nm to 657 nm, relatively to

CTAB-stabilised gold NRs indicates the presence of the PEG molecules in the surface of the NPs.

The average size of the gold core of SH-PEG-COOH and SH-PEG-NH_2 –coated gold NR obtained from TEM analysis was 55.31 ± 0.36 nm (average ± SE) x 21.47 ± 0.13 nm (average ± SE) (length x width) and 54.61 ± 0.33 nm (average ± SE) x 19.81± 0.13 nm (average ± SE) (length x width), respectively, showing that the size of the gold core remain unchanged relatively to the CTAB-coated gold NRs (55.29 ± 0.36 nm (average ± SE) x 21.48 ± 0.13 nm (average ± SE) (length x width)).

TEM images and size-distribution histograms demonstrate the monodispersity of the PEGylated gold NR. Zeta potential measurements of CTAB, SH-PEG-COOH and SH-PEG-NH_2 -coated gold NRs in Milli-Q water are shown in Table 4.3.

The zeta potential of the PEG-modified NSs and NRs (Table 4.2 and Table 4.3) was measured to determine the magnitude of the electrostatic or charge repulsion or attraction between particles, and consequently their stability.

Table 4.3 Zeta potential of CTAB, SH-PEG-COOH and SH-PEG-NH_2 -coated gold NR in Milli-Q water. Values presented are averages ± SE.

Gold NP type	**Zeta potential (mV)**	**Hydrodynamic diameter (nm)**	
		Peak 1	Peak 2
CTAB-coated gold NR	9.07±1.42	85.71±0.76	9.87±0.62
SH-PEG-COOH-coated gold NR	-33.26±0.05	103.60±0.93	14.84±0.52
SH-PEG-NH_2-coated gold NR	23.57±0.10	110.13±0.85	10.66±0.46

Zeta potential measurements confirmed the stability of all the PEG-coated NP, with high zeta potential values for both SH-PEG-COOH and SH-PEG-NH_2-coated particles.

Gold NSs and gold NRs coated with SH-PEG-COOH presented a negative surface charge, while the ones coated with SH-PEG-NH_2 presented a positive surface charge. As previously mentioned, the zeta potential is a measure of the NP stability, *i.e.* NPs resistance to aggregation. The higher the NPs zeta potential is, either positive or negative, the more efficient will be the repelling force between the NPs, and consequently the more stable they will be. All the PEGylated NPs used in the study had high negative (PEG-COOH) or positive (SH-PEG-NH_2) zeta potential values, indicating their colloidal stability. NPs stability was further confirmed by the TEM images and the UV-Visible spectrum.

It has been shown that the maximum grafting density of PEG to gold NS and gold NR are 1.6 PEG/nm^{-2} and 0.052 PEG/nm^{-2}, respectively, confirming the need of a higher concentration PEG to fully functionalise the gold NRs.[189]

Although DLS is a technique routinely used for NP size analysis,[161, 190, 191] it has an inherent problem in describing the size of non-spherical particles. The diameter measured by DLS is a value that refers to how a particle diffuses within a fluid so it is referred to as a hydrodynamic diameter.[192] The diameter that is obtained by this technique is the diameter of a sphere that has the same translational diffusion coefficient as the particle.[193, 194] The particle hydrodynamic diameter depends not only on the size of the particle core, but also on any surface structure that will affect the diffusion speed, as well as the concentration and type of ions in the medium. Hence, as mentioned before, the hydrodynamic diameter of a NR is the diameter of a sphere that has the same translational diffusion speed as the particle. If the shape of a particle changes in a way that affects the diffusion speed, then the hydrodynamic size will change.

The size distribution of gold NRs obtained by DLS measurements presents two peaks (Table 4.3), a higher intensity peak at around 85 nm - 110 nm and a smaller intensity peak at around 10 nm - 14 nm. DLS measurements in Table 4.3 simply mean that CTAB, SH-PEG-COOH and SH-PEG-NH_2 -coated gold NRs have the same diffusion coefficient as gold NSs with hydrodynamic diameter of 85.71 nm, 103.60 nm and 110.13 nm, respectively. The small size peak around 10 nm -14 nm is sometimes mistaken as the presence of small particle impurities. Several reports recently proposed that this small size peak is actually a representation of the rotational diffusion of the non-spherical NPs.[190, 195] It is not an actual particle size distribution peak. It corresponds to neither the longitudinal and transverse dimension of the NRs. This peak signifies that the rotational diffusion coefficient of the NRs is equivalent to the translation diffusion coefficient of a spherical particle with an average diameter of 10 nm - 14 nm.[196]

4.4.2 Characterization of peptide-functionalised gold nanospheres

CALNN peptide was design by Levy and co-workers as a capping agent of gold NPs.[197] From the 49-peptide sequences they studied, the sequence CALNN was the one showing the best performance as capping agent. As mentioned before, CALNN contains hydrophobic end groups that ensure NP solubility in water, a thiol group that forms a stable bond with the gold surface, and a positively charged ammonium group that may also interact with gold. These properties allow CALNN to convert citrate-stabilised gold NPs into extremely stable, water-soluble gold NPs.[198-200] Recently, Levy *et al.*[201] reported a method for the synthesis of monofunctionalised gold NPs using CALNN as a binding anchor for the functional group to the NP. They prepared peptide-capped NPs by mixing 6 nm gold NPs with peptide solutions of the peptide CALNN and a

functional peptide composed of the CALNN sequence extended by a His-tag sequence and a biological label ($GHHHHHHHGK_{biotin}G$).[201]

The same approach was used here to functionalise 15 nm gold NSs with two CPPs. These CPPs were originally designed to efficiently cross the biological membranes and facilitate the cell uptake.[202, 203] Several studies in the cosmetic and pharmaceutical research fields have been focusing on the application of CPPs in the topical and transdermal delivery of compounds.[204, 205] CPPs characteristics such as relatively short length, water solubility, cationicity and amphipathic character makes them strong candidates for delivering a wide variety of biomolecules across the skin.

In the present work, the CPPs: Tat and R_7 were utilised. Tat has been successfully applied for intracellular delivery of a broad variety of cargoes, including various nanosized carriers such as liposomes, micelles, and NPs,[206] whilst R_7 has been shown to cross the skin barrier and enter the epidermis.[207]

To perform a systematic study we used three types of peptides to functionalise the NP surface: CALNN, CALNNTat, $CALNNR_7$. The attachment of CALNN, CALNNTat or $CALNNR_7$ to the gold NP surface can be easily achieved by a stable gold–thiol bond. The main challenge of conjugating gold NPs with CALNNTat and $CALNNR_7$ is the opposite charge of the peptides when compared to the gold NP surface charge.[208] CALNNTat and $CALNNR_7$ have a positive net charge (Table 4.1), while BSPP-coated gold NPs possess a negative zeta potential (Table 4.2).

Several attempts were made to achieve a full coverage of the gold NP surface with CALNNTat and $CALNNR_7$, *i.e.* replace the BSPP on the gold NS surface by 100% CALNNTat or 100% $CALNNR_7$. This resulted in unstable NPs conjugates, probably due to the binding of positively charged ligands to a negatively charged NP. This causes a charge compensation that reduces the electrostatic repulsion between the functionalised gold NP and destabilizes them.[209] Thus, one type of gold NPs was functionalised with layer homogeneous layer of CALNN peptide, while a second and third type were functionalised with a mixed layer of 99%CALNN/1%CALNNTat and 99%CALNN/1%$CALNNR_7$, respectively. In the latter, CALNN assists in the solubility and stability of the

NP, while the CALNNTat and CALNNR$_7$ provide the NPs with the desirable functionalisation.[148] The addiction of these peptides mixtures to the gold NPs did not imply that this exact ratio of peptides, *i.e.* 99%CALNN and 1%CALNNTat or 99%CALNN and1%CALNNR$_7$, was the ratio actually bound to the surface of the gold NPs. Nevertheless, NPs characterization and results from both, the study of NPs interaction with MDCK-II cells (Chapter 5) and NPs penetration through the skin (Chapter 6), confirmed the efficient attachment of CALNNTat and CALNNR$_7$ to the gold NSs surface, regardless the quantity of these peptides that were actually bound to the NSs surface. By simplicity, the peptide functionalized NSs were named CALNNTat and CALNNR$_7$ –functionalised gold NSs.

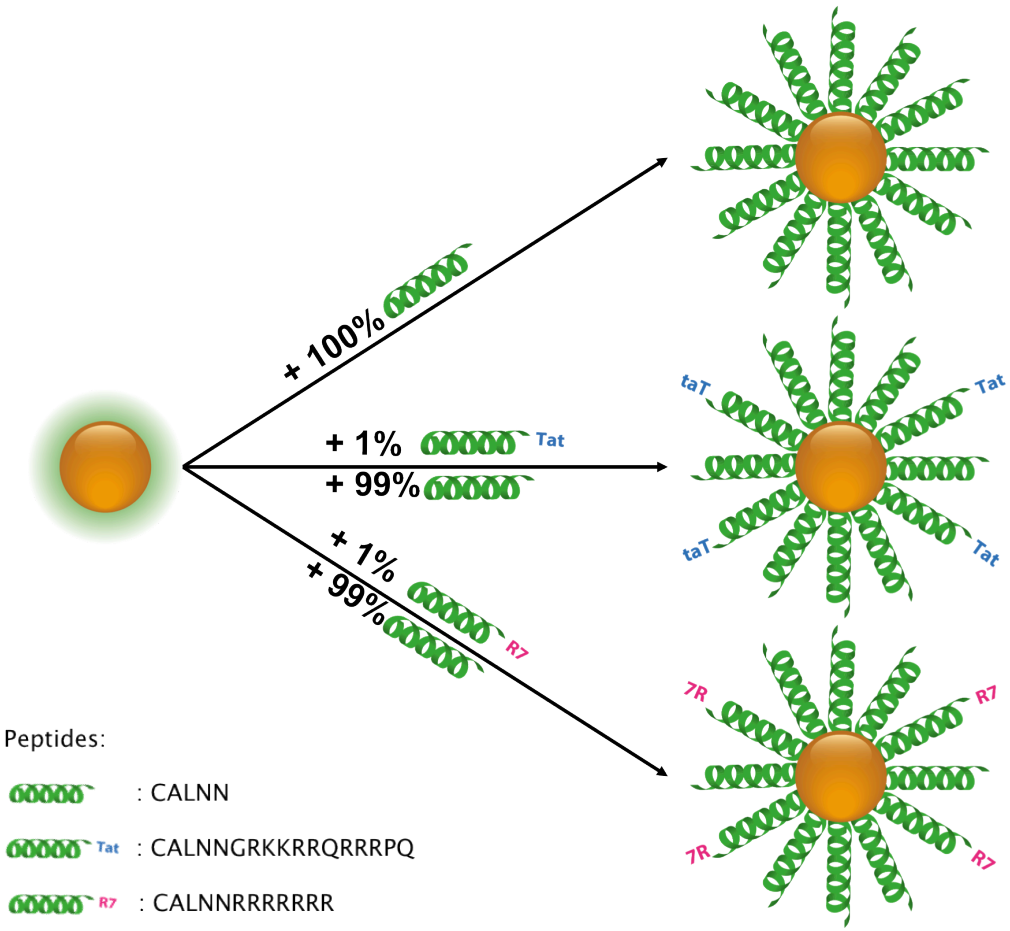

Scheme 4.2 Schematic illustration of the ligand exchange reaction between BSPP and CALNN-based peptides in gold NSs.

A schematic illustration of the peptide-functionalization procedure is shown is Scheme 4.2.

The functionalization with CALNN or CALNN-containing peptides should guarantee the complete removal of BSPP molecules from the surface of the gold NSs. Nevertheless, if some BSPP remained in the in peptide-functionalized gold NPs, it is most likely to be intercalated with the CALNN or CALNN-containing peptides and therefore not affecting the gold NP specific functionalization assigned by the peptides.

The three types of peptide-functionalised gold NSs are characterised in Figure 4.6, with TEM representative images, size-distribution histograms and UV-Visible spectra.

The average size of the gold core of the CALNN, CALNNTat and $CALNNR_7$ -functionalised NSs obtained from TEM analysis was 14.59 ± 0.03 nm (average ± SE), 14.49 ± 0.03 nm (average ± SE), and 14.53 ± 0.03 nm (average ± SE), respectively, showing that the size of the gold core remain unchanged relatively to the BSPP-coated gold NSs (14.82 ± 0.02 nm (average ± SE)).

The redshift in the UV-Visible spectrum of CALNN, CALNNTat and $CALNNR_7$ -functionalised NSs from 521 nm to 522 nm, 525 nm and 524 nm, respectively, relatively to BSPP-coated gold NSs indicates the presence of the peptides in the surface of the NPs.

TEM images and size-distribution histograms demonstrate the monodispersity of the peptide-functionalised gold NS.

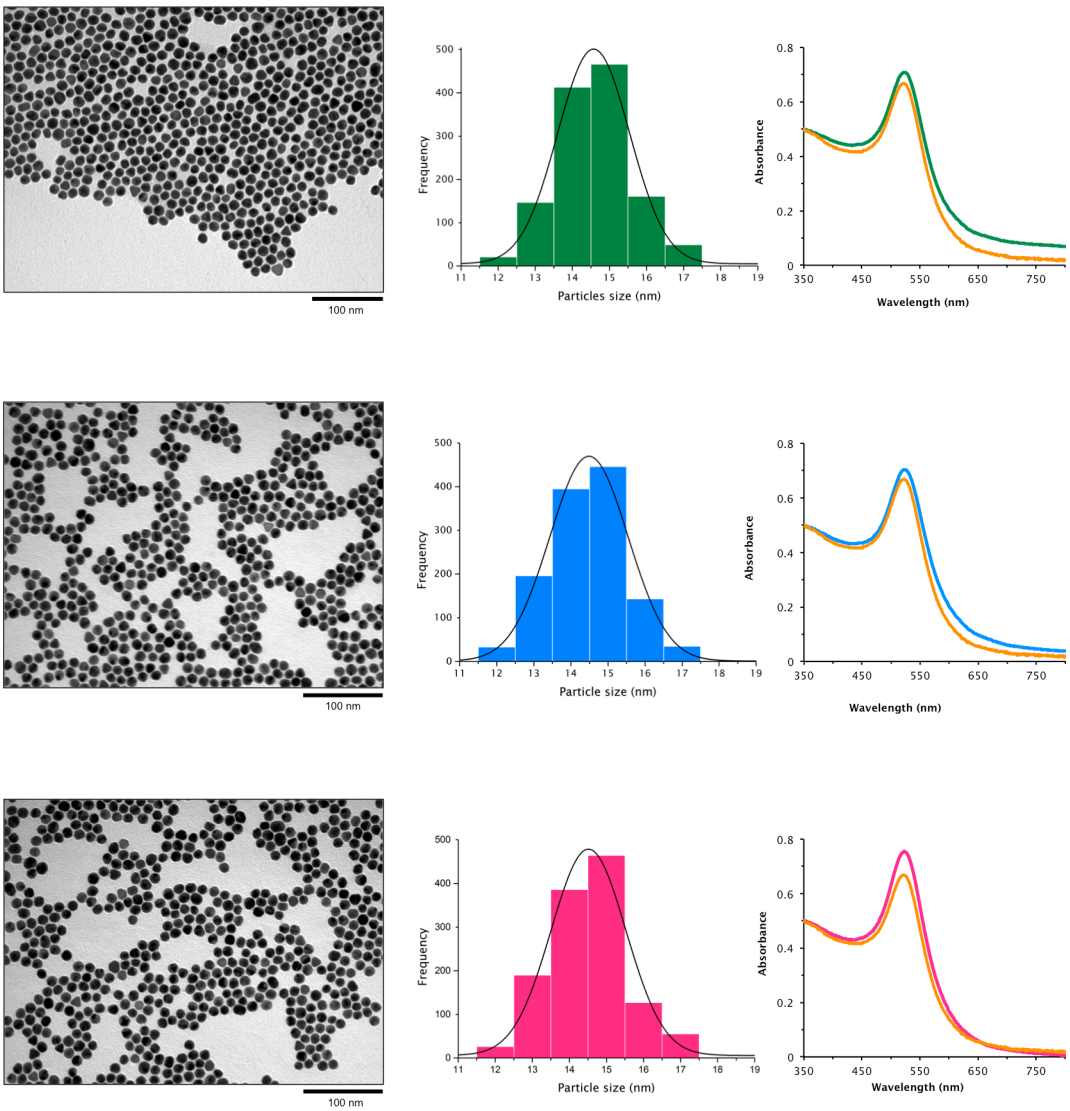

Figure 4.6 TEM images, size-distribution histograms and UV-Visible spectra of CALNN (top row), CALNNTat (middle row) and CALNNR$_7$ (bottom row) –functionalised gold NSs.

Figure 4.7 shows the gel electrophoresis of BSPP-coated and peptide-functionalised gold NPs. The delay on the band corresponding to the peptide-functionalised gold NPs, when compared with the band of the BSPP-coated gold NSs, is possibly associated with the decrease of the NSs net negative charge

and the increase of their hydrodynamic diameter, especially in the case of gold NSs functionalised with CALNNTat and $CALNNR_7$, *i.e.* longer chain peptides.

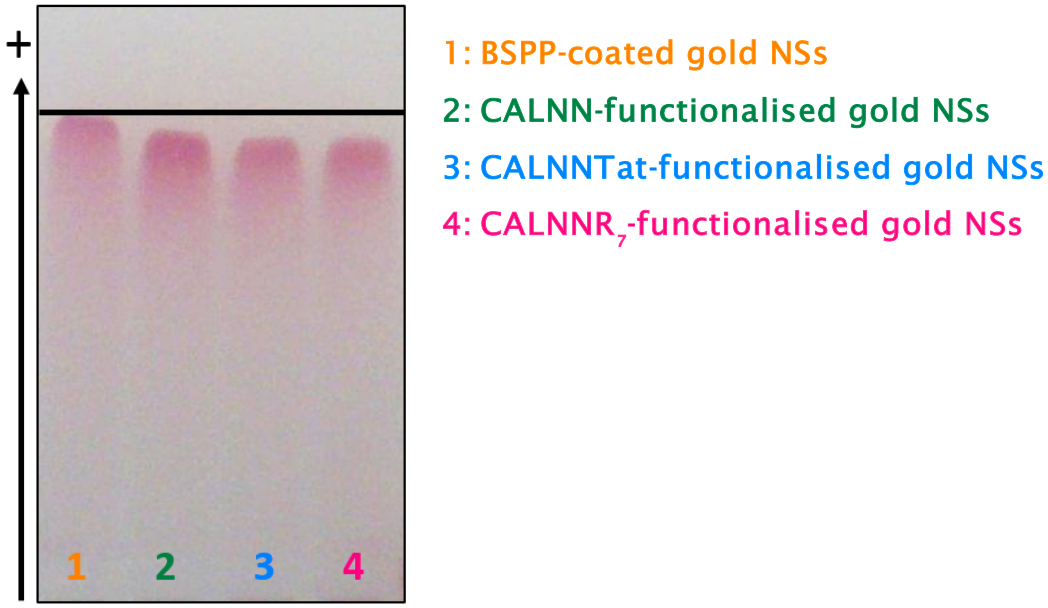

Figure 4.7 Gel electrophoresis of BSPP-coated and CALNN, CALNNTat and $CALNNR_7$ –functionalised gold NSs.

4.5 Summary

Protocols to PEGylated gold NS and gold NR were established. The exchange of BSPP with PEG in the gold NSs surface or CTAB with PEG gold NRs surface, was successfully performed. PEGylated NPs were fully characterised to confirm their stability.

Furthermore, gold NSs were functionalised with CALNN-containing peptides. TEM and spectroscopic analysis demonstrated the colloidal stability of the colloidal solutions. The delay on the gel electrophoresis of the gold NPs coated

with CALNNTat and CALNNR$_7$ relatively to the CALNN-functionalised gold NPs indicated the presence of the CPP in the surface of the NPs.

Table 4.4 shows a schematic illustration of all different types of NPs used in this thesis to investigate the effect of NP shape, charge and functionalisation in their interaction with MDCLK-II cells and in their penetration through human and mouse skin.

Table 4.4 Schematic illustration of the gold NPs used in this study.

		Charge		Function		
		SH-PEG-COOH coated gold NP	SH-PEG-NH_2 coated gold NP	CALNN functionalised gold NP	CALNNTat functionalised gold NP	$CALNNR_7$ functionalised gold NP
shape	spheres	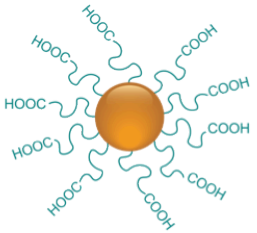	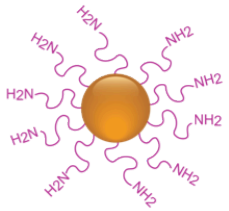	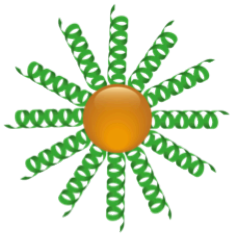	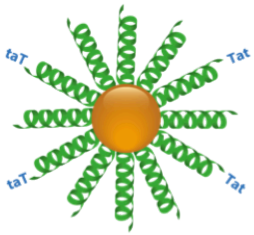	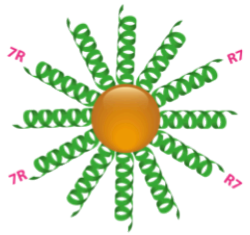
	rods	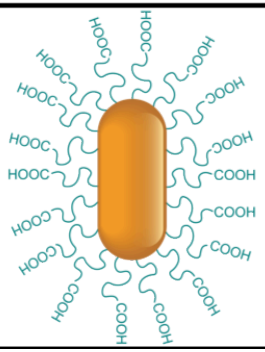	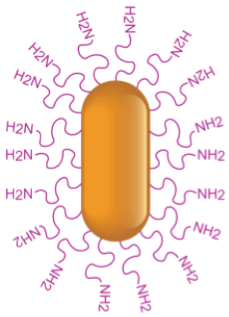			

PEG molecules:

: SH-PEG-COOH

: SH-PEG-NH_2

Peptides:

: CALNN

: CALNNGRKKRRQRRRPQ

: CALNNRRRRRRR

Chapter 5 Interaction of gold nanoparticles with MDCK-II cells

The MDCK-II, a canine renal epithelial cell line, and Caco-2, a human colon adenocarcinoma cell line, have been extensively used as *in vitro* tools to assess a drug permeability and transporter interactions during discovery and development.[210, 211] When cultured on porous membrane, these cells form confluent monolayers that model the epithelial barrier for permeability, transport and drug-interaction assays.[212-215] When compared to Caco-2 cells, MDCK-II cells have lower TEER and, since the MDCK-II cells are from dog kidney, the profile of expressed transporter enzymes with respect to human derived Caco-2 cells may be different.[211] Nevertheless, a good correlation between Caco-2 and MDCK-II permeability experiments is usually observed.[216]

MDCK-II cell cultures present some advantages when compared with Caco-2 cells. The main advantage is their shorter culture time to confluence: while MDCK-II cells differentiate into columnar epithelium and form tight junctions in about 7 days, Caco-2 cells require approximately 21 days.[217] For this reason, MDCK-II cells were used in this work.

The MDCK-II cell line is a well-established model for biological processes, such as absorption and penetration across the tight junction containing epithelia.[218, 219] MDCK-II cells in culture produce a polarized confluent monolayer, form tight junctions and microvilli on the apical cell surface.[25, 220]

5. Interaction of gold nanoparticles with MDCK-II cells

There are a number of different methods to analyse the tight junctions structure and function *in vitro*.[221] Studies on the tight junction assembly and function are generally performed by measuring the TEER of the cell monolayers, whereas the investigation of the tight junction morphology involves a structural analysis by LM and TEM. The latter can also provide information concerning cell viability. Moreover, the location and expression of tight junction proteins often involve techniques, such as immunofluorescence,[222] immunocytochemistry[223] and western blotting.[224] Since the purpose of present research was to investigate the tight junction assembly, function and morphology, the location and expression of tight junction proteins was not accessed.

Seven different types of gold NPs (Table 4.4) were employed to study their interaction with MDCK-II cells. These particles differ between each other in terms of charge, shape and surface functionalisation. Shortly, 15 nm gold NSs and 55 x 20 nm (length x width) gold NRs coated with thiol-containing PEGs with either a amino (positively charged particles) or a carboxyl (negatively charged particles) termini and gold NSs functionalised with CALNN, CALNNTat, and $CALNNR_7$.

The effect of the presence of gold NPs during the tight junction formation and maintenance were investigated. Results from this study are presented in the current chapter. Section 5.1 comprises the study of how the size, shape, charge and functionalisation of gold NPs influence the formation of tight junctions. This was achieved by performing TEER measurements. Section 5.2 contains the results from study of the interaction of the same NPs with the fully-formed tight junctions. TEER measurements, LM and TEM analysis were preformed to investigate the gold NPs-tight junctions interactions.

5.1 Effect of the presence of gold nanoparticles on the tight junction formation

Tight junctions have important roles such as the regulation of the epidermal barrier permeability, by regulating the paracellular flux of water-soluble molecules between adjacent cells,[18] and are crucial for maintaining the epithelial cells polarity. As mentioned in Section 2.2.2, tight junctions are composed by several proteins including actin-binding proteins and adhesive transmembrane proteins. Among the latter are claudins that are critical barrier proteins.[17] Mutations in the genes of these proteins can compromise the tight function and structure.[225] Similarly, certain environmental conditions, such as UV exposure, can cause a temporary disruption of the tight junction's protein complex, resulting in a loss of the barrier function.[226]

In the present work, MDCK-II cells were cultured with seven types of NPs (Table 4.4), to investigate if the NPs presence affects tight junction formation between adjacent cells. The gold NPs used were different in terms of charge, shape and surface functionalisation, in order to investigate if these parameters perturb or not the tight junction formation.

5.1.1 Transepithelial electrical resistance measurements – effect of gold nanoparticles in the tight junction formation

The effect of the present of gold NP in the tight junction formation in MDCK-II cell monolayers was evaluated by measuring the TEER. As mentioned in Chapter 2, TEER is a technique used as a quantitative measure of the tight junction physiology.[227] The electrical resistance was measured by means of an EVOM^2 epithelial voltammeter, which is a device specifically designed to perform non-destructive TEER measurements.[228] Essentially, an alternating current voltage is applied to two electrodes, one on each side of the cell layer. The resulting current is measured and used to obtain the electrical resistance according to Ohm's law.[22]

TEER is characteristic of each cell monolayer. The disruption of tight junctions by NPs can be monitored by quantitatively measuring the TEER of monolayer.[229] If NPs disrupt the integrity of the epithelial monolayer by loosening tight junctions, the TEER will be reduced. The magnitude of TEER reduction would then reflect the amount of damage to the monolayers. TEER values can also give an indication of the toxic effects induced by NPs, since damage to the tight junctions would allow the leakage of potentially toxic substances through the epithelial barriers into circulation.

In our experiments, MDCK-II cells were seeded (5×10^5 cells/ml) onto 12-well transwell insert membrane supports together with the NPs. The concentration of NSs and NRs added to the cells was 1×10^7 NSs/cell and the 1×10^6 NRs/cell, respectively. The electrical resistance between the apical and basolateral surfaces of the cell monolayer was monitored over 10 days. Results are shown in Figure 5.1.

The steep increase in TEER observed as early as 24 hours after cell seeding marks the early onset of tight junction formation in the cell monolayer. After 8 days, TEER reached a peak, indicating fully established tight junctions.[230] The TEER then decreased. It has been suggested that this TEER decrease may occur due to an increasing number of cells and an increasing total perimeter of cell-cell contacts per surface area.[230] Finally, after 9 days, the TEER values reached a steady plateau, between approximately 125 and 150 $\Omega.cm^2$, which are the characteristic TEER values of the MDCK-II cell line.[231]

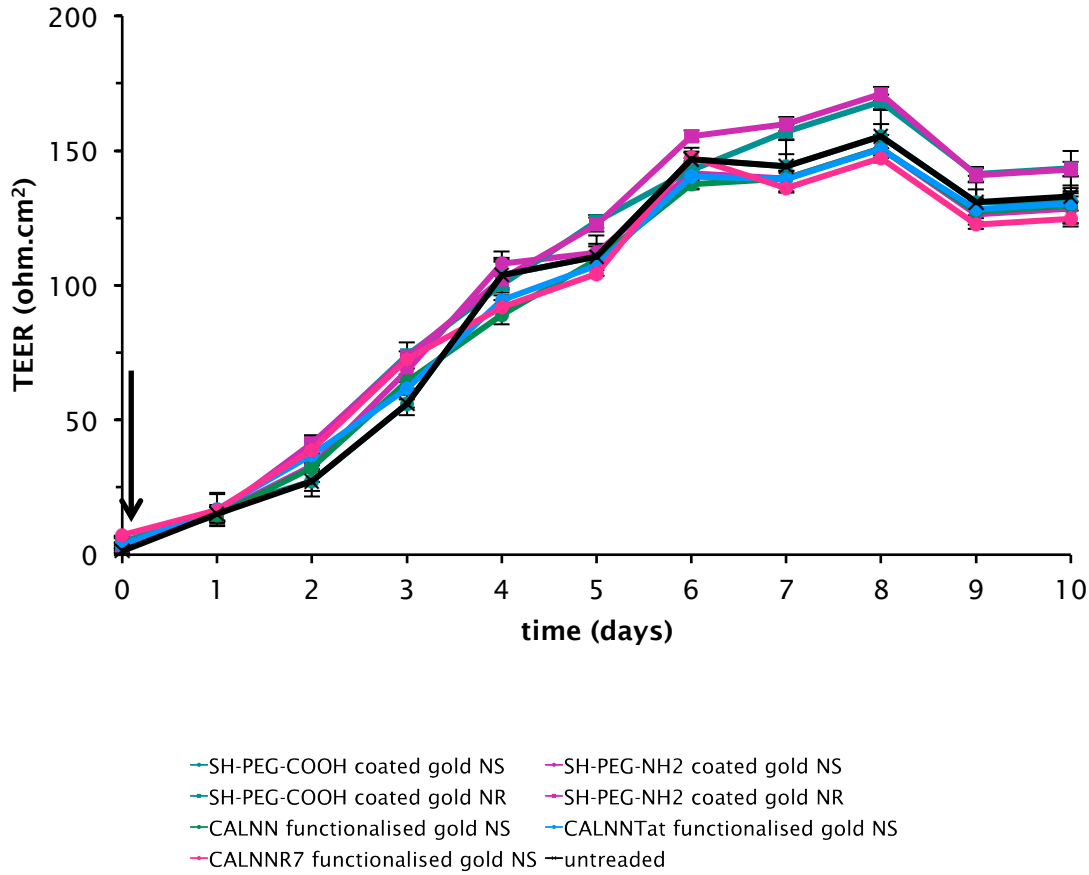

Figure 5.1 TEER of MDCK-II cell monolayers measured at 24-hour time intervals over 10 days. Gold NPs were added at day 0 (black arrow). Data points represent averages ± SE, n = 3 readings across each insert.

The TEER values presented here are the resistances obtained for each transwell insert containing cells incubated either with or without NPs, subtracted by the blank resistance, *i.e.* the resistance obtained for a transwell insert without cells or NPs and cultured under the same experimental conditions.

TEER measurements show that the presence of gold NPs did not cause any alteration in the TEER values of the cell monolayers, when compared with the untreated samples. The TEER curve was consistent for all the NPs treated and untreated samples, indicating that the process of the tight junction formation in MDCK-II cells is not affected by presence of the gold NPs, regardless their charge, shape or surface functionalisation.

5.2 Effect of the presence of gold nanoparticles on the MDCK cells monolayer

In another set of experiments, the same types gold NPs were used to investigate the influence of the presence NPs in well-formed tight junctions and their interaction with MDCK-II cells at the electron microscopy level. Because MDCK-II monolayers are considered a reliable model to simulate a skin penetration system *in vitro*, results from the present investigation can lead to a better understanding of how the gold NP charge, shape and surface functionalization may influence the NP transport through the epithermal layers of the skin.[220]

5.2.1 Transepithelial electrical resistance measurements – effect of gold nanoparticles in the tight junction maintenance

The interaction between gold NP and tight junctions in MDCK-II cells was evaluated by measuring the TEER of the cell monolayers. MDCK-II cells were seeded (5 x 10^5 cells/ml) onto 12-well transwell insert membranes and the electrical resistance between the apical and basolateral chambers of the transwell was monitored over 9 days. Results are shown in Figure 5.2.

Similarly to the experiment reported in section 5.1.1, the TEER values reached a peak after 8 days of cell incubation, followed by the typical small decrease of the TEER, values at the 9th day. At this point the tight junctions were formed and gold NPs were added to the MDCK-II cells.[230] TEER was further monitored for 24 hours. As expected, TEER values reached a steady plateau between approximately 125 and 150 $\Omega.cm^2$, showing that the presence of gold NPs did not cause any change in the typical TEER curve of the MDCK-II cell monolayer.

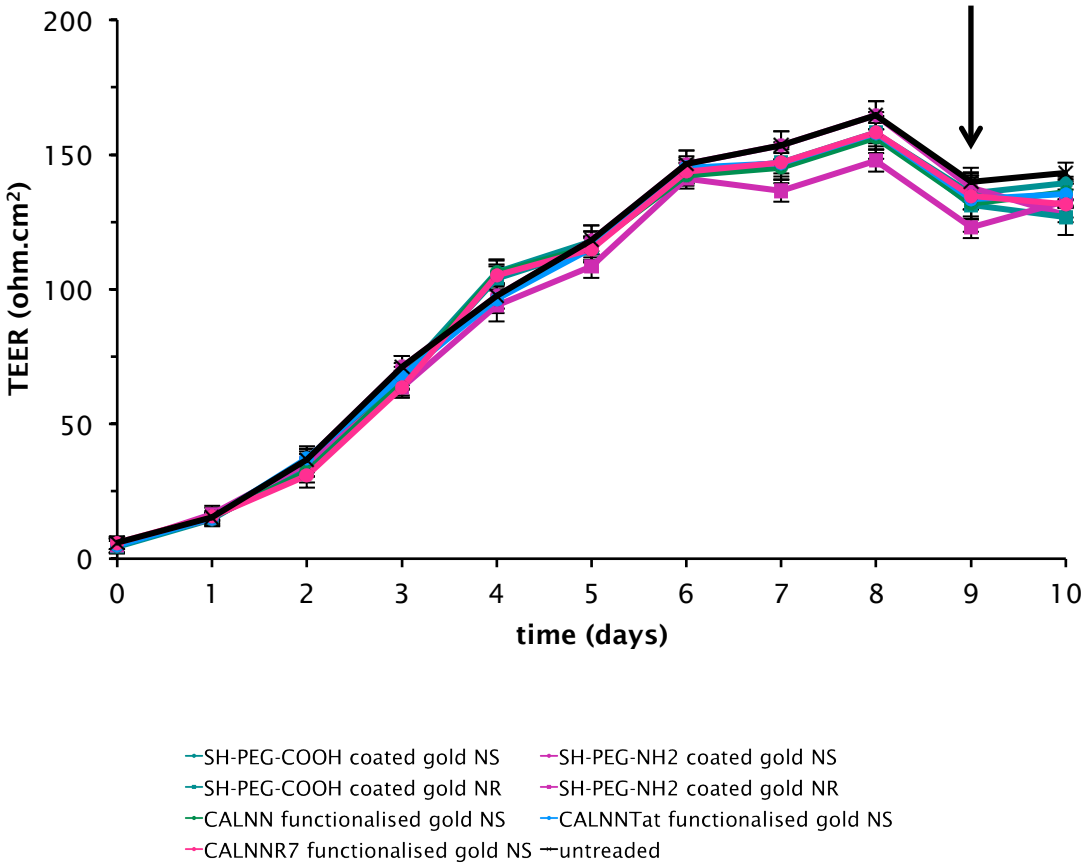

Figure 5.2 TEER of MDCK-II cell monolayers measured at 24-hour time intervals over 10 days. Gold NPs were added in the 9th day (black arrow). Data points represent averages ± SE, n = 3 readings across each insert.

It is widely reported that tight junction disruption is characterized by a significant decrease in TEER values.[224, 230, 232] According to the TEER results obtained, it is clear that tight junction disruption did not occur. These results showed the characteristic resistance of the tight junctions is not affected by the presence of gold NPs, regardless their charge, shape or function.

5.2.2 Light microscopy of tight junctions in the presence of gold nanoparticles

The interaction of gold NPs with MDCK-II cells was investigated by LM. Results are presented in Figure 5.3.

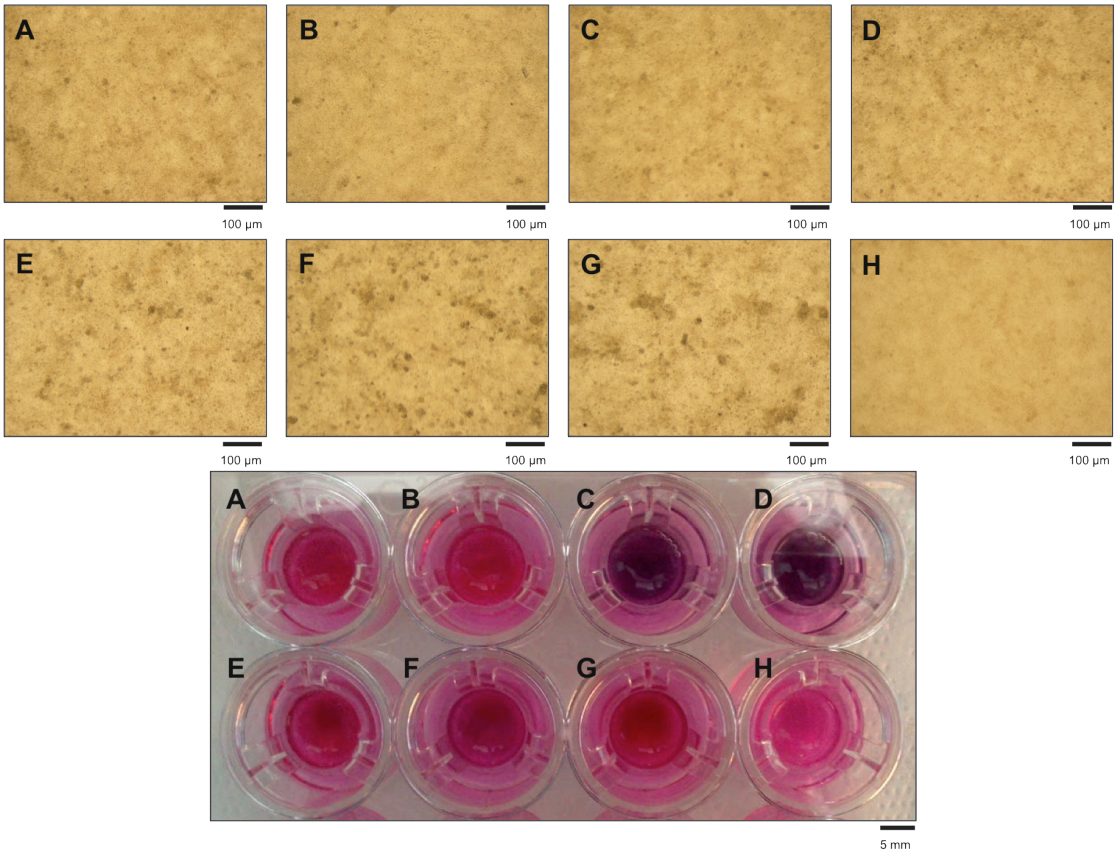

Figure 5.3 LM images (top) and digital photograph (bottom) of the MDCK-II cells monolayers (with formed tight junctions) after 24 hours incubation with: SH-PEG-COOH coated gold NSs (A); SH-PEG-NH_2 coated gold NSs (B); SH-PEG-COOH coated gold NRs (C); SH-PEG-NH_2 coated gold NRs (D); CALNN functionalised gold NSs (E); CALNNTat functionalised gold NSs (F) and $CALNNR_7$ functionalised gold NSs (G). Untreated MDCK-II cells monolayer (H).

LM pictures showed that MDCK-II cells incubated with all the seven different types of NP (Figure 5.3, top, Images A-G) present dark-coloured spots. These

spots were not observed in the untreated sample (Figure 5.3, top, Image H). Additionally, cells incubated with gold NSs functionalised with CALNN, CALNNTat and $CALNNR_7$ exhibited a significantly higher number of dark spots in the LM images (Figure 5.3, top, Images E, F and G). These spots might indicate the presence of gold NPs aggregates either on the surface of the cells or inside the cells, possibly in vesicles after being taken up.

It is worth noticing the aesthetical difference between the treated and untreated samples when observed at naked eye (Figure 5.3, bottom), where the cells incubated with NPs exhibited a dark pink colour, in the case of incubation gold NSs (Figure 5.3, bottom, Images A, B, E, F and G), or purple, in the case of incubation with gold NRs (Figure 5.3, bottom, images C and D); while the untreated cells showed, as expected, the typical pink colour of the growth media (Figure 5.3, bottom, Image H). The purple colour of the transwells with cells incubated with NRs might be the result of mixture of the pink coloured media and the blue colloidal NR solution.

5.2.3 Transmission electron microscopy of tight junctions in the presence of gold nanoparticles

To confirm that the presence of of NPs does not have an effect in the tight junction physiological structure and to have a better understanding of the gold NPs - MDCK-II cells interaction, the samples of MDCK-II cells incubated with gold NPs for 24 hours were examined by TEM. Images are shown in Figure 5.4

From the TEM images it is possible to conclude that gold NSs were taken up by MDCK-II cells to a higher extent than gold NRs of the same charge. Yang *et al.*[233] have showed that the capacity of a NP to cross a lipid bilayer depends on the contact area between the particle and the lipid bilayer, and on the orientation of the particles at the membrane, *i.e.* the local curvature of the particle at the contact point, which both are shape dependent. Additionally, cell culture studies on the effect of the NP shape in the uptake of NPs have shown that spherical NPs are taken up in greater number than rod-shaped particles of similar size and charge by mammalian cells.[234] The effect of NPs shape on their internalization, with spherical particles being taken up in higher

number than rod-shaped particles of similar size and charge, might be explained by the greater membrane wrapping time required for the elongated particles. Also, it has been hypothesised that any interactions that do occur between rod-shaped NPs and cell surfaces are easily disrupted under strong hydrodynamic shear minimizing the opportunity for cell uptake. In contrast, spherical NPs are less influenced by shear and are able to interact more strongly with the cell surface, increasing their cellular uptake.[235] From the analysis of TEM images, it appears that the shape, but not the charge, determines the level of uptake of gold NPs.

Additionally, TEM investigation showed that gold NPs functionalised with CALNN, CALNNTat and $CALNNR_7$ have a higher uptake by MDCK-II cells than the other types of gold NPs. The CALNN, CALNNTat and $CALNNR_7$ – functionalised gold NPs were mainly found in the cell cytoplasm, enclosed in vesicles (Figure 5.4, Image E, F and G). This might suggest that the uptake mechanism was endocytosis, which is in agreement with previous studies.[114]

PEGylated gold NRs were found outside the cells, nearby the microvilli (Figure 5.4, Images C and D); while single PEGylated gold NSs were found enclosed in vesicles (Figure 5.4, Images A and B).

Furthermore, TEM analysis showed that, regardless NP shape, charge and functionalization, MDCK-II physiological structure was preserved after 24 hours of incubation with gold NPs. This might be an indicative of the non-toxicity of gold NPs to MDCK-II cells, under the experimental conditions used in this thesis.

Due to limited access to ICP-AES analysis, samples were no characterized by this technique.

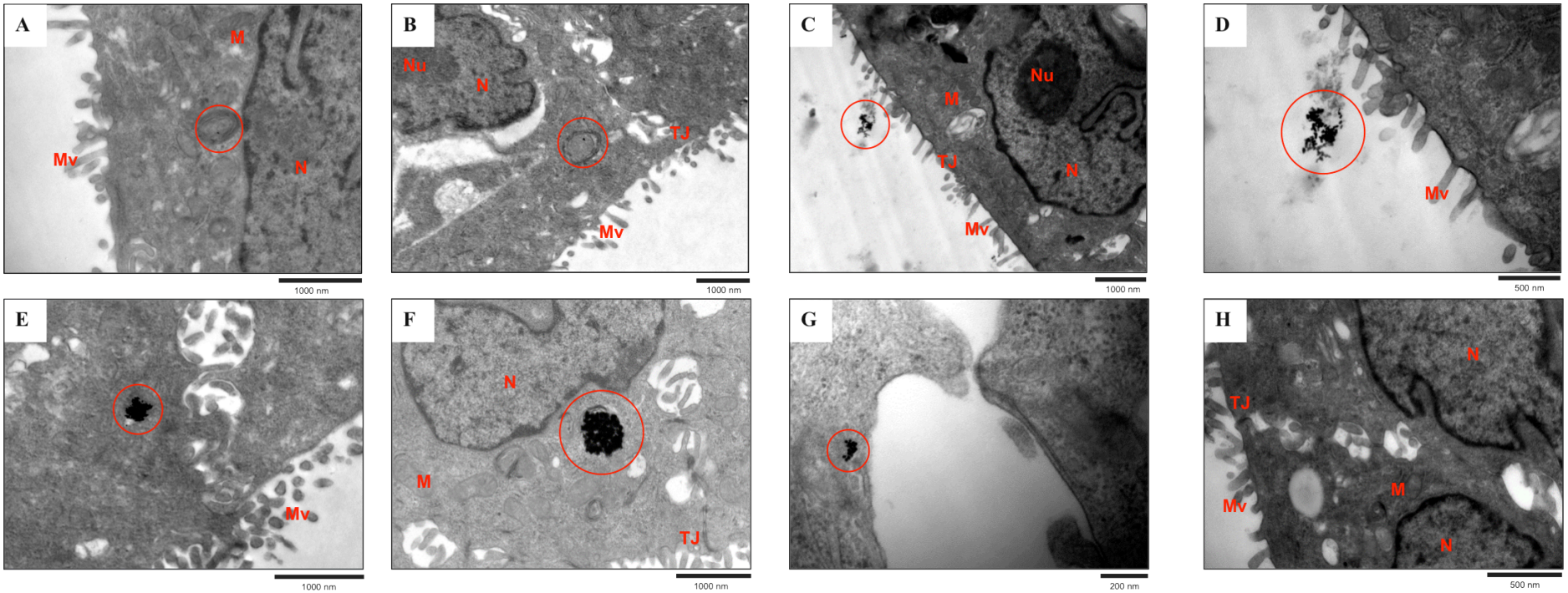

Figure 5.4 Representative TEM images of the MDCK-II cells monolayers (with formed tight junctions) after 24 hours incubation with: SH-PEG-COOH-coated gold NSs (A); SH-PEG-NH_2-coated gold NSs (B); SH-PEG-COOH-coated gold NRs (C); SH-PEG-NH_2-coated gold NRs (D); CALNN-functionalised gold NSs (E); CALNNTat-functionalised gold NSs (F) and $CALNNR_7$-functionalised gold NSs (G). Untreated MDCK-II cells monolayer (I). Red circles indicate the presence of NPs. Microvilli (Mv), Tight junctions (TJ), Nucleus (N), Nucleolus (Nu), Mitochondria (M).

5.3 Discussion and conclusions

Results from the TEER measurements showed that the exposure of MDCK-II cells monolayers, either before or after the tight junction formation, to gold NPs did not cause any change on TEER values, when compared with TEER values of untreated MDCK-II cells. The same result was observed for all the seven different types of NPs, indicating that the process of the tight junction formation and its maintenance is not affected by presence of the gold NPs, regardless the their shape, charge and functionalization.

TEM images showed that gold NSs were taken up by MDCK-II cells to a higher extent than gold NRs of the same charge. PEGylated gold NRs were found outside the cells, nearby the microvilli; while single PEGylated gold NSs were found enclosed in vesicles. Additionally, TEM investigation showed that gold NPs functionalised with CALNN, CALNNTat and $CALNNR_7$ were taken up in higher number by MDCK-II cells than the other types of gold NPs. CALNN, CALNNTat and $CALNNR_7$ –functionalised gold NPs were mainly found in large groups enclosed in vesicles in the cell cytoplasm, suggesting that the uptake mechanism was endocytosis.

LM pictures showed that MDCK-II cells incubated with all the seven different types of NP present dark-coloured spots, that were not observed in the untreated sample. Additionally, cells incubated with gold NSs functionalised with CALNN, CALNNTat and $CALNNR_7$ exhibited a significantly higher number of dark spots in the LM images. These spots might indicate the presence of gold NPs aggregates either on the surface of the cells or inside the cells, possibly in vesicles after being taken up.

Furthermore, TEM analysis showed that, regardless NP shape, charge and functionalization, MDCK-II physiological structure was preserved after 24 hours incubation with gold NPs. This might be an indicative of the non-toxicity of gold NPs to MDCK-II cells, under the experimental conditions used in this thesis.

Chapter 6 Penetration of gold nanoparticles through human and mouse skin

6.1 Introduction

In the present chapter, the penetration of colloidal gold NPs of different physicochemical characteristics through the skin is investigated. Gold NPs of different charge, shape and surface functionalisation where used to assess the influence of these parameters in the penetration through the skin. The penetration was evaluated both qualitatively and quantitatively, using a variety of complementary techniques. ICP-AES was used to quantify the total number of particles penetrating into the skin structure. TEM and PL microscopy analysis of skin cross sections provided a direct visualization of NP migration within the different skin layers. Finally, EDX was used to confirm the elemental composition of the NPs found in the skin samples.

Seven different types of gold NPs were employed to study their penetration through skin (Table 4.4). These particles differ between each other in terms of charge, shape and surface functionalisation. Shortly, 15 nm gold NSs and 55 x 20 nm (length x width) gold NRs coated with thiol-containing PEGs with either a amino (positively charged particles) or a carboxyl (negatively charged

particles) termini and gold NSs functionalised with CALNN, CALNNTat, and $CALNNR_7$.

6.2 Evaluation of skin Integrity

In penetration experiments, the choice of the skin specimens is very important, as the penetration degree can vary from specimen to specimen. Although the main skin structure is universal in mammals, there are variations according to the animal species, sex, age, and the area of the body from where the skin is obtained.[236] For example, in man the epidermis upon the eyelid is the thinnest skin in the body (0.05 mm), while the palm and sole of the foot is the thickest (1.5 mm). In general, human epidermis is thicker than mouse epidermis. On the other hand, mouse skin has more closely spaced hair follicles than human skin.[237] Furthermore, mouse skin does not have rete ridges as are seen in human skin, where the lower aspect of the epidermis forms ridges of cells that extent into the dermis.[238] All these factors must be taken into account when conclusions are drawn and they also determine the design of the experiment, as it will be discussed later. To reduce the variation caused by the factors mentioned above, healthy abdominal human skin from middle-aged donors, which has a low density of hair follicles, and dorsal mouse skin from newborn mice, where the hair follicles are in the early phases of their development, were used in the present study. The basic structure of mouse skin, consisting of stratified layers and hair follicles, is formed before birth.[239] However, a newborn mouse skin has a thick epidermis with incomplete development of hair follicles.[240] By week one the hair follicles are fully developed in anagen, the active growth phase of the hair follicles, producing hair fibres that emerge at 5 days postpartum. At this point, the truncal epidermis is relatively thick and thins and remains thin for life under normal circumstances by 2-3 weeks of age. Hair follicles produce fibers over the thorax until around 14 days of age at which time the follicles enter the catagen phase and begin to regress, undergoing apoptosis. Within 3-5 days the follicles are in the telogen phase, the resting phase of the hair foliculle. The mouse skin used in this work was

excised skin from 1 day-old mouse, with an incomplete development of hair follicles and with no hair fibres emerging at the surface yet.

It is worth noting that the ethics agreement for human samples requires that the samples are completely anonymous. Therefore, there was no access to information regarding the age and health of the donor and also the skin site. However, it is likely that the samples were abdominal skin, as most were from abdominoplasty operations. Furthermore, individuals subjected to an abdominoplasty operation are usually adults and reasonably healthy, otherwise the operation would not be undertaken. Thus, it is reasonable to assume that human samples were healthy abdominal human skin from middle-aged donors.

Another parameter that plays a critical role on the penetration studies and is not always taken into account is the skin integrity in the course of the experiments. For meaningful results the skin must maintain its integrity during penetration experiments. Franz diffusion cells (Figure 2.11) are the most commonly used setup in skin penetration experiments. However, in this setup the skin is exposed to high pressure and shear stresses developed from clamping the receptor and donor compartments together, these can affect the penetration and result in artefacts. To avoid this, different penetration setups were designed and tested, for both human and mouse skin.

LM is routinely used to assess the skin integrity. However, it only provides a gross observation of any adverse effect occurring in the skin.[241] For a more specific and detailed evaluation of the skin integrity, TEM may also be performed.[241, 242] therefore, in this present work, LM and TEM were used to assess the skin integrity over certain exposure times.

In the experiments, full thickness human skin was cultured in 6-well microplates placed at the air-liquid interface at 37˚C in 5% CO_2/air (Figure 3.2).

LM was used to assess human skin integrity at 12, 24 and 48 hours (Figure 6.1). Histological examination of the skin showed no obvious changes in the integrity of the dermis and epidermis at 12 and 24 hours incubation, however the dermis showed some local degradation of the collagen matrix after 48 hours (Figure 6.1, red asterisk).

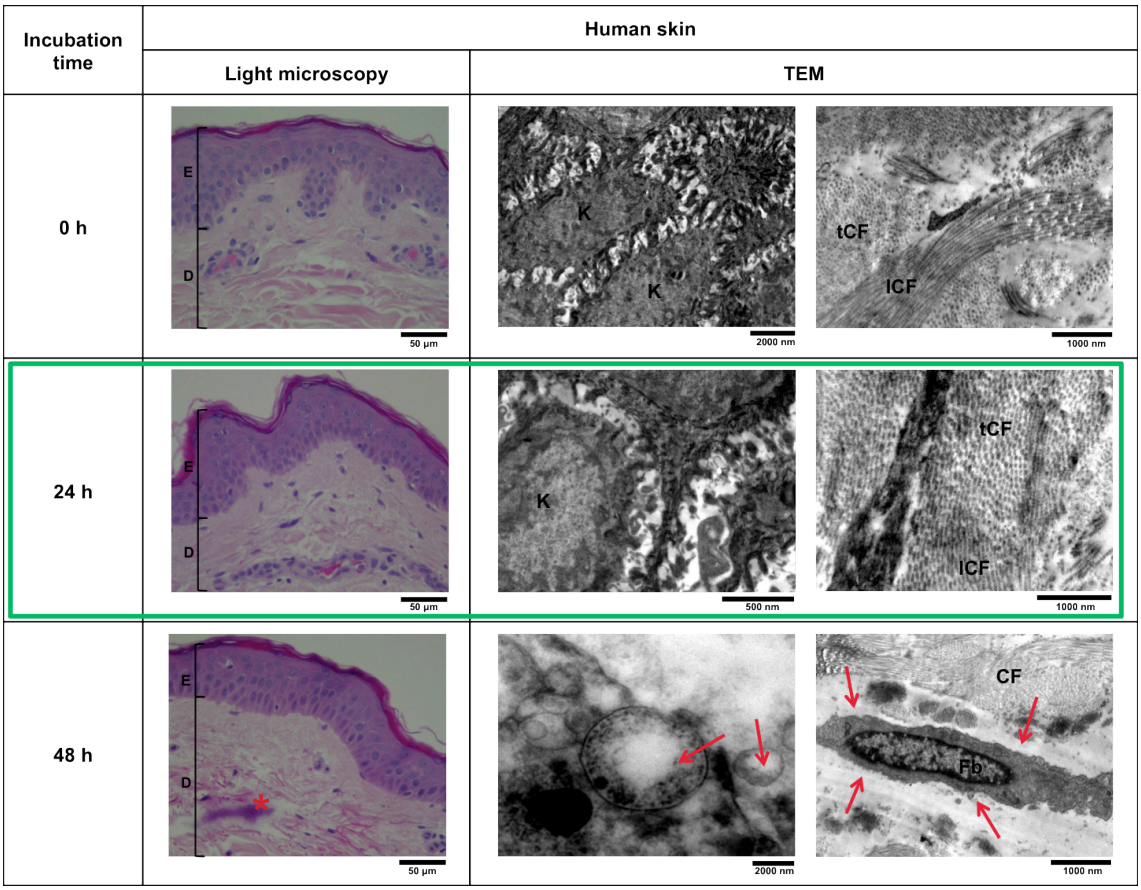

Figure 6.1 Evaluation of human skin integrity when exposed to different incubation times by LM and TEM. Red asterisk and red arrows indicate degraded areas in the skin. The green rectangle highlights the conditions chosen for the human penetration experiment. K: keratinocyte; Fb: fibroblast; CF: collagen fibres; lCF: longitudinal collagen fibres; tCF: transversal collagen fibres.

To validate the results obtained by LM, human skin samples were analysed by TEM. Results of the TEM investigation are also shown in Figure 6.1. As expected, the skin control samples (0 hours of incubation) are structurally comparable with healthy skin, either by LM (Figure 2.4, Image A) or TEM (Figure 2.5, Image I and II). The TEM images confirmed the preservation of the skin integrity over the first 24 hours incubation, while by 48 hours of incubation the skin cells showed clear cytoplasm degradation and degradation of the plasma membranes in many cells (Figure 6.1, red arrows). Therefore, 24

hours was the incubation time used in the human skin penetration experiments.

For mouse skin, the same setup and conditions as the ones used for human skin were tested (Figure 3.2) for 24 hours. LM and TEM images are shown in Figure 6.2. The histological study did not show any alteration of the skin integrity after 24 hours, however by TEM images showed loss of organelles, cytoplasmic degradation and break down of cell and nuclear membranes (Figure 6.2, 2nd row, red arrows). The more rapid loss of the integrity of the mouse skin might be attributable to the difference of skin thickness of the skin specimens used. Human skin is thick enough to be cultured in the conditions illustrated in Figure 3.2, assuring that the skin deeper layers are immersed in medium, while the epidermis remains dry. Mouse skin, however, is much thinner than human skin and it is impossible, in such experimental conditions, to maintain the epidermis dry whereas the deeper layers of the skin are immersed in medium. If the epidermis is saturated for long periods, the metabolically inactive corneocytes will absorb water and swell, whilst the deeper metabolizing keratinocytes in the epidermis do not. This results in an expansion of the corneocyte layer that starts to wrinkle. Over the long term this will compromise the skin integrity, lead to cell death and consequently to unreliable results.

Thus, for the mouse skin penetration experiments, a different setup was designed and tested. Here the mouse skin was cultured in 12-well transwell inserts at the air-liquid interface at 37°C in 5% CO_2/air as illustrated in Figure 3.3. A similar setup was reported before to investigate the penetration of gold NPs through open-edge nonsealed skin equivalents.[31] In this study, the skin equivalents had a concave surface, thus the use of an O-ring to contain the NP solutions was not required.

Skin integrity was investigated at 6 and 24 hours. LM and TEM images obtained in this study are shown in Figure 6.2. The LM image of the mouse skin cultured for 24 hours in the conditions illustrated in Figure 3.3 does not show any visible alteration of the skin integrity, however the TEM images showed cells with broken cellular membranes and absence of cell organelles (Figure 6.2, 4th row, red arrows). At 6 hours of incubation, LM and TEM analysis

confirmed the maintenance of the skin integrity with no obvious tissue or cellular degeneration and therefore these were the conditions chosen for the mouse skin penetration experiments using mouse skin.

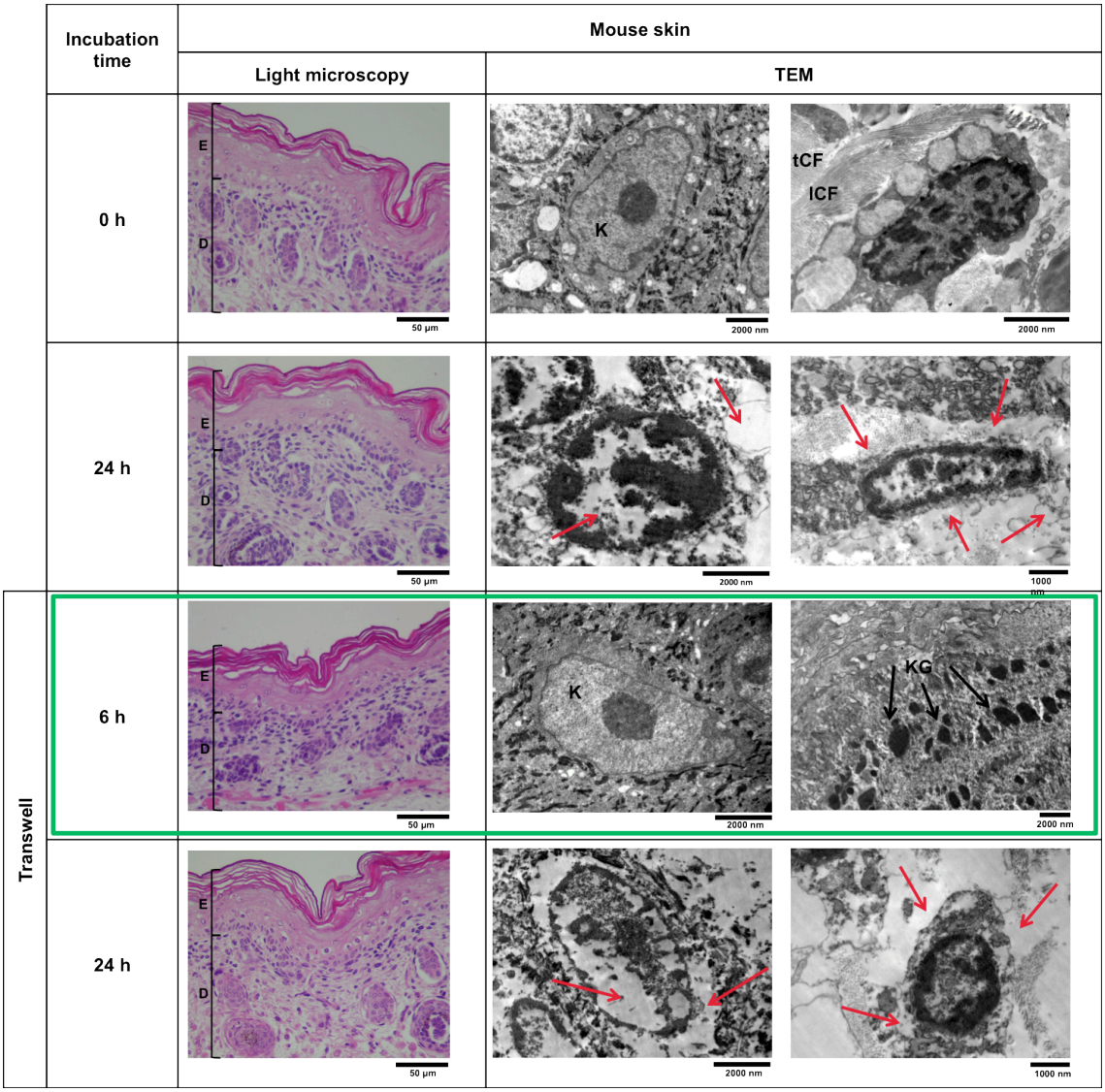

Figure 6.2 Evaluation of mouse skin integrity when cultured without (2nd row) and with (3rd and 4th rows) transwell inserts for different incubation times, by LM and TEM. Red arrows indicate degraded areas in the skin. The green rectangle highlights the conditions chosen for the mouse skin penetration experiment. K: keratinocyte; Fb: fibroblast; lCF: longitudinal collagen fibres; tCF: transversal collagen fibres; KG: keratohyalin granules.

6.3 Skin penetration by gold nanoparticles

To assess the extent to which different types of NPs diffuse through the skin, the initial concentrations of colloidal particles applied to the skin were relatively high, *i.e.* 100 nM for gold NS and 14 nM for gold NR. The human and mouse skin were exposed to NPs for the maximum know time for which the skin preserved its integrity in the experimental respective setup, *i.e.* 24 hours for human skin and 6 hours for mouse skin.

In the penetration experiments, the aqueous droplets of the different types of NPs were applied to the skin surface within the area of an O-ring, sealed to epidermis of the skin with Vaseline. The O-ring avoided edged-leakage and therefore undesirable edge penetration through the skin.

6.3.1 Assessment of skin penetration by inductively coupled plasma atomic emission spectrometry

ICP-AES was used to quantitatively evaluate the penetration of the different types of NPs through skin. In ICP-AES measurements, the sample is nebulized and transferred with an argon carrier gas stream into an argon plasma, where is desolvated, atomized and ionized. The emission spectra of the excited elements within the high-temperature plasma are measured to separate element-specific wavelengths of light. These are used for the identification of the element and the intensity of each emission is indicative of the concentration of the element within the sample.

After the skin exposure to the gold NPs, as described in Chapter 3, section 3.3.3, and prior to ICP-AES analysis, the remaining NP droplet was collected from the interior of the O-ring. The skin surface in the interior of the O-ring, previously in contact with the NPs solution, was washed twice with deionized water. The O-ring was then removed and the skin surface was tape-stripped six times to ensure that the SC was removed and with it any NPs attached to the uppermost layers of the skin. Tape stripping is a commonly used method to examine the localization and distribution of substances within the SC.[243-245] It is a minimally invasive technique to sequentially remove SC by the repeated

application of appropriate adhesive tapes.[246] The amount of SC removed by a single adhesive tape strip depends on several intrinsic factors such as the skin anatomical site[247], the age of the donor[248], the thickness of the SC[249], the composition and amount of lipids[250], the race[251] and the skin type.[252] Extrinsic factors including the force of removal from the skin[253, 254], the duration of pressure onto the skin[252] and topically applied substances, also have an affect the amount of SC removed by tape stripping.[255] In general, a uniform and homogeneous removal of the SC is required. The factors herein mentioned may affect this homogeneity of removal. Therefore, in this work the tape stripping procedure was equally applied in all the samples to avoid the undesirable influence of extrinsic factors and to assure a reliable cross-data comparison of the results from different samples.[256] The tape stripping procedure was preferred rather than other skin washing method, because it avoided the potential edge-contamination of skin by NPs.

The tape stripping procedure assured the ICP-AES signal was mostly produced by particles located within the skin and not the ones that possibly remained in the skin surface.

After tape stripping, each skin sample was dissolved in aqua regia (10%). Human skin had to be microwave digested to facilitate the dissolution process. Once the samples were dissolved, they were diluted (1:10 ratio) with Milli-Q water and ICP-AES measurements were performed.

ICP-AES results were obtained from three independent experiments for each type of NPs. It is worth mentioning that the experiments were carried on using a human skin specimen from one donor only and mouse skin specimens from 4 newborn mice. The same batches of gold NPs fully characterized were used in all the experiments.

Figure 6.3 shows ICP-AES results in terms of percentage of gold NPs found per skin samples relatively to the initial amount of NPs applied to the skin surface. It is shown that the percentage of NPs found in the skin for NSs and NRs of opposite charge (Figure 6.3, top), and for the three types of peptide-functionalised NPs in comparison to the non-functional PEGylated NSs (Figure 6.3, bottom).

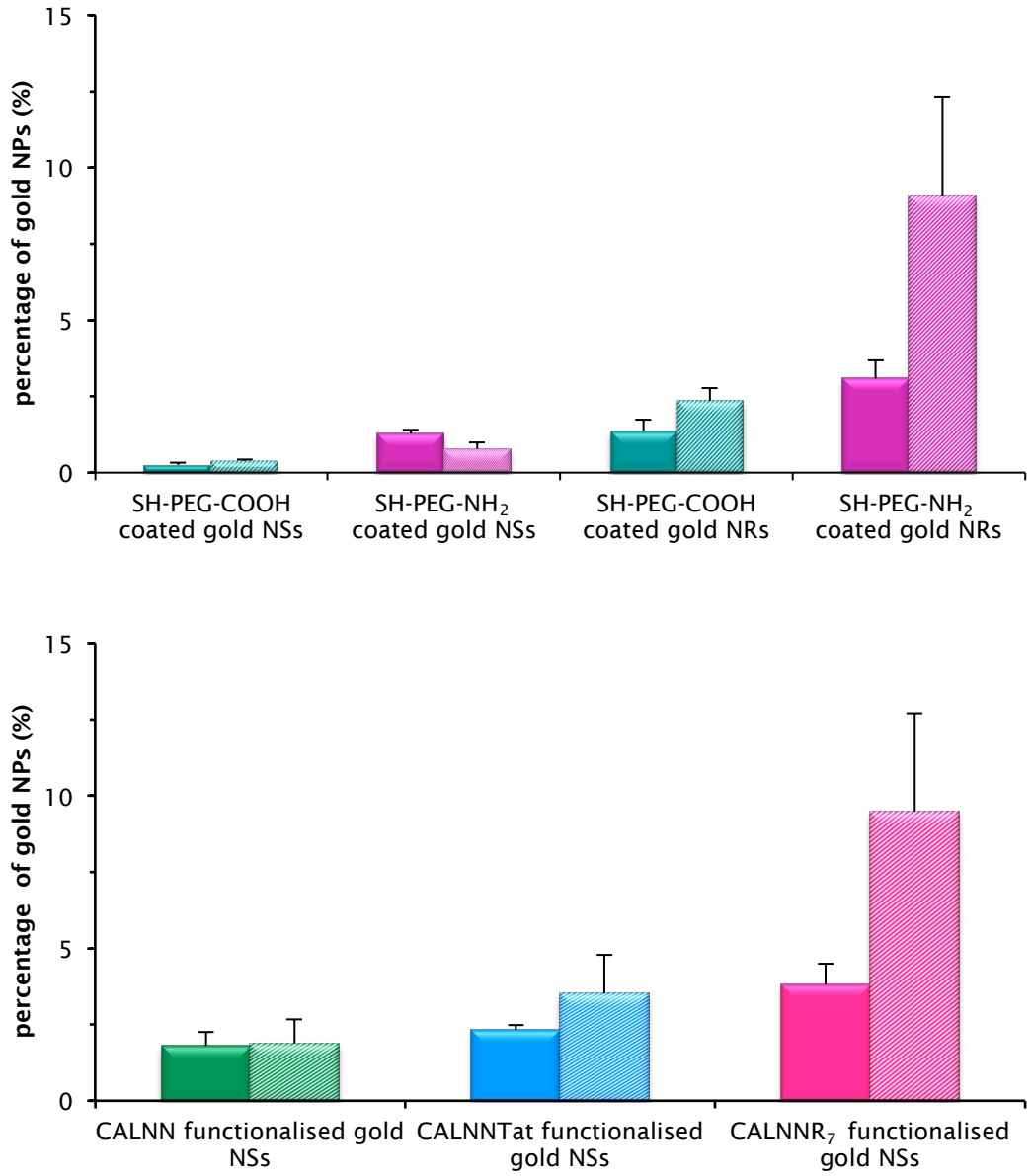

Figure 6.3 ICP-AES measurements showing the percentage of gold NPs found in the human (solid bars) and mouse (striped bars) skin. The percentage was calculated by assigning the value of 100% to the initial amount of NPs applied to the skin surface. The top graph shows the results of the PEGylated gold NSs and gold NRs to compare the effect of NP shape and charge on the penetration. The bottom graph shows results of the peptide-functionalised gold NSs, to investigate the effect of NP functionalisation on the penetration. Data are means ± SE, n=3.

As can be seen, there is a clear trend in that the percentage of positively charged PEGylated NPs found in the skin in higher (1.5 to 3 times) than the percentage of their negatively charged counterparts. The same tendency, *i.e.* positively charge particles show to have higher penetration than negative ones, was observed in a recent studies with liposomes, were cationic liposomes penetrate the skin more efficiently than anionic ones.[257] The enhanced skin permeation of cationic liposomes was attributed to the "Donnan exclusion effect" that is related with the more efficient interaction of cationic particles with the negatively charged skin cells.

The second observation is that the percentage of NRs found in the skin is higher than the percentage of NSs, especially in mouse skin. Several studies have demonstrated an effect of NP geometry on the uptake in cells in culture, related to the radius curvature.[234, 258, 259] Possible, there is a similar contribution of particle geometry in the interactions of NPs with the skin tissue.

Thirdly, there is an overall trend that the percentage of peptide-functionalised NSs were found in skin in larger numbers (up to 37 times more in some cases) compared to PEGylated NSs, suggesting that an electrostatic interaction between the positively charged arginine groups of Tat and R_7 and negatively charged skin cell surfaces was responsible for the skin binding of these peptides and also for their translocation through the skin. Additionally, this much higher penetration of the peptide-functionalised NSs may be also attributed the enhanced penetrating properties of the functional peptides.

Figure 6.4 shows the same ICP-AES results, in terms of number of NPs found in the skin. These graphs show the same main penetration trends previously pointed out, *i.e.* positively charged gold NPs showed high penetration than the negative ones, regardless their shape; NRs penetration is higher than spheres and peptide-functionalised NSs showed higher penetration than PEGylated gold NSs. It is interesting to notice that the number of $CALNNR_7$ gold NSs found in the skin is 7-30 times higher than the PEGylated gold NSs, emphasizing the importance of surface coverage in penetration.

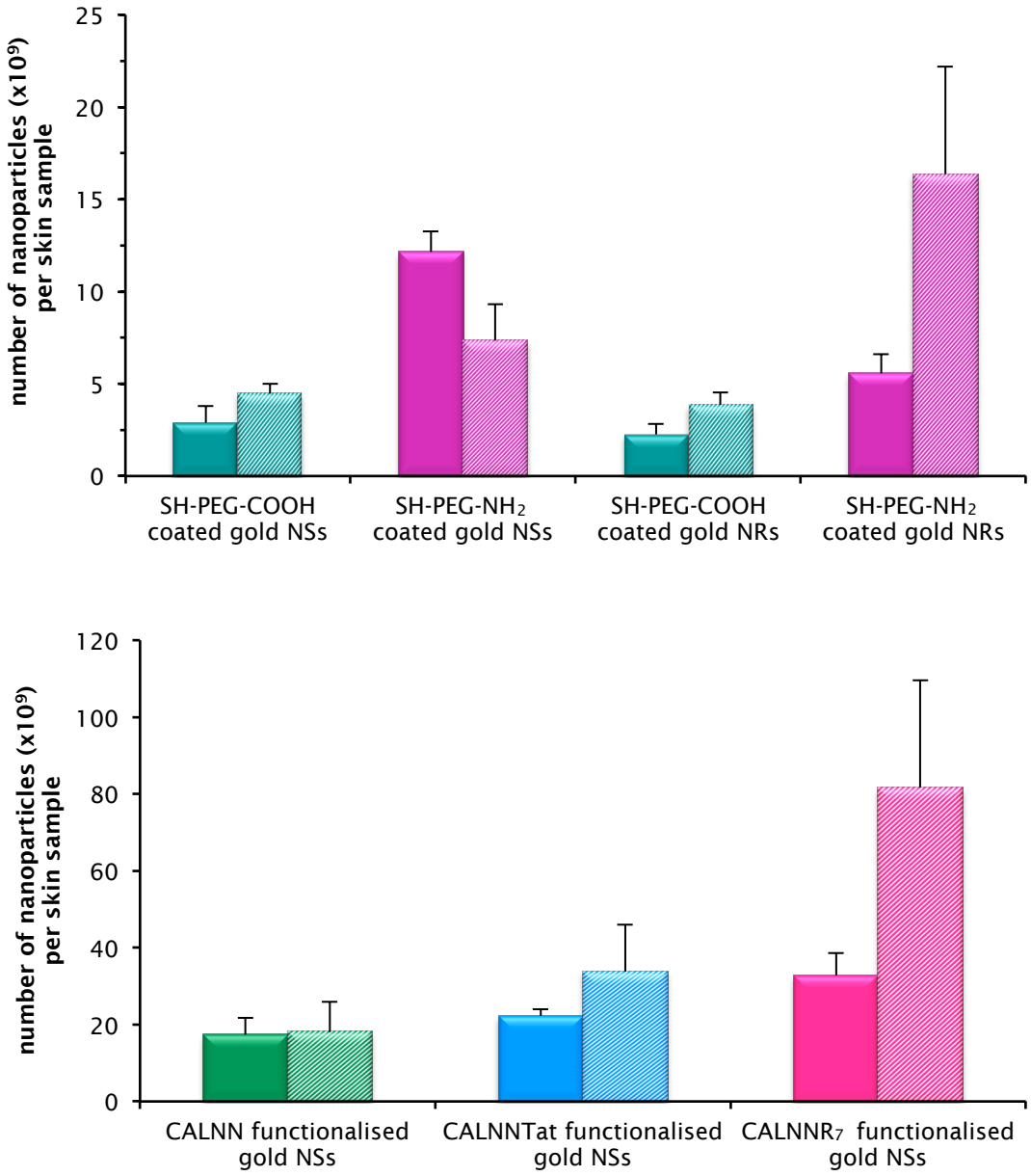

Figure 6.4 ICP-AES measurements showing the number of gold NPs per sample of human (solid bars) and mouse (striped bars) skin. The top graph shows the results of the PEGylated gold NSs and gold NRs to compare the effect of NP shape and charge on the penetration. The percentage was calculated by assigning the value of 100% to the initial amount of NPs applied to the skin surface. The bottom graph shows results of the peptide-functionalised gold NSs, to investigate the effect of NP functionalisation on the penetration. Data are means ± SE, n=3.

There was a tendency for the amount of gold NPs found in mouse skin to be higher that in human skin. This can be explained by the fact that viable mouse skin is thinner and more permeable to NPs than viable human skin.[97, 260]

As the results from ICP-AES take into account the entire skin with all layers, no assessment about the exact location (SC, epidermis or dermis) of the NPs can be made using this technique alone.

6.3.2 Assessment of skin penetration by transmission electron microscopy

TEM was performed to qualitatively assess the distribution of NPs in the skin, allowing the location of gold NPs in different skin layers.

For TEM analysis, the skin samples were cut into 90 nm-thick transversal sections. It is worth noting that the skin sectioning is a delicate process and needs to be performed cautiously to avoid contamination from the top to deeper layers of the skin with NPs. To avoid this, when cutting the ultrathin sections, the epidermis was orientated perpendicularly to the blade. Thus, all the skin layers were cut simultaneously and the part of the blade cutting the top skin layers never got in contact with deeper skin layer and vice-versa. These sections are very thin and it is not expected to see a large number of particles, nevertheless they provide information about the NP location within the sectioned regions.

Figure 6.5 and Figure 6.6 show TEM images of skin sections treated with NPs. Regardless their shape, charge and function, NPs were found in all layers of the skin, including the deeper layers *i.e.* epidermis and dermis.

The images H in Figure 6.5 and Figure 6.6 show an overview of dermis of healthy not-treated human and mouse skin, respectively.

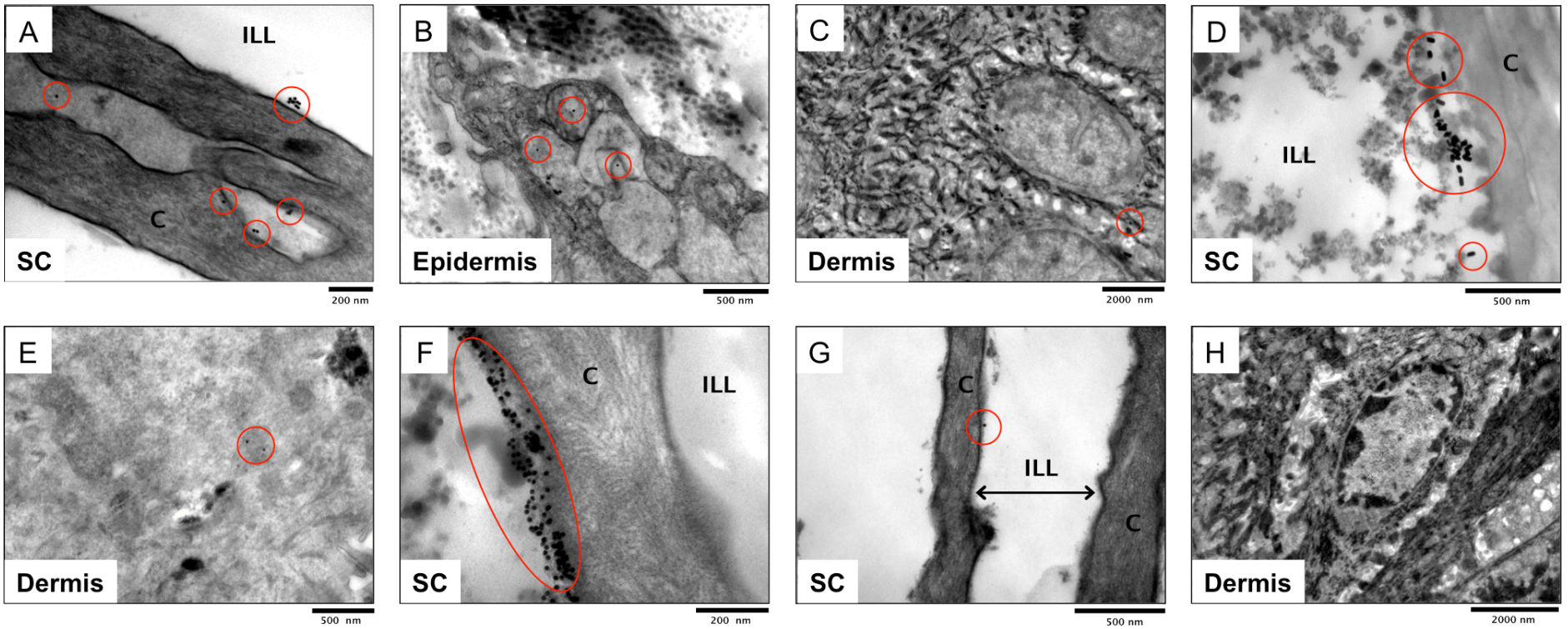

Figure 6.5 TEM images of ultrathin sections human skin incubated with SH-PEG-COOH-coated gold NSs (A); SH-PEG-NH_2-coated gold NSs (B); SH-PEG-COOH-coated gold NRs (C); SH-PEG-NH_2-coated gold NRs (D); CALNN-functionalised gold NSs (E); CALNNTat-functionalised gold NSs (F) and $CALNNR_7$-functionalised gold NSs (G). Untreated skin (H). Red circles indicate the presence of NPs in the different skin layers: SC, epidermis and dermis (Figure 2.1 and Figure 2.2). ILL: intercellular lipid lamellae; C: corneocyte.

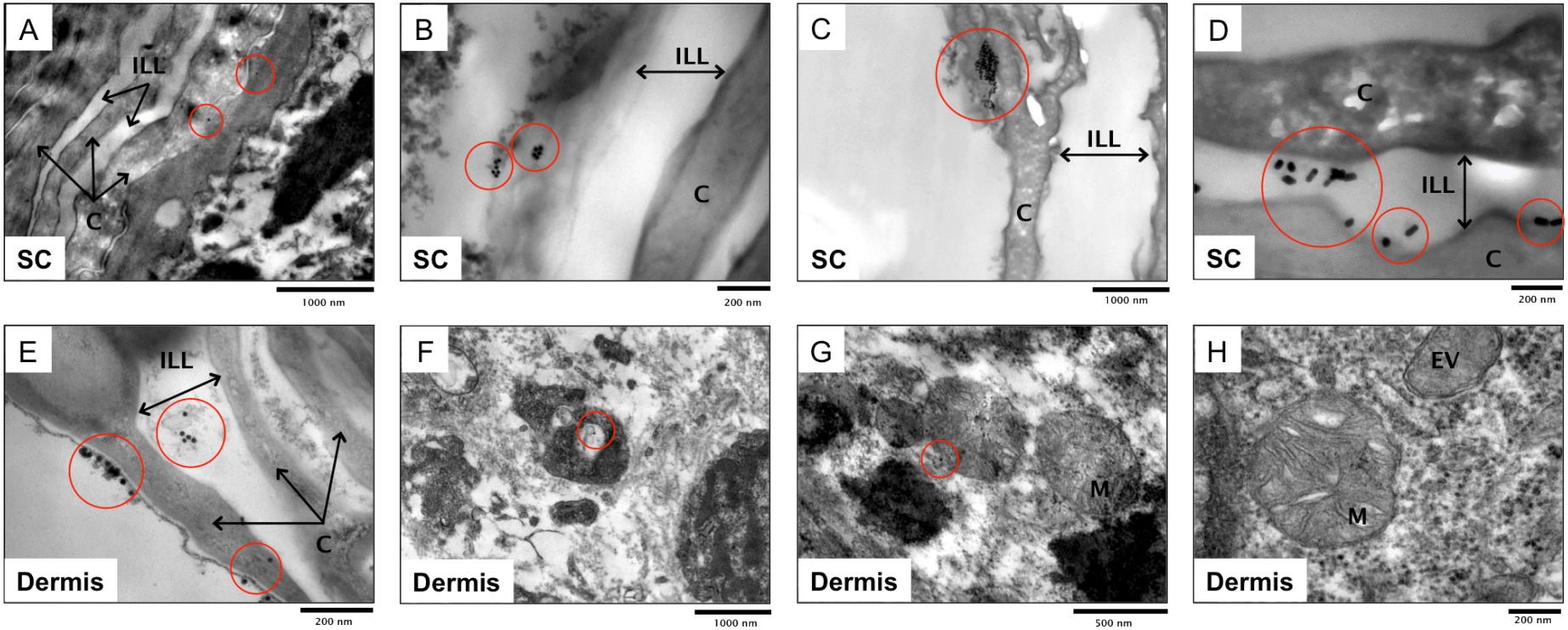

Figure 6.6 TEM images of ultrathin sections mouse skin incubated with SH-PEG-COOH-coated gold NSs (A); SH-PEG-NH_2-coated gold NSs (B); SH-PEG-COOH-coated gold NRs (C); SH-PEG-NH_2-coated gold NRs (D); CALNN-functionalised gold NSs (E); CALNNTat-functionalised gold NSs (F) and $CALNNR_7$-functionalised gold NSs (G). Untreated skin (H). Red circles indicate the presence of NPs in the different skin layers: SC, epidermis and dermis (Figure 2.1 and Figure 2.2). ILL: intercellular lipid lamellae; C: corneocyte; M: mitochondria; EV: endocytic vesicle.

After gold NPs exposure, o evident signs of toxicity were found either in human or mouse skin by analysis of the TEM images.

NPs found in the SC were generally located in the intercellular spaces between the corneocites (Figure 6.5 Images A, D, F, G and Figure 6.6 Images A, B, C, D, E). This might be an indicative that gold NPs diffuse through the skin using the paracellular pathway. This is in agreement with a study by Labouta *et al.*[75] who showed that 6 nm and 15 nm gold NPs permeate the SC mainly through the paracellular pathway, in a similar manner to drug molecules.

When compared with non-functionalised gold NPs, the NPs coated with CCPs were found deeper in the mouse dermis (Figure 6.6 Image F and G) and in higher amounts in the human SC, especially the CALNNTat -functionalised gold NPs (Figure 6.5 Image F).

Meanwhile, when the NPs reached the dermis they were found either inside the cells (Figure 6.5 Image B) or in the intercellular spaces (Figure 6.5 Image C and Figure 6.6 Image F and D).

Due to the high difficulty in locating the nano-sized particles in the ultrathin sections of compact skin tissue, a TEM quantitative analysis would not be accurate. Therefore, this analysis was not performed.

To confirm the elemental composition of the NPs found in the TEM images of ultrathin sections of the skin, EDX analysis was performed and results are shown in Figure 6.7. EDX uses the electron beam of an electron microscope that interacts with the atoms in the sample displacing electrons from their energy levels. A position vacated by an electron ejected from an inner shell is occupied by a higher-energy electron from an outer shell, accompanied by an X-ray emission. Atoms of each element release X-rays with unique amounts of energy during the electron transfer process. These characteristic energies of the emitted X-rays can then be used to identify the elements in the sample.[261]

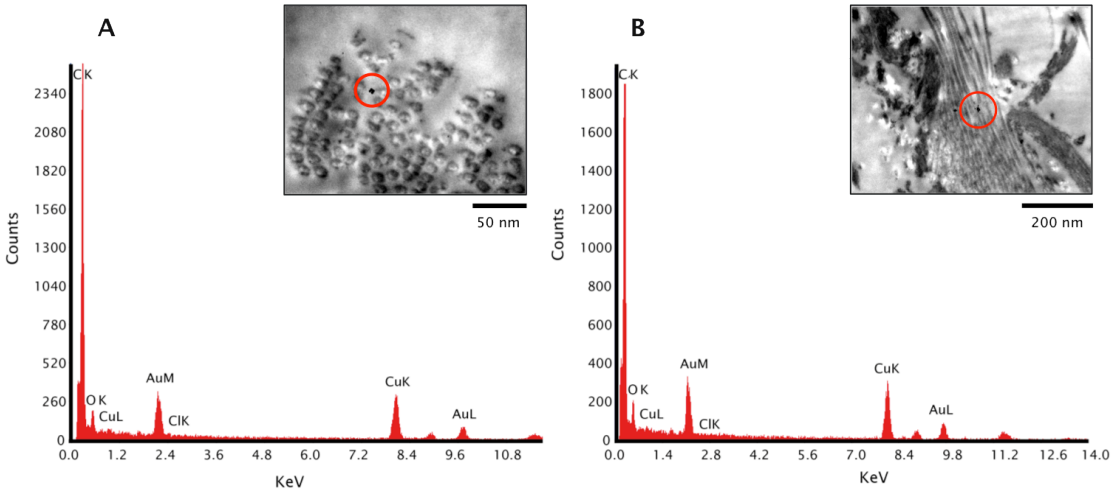

Figure 6.7 EDX spectra obtained from the analysis of TEM images of ultrathin sections of human skin containing SH-PEG-COOH-coated gold NPs (A) and SH-PEG-NH_2-coated gold NPs (B). Red circles indicate the presence of gold NPs.

The revealed peaks of gold on the EDX spectra confirmed the presence of gold NPs in the skin specimens after 24 hours of NP-treatment. The copper peak in spectra was originated by the scattering from the TEM copper mesh grid that supported the skin section.

6.3.3 Assessment of skin penetration by photoluminescence microscopy

PL microscopy allows the characterization of larger areas and thicker sections (14 μm), when compared to TEM, providing an overview of the distribution of densities of particles with micrometer resolution. For the PL microscopy analysis of the skin samples, a novel apparatus was built using a femtosecond-pulsed laser, operating at a wavelength of 515 nm. Compared to most PL microscopy studies using near-infrared laser excitation, this is

well matched to the localized surface plasmon resonance of individual gold NSs.

For the PL microscopy study, fixed paraffin section were prefer rather than frozen section. Paraffin sections yield better histological preservation than frozen sections.[153] Additionally, paraffin blocks allow the used of larger pieces of tissue and are easier to store.

Figure 6.8 shows the bright field and PL microscopy images of sections of mouse skin incubated with the different type of NPs.

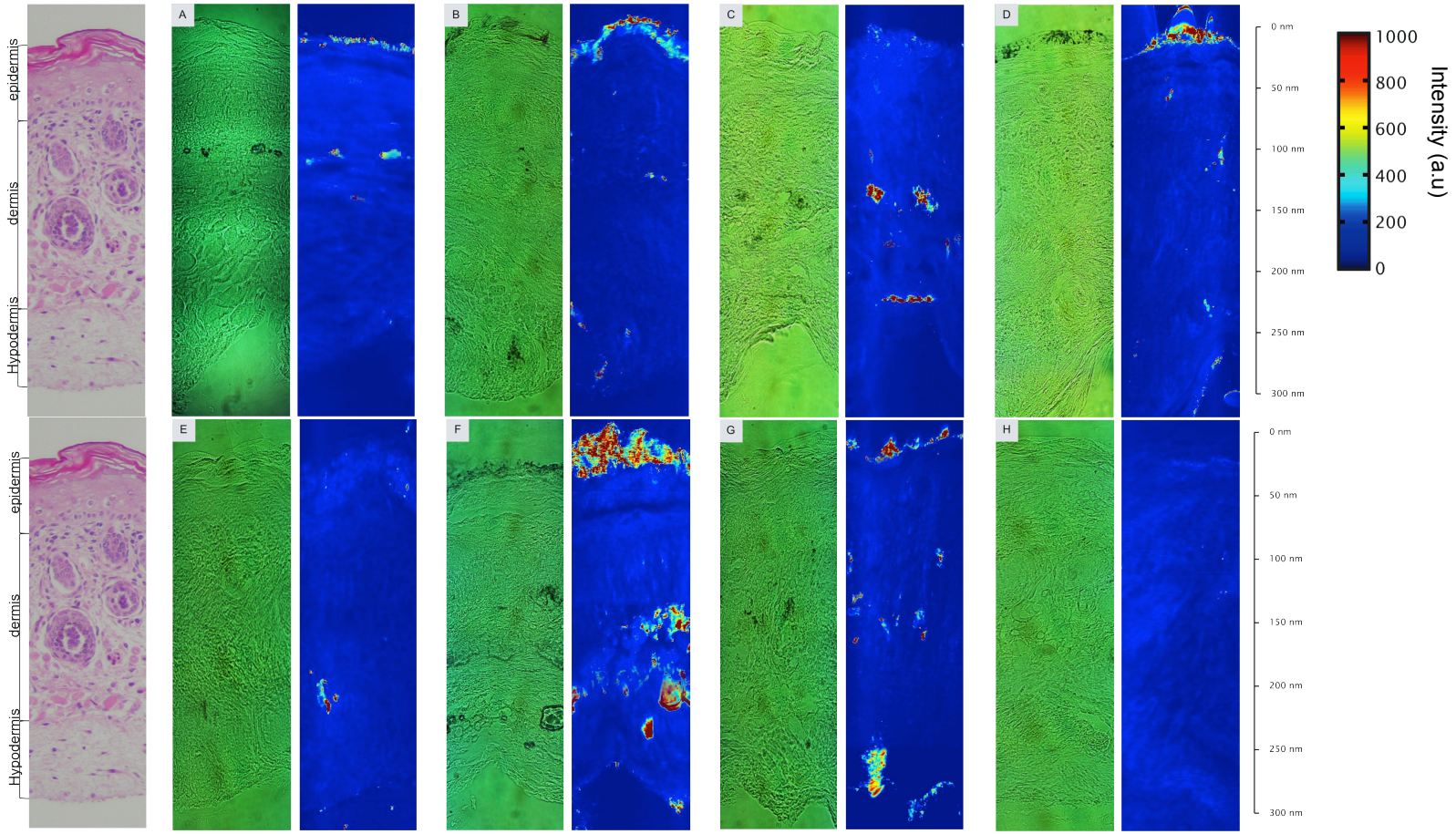

Figure 6.8 Bright field and PL microscopy images of mouse skin incubated with SH-PEG-COOH-coated gold NSs (A); SH-PEG-NH_2-coated gold NSs (B); SH-PEG-COOH-coated gold NRs (C); SH-PEG-NH_2-coated gold NRs (D); CALNN-functionalised gold NSs (E); CALNNTat-functionalised gold NSs (F) and $CALNNR_7$-functionalised gold NSs (G). Untreated skin (H).

The bright spots in the images indicate the presence of the NPs, which penetrate deeper in the dermis in the case of CALNNTat and $CALNNR_7$-functionalised gold NSs. PL microscopy allows to visualize groups of more than 10 NPs. In the skin samples incubated with CALNNTat and $CALNNR_7$-functionalised gold NSs, the macroscale organization of NPs clearly takes place in certain areas of the dermis.

The greater penetration in depth by the NPs functionalized with CALNNTat and $CALNNR_7$ when compared with the other NPs used in this work may be attributed to the key role of Tat and R_7 as CPPs. It should be noted that both human and mouse skin samples were not tape-striped for PL microscopy measurements. For this reason, high densities of NPs are also observed at the surface of the skin. While at this stage no conclusive answer can be given regarding the macroscale organization of NPs in the deeper layers of the skin, it is possible that these are concentrated in cells, specially aimed at harvesting infiltrating material or infectious agents. Indeed, studies of intradermal-injected quantum dots have indicated evidence of translocation of NPs to adjacent lymph nodes via skin macrophages and dendritic or Langerhans cells.[46] Intradermal injections deliver substances directly into the dermis, avoiding the barrier presented by the SC. This is not the case of the experiments reported in the current work, where the route of administration is transdermal, *i.e.* NPs are applied in the surface of the skin and have to overcome the SC and all epidermal layers in order to reach the dermis. Nevertheless, translocation mechanisms as the one reported for intradermal injections of quantum dots, may be a possible explanation for the observed of NPs clustering deep inside the dermis layer.

6.4 Conclusion

The penetration of different types of gold NPs with through human and mouse skin was investigated and the effect of the NPs charge, shape and functionalisation in the penetration was evaluated. The systematic study carried on includes quantitative and qualitative characterization of the skin samples after exposure to gold NPs and concluded that there is an overall

trend that positively charged NPs penetrated the skin in larger numbers, when compared with their negatively charged counterparts. Also, it was observed that rod-shape NPs were found in the skin in much higher numbers than spheres, thus the morphology of the particle has to be taken into account in such studies. Moreover, peptide-functionalised NSs penetrate the skin in larger numbers (up to 30 times more in some cases) in comparison to PEGylated NSs, highlighting the important role of CPPs. In ultrathin sections (90 nm) TEM showed that the particles were found both in epidermis and dermis. In thick sections of skin (14 μm) PL microscopy studies showed that Tat and R_7 containing NPs migrate in large numbers in the deeper layers of the skin and present a macroscale organization.

Chapter 7 Conclusions and future work

The use of NPs in biomedicine holds potential for important developments in drug delivery, imaging, diagnosis and therapy.[262-265] This is fuelled by significant advancements in NP chemical synthesis and surface functionalisation, which allows designing the properties of the nanomaterial.[120, 266-272] Having available a rich library of nanomaterials, one of the biggest challenges is to understand the NP behaviour when introduced to biological structures.[273, 274] Currently, many studies focus on how the morphology, charge and ligand capping of NPs influence their cellular fate.[275-279] However, equally important and not yet well understood, is how the physicochemical characteristics of NPs influence their interactions multicellular tissues. A typical and highly relevant example of such a tissue is the skin. Understanding how the morphology, charge and functionalisation of NPs influences their penetration through the different layers of the skin is crucial for the future development of NP-based transdermal drug delivery methods, as well as for the toxicology field.

In the present work gold NPs were incubated MDCK-II cell monolayers, which constitute a reliable model for penetration across the skin barrier.[218] Seven types of gold NPs were used in this study, namely; SH-PEG-COOH gold NPs (negatively charged NSs), SH-PEG-NH_2 gold NPs (positively charged NSs), SH-PEG-COOH gold NRs (negatively charged NSs), SH-PEG-NH_2 gold NRs (positively charged NRs, CALNN-functionalised gold NSs (peptide-functionalised NSs), CALNNTat-functionalised gold NSs (CPPs-functionalised NSs) and $CALNNR_7$-functionalised gold NSs (skin-penetrating-peptide functionalised NSs).

The interaction of these seven types of gold NPs with tight junctions and their effect on the tight junction formation was evaluated by TEER. The exposure of MDCK-II cells monolayers, either before or after the tight junction formation, to gold NPs did not cause any change on TEER of the cell monolayer, when compared with TEER of untreated MDCK-II cells. The same result was observed for all the seven different types of NPs, indicating that the process of the tight junction formation and its maintenance is not affected by presence of the gold NPs, regardless the their shape, charge and functionalization.

The effect of charge, shape and surface functionalisation of gold NPs in their uptake by MDCK-II monolayers with formed tight junctions was evaluated by TEM. Results showed that gold NSs were taken up by MDCK-II cells to a higher extent than gold NRs of the same charge. Yang *et al.*[233] have showed that the capacity of a NP to cross a lipid bilayer depends on the contact area between the particle and the lipid bilayer, and on the orientation of the particles at the membrane, *i.e.* the local curvature of the particle at the contact point, which both are shape dependent. Additionally, cell culture studies on the effect of the NP shape in the uptake of NPs have shown that spherical NPs are taken up in greater number than rod-shaped particles of similar size and charge by mammalian cells.[234] The effect of NPs shape on their internalization, with spherical particles being taken up in higher number than rod-shaped particles of similar size and charge, might be explained by the greater membrane wrapping time required for the elongated particles. Also, it has been hypothesised that any interactions that do occur between rod-shaped NPs and cell surfaces are easily disrupted under strong hydrodynamic shear minimizing the opportunity for cell uptake. In contrast, spherical NPs are less influenced by shear and are able to interact more strongly with the cell surface, increasing their cellular uptake.[235]

From the analysis of TEM images, it appears that size, but not the charge, determines the level of uptake of gold NPs. PEGylated gold NRs were found outside the cells, nearby the microvilli; while single PEGylated gold NSs were found enclosed in vesicles. Additionally, TEM investigation showed that gold NPs functionalised with CALNN, CALNNTat and $CALNNR_7$ were taken up in higher number by MDCK-II cells than the other types of gold NPs. CALNN, CALNNTat and $CALNNR_7$ –functionalised gold NPs were mainly found in large

groups enclosed in vesicles in the cell cytoplasm, suggesting that the uptake mechanism was endocytosis, which is in agreement with previous studies.[114]

Furthermore, TEM analysis showed that, regardless NP shape, charge and functionalization, MDCK-II physiological structure was preserved after 24 hours incubation with gold NPs. This might be an indicative of the non-toxicity of gold NPs to MDCK-II cells, under the experimental conditions used in this thesis.

For the skin penetration experiment, two different setups were designed for human and mouse skin. The optimized setups guaranteed that human and mouse skin integrity was preserved, for the designated incubation times. For human skin, the selected setup consisted in the incubation of the skin immersed in medium, while maintaining the skin surface dry. Under these conditions, the maximum incubation time for each the human skin conserved its integrity was 24 hours. However, mouse skin lost its integrity when submitted to these conditions. Hence, a new setup to study the penetration through mouse skin was designed. The mouse skin setup involved the skin incubation in a transwell insert with medium in the basal side only and not in the apical side. This assured that the skin surface was dry, while the deeper layers were in constant contact with medium. The maximum incubation time for each the mouse skin conserved its integrity was 6 hours. These experimental conditions were then applied to study the penetration of the seven types of gold NPs used in this thesis. ICP-AES was used to obtain a qualitative characterization of the NPs-treated skin samples, while TEM, EDX and PL microscopy were used to obtain a qualitative characterization.

ICP-AES results indicated that the NPs physicochemical parameters are key factors governing their skin penetration. Overall, positively charged NPs penetrated the skin in larger numbers (2-6 times) in comparison to their negatively charged counterparts. This might be attributed to the more efficient interaction of cationic particles with the negatively charged skin cells (Donnan exclusion effect). Additionally, rod-shape NPs were found in the skin in higher numbers than spheres. Moreover, there is a clear overall trend that the peptide-functionalised NSs employed in our experiments penetrate the skin in larger numbers (up to 30 times more in some cases) in comparison to PEGylated NSs, suggesting that an electrostatic interaction between the

positively charged arginine groups of Tat and R_7 and negatively charged skin cell surfaces was responsible for the skin binding of these peptides and also for their translocation through the skin. Additionally, this much higher penetration of the peptide-functionalised NSs may be also attributed the enhanced penetrating properties of the functional peptides.

In ultrathin sections (90 nm) TEM showed that the particles were found both in epidermis and dermis. After gold NPs exposure, o evident signs of toxicity were found either in human or mouse skin by analysis of the TEM images.

NPs found in the SC were generally located in the intercellular spaces between the corneocites, which might suggest that they diffuse through the skin using the paracellular pathway. This is in agreement with a study by Labouta *et al.*[75] who showed that 6 nm and 15 nm gold NPs permeate the SC mainly through the paracellular pathway, in a similar manner to drug molecules. When compared with non-functionalised gold NPs, the NPs coated with peptides were found in deeper skin layers, especially the CALNNTat fuctionalised gold NPs. Peptide functionalised NPs were found in dermis, either inside the cells or in the intercellular spaces.

Furthermore, thick sections of skin (14 μm) investigated by PL microscopy showed that CALNNTat and CALNNR_7 functionalised gold NPs migrate in large numbers into the deeper layers of the skin, where they present a microscale organization.

Results from this work suggest that gold NPs penetrate across the SC through the intercellular spaces between the corneocites, following the paracellular pathway, in a similar manner to drug molecules. Once the NPs overcome the SC they may penetrate to deeper layers of the skin, *i.e.* the dermis, where they might be taken up by skin dendritic cells, such as Langerhans cells, as the microscopy organization of CALNNTat and CALNNR_7 functionalised gold NPs observed by PL microscopy suggests. As dermal dendritic cells are replace from the dermis every 72 hours,[280] our findings imply that the NPs accumulated in the dermis might be cleared by transport to the lymphatic or blood vessels – dermal clearance.[51] Apart from dermal clearance, a substance may also be effectively removed through metabolism in the skin.[53]

7.1 Recommendations for future work

Application of inorganic NPs in dermatology is a rapidly growing field of research. Despite the interest of researches, the ability of inorganic NPs to overcome the SC and reach deeper skin layers is controversial among the research community.[1, 40, 281] In an attempt to solve this dilemma, the following factors should be taken into consideration as recommendations for future work.

Firstly, human skin should be the primary choice for *in vitro* skin penetration experiments. Meanwhile, penetration studies using animal skin should be also performed, in order to find a correlation between *in vitro* and *in vivo* penetration studies in animal and human skin. Secondly, general guidelines for studies on the skin penetration by NPs, *e.g.* experimental setup, incubation times, NPs concentration, NPs dispersion medium and penetration enhancement approaches, should be developed. Thirdly, information regarding the experimental conditions, as well as NPs characterization and galenic formulation should be detailed in the published work.

The investigation of the skin penetration by inorganic NPs, aiming either the development of transdermal drug delivery systems or the health risk assessment, is a recent research area with promising potential. Challenges in future studies include the development of new analytical approaches and higher sensitivity techniques that allow tracking and quantitation of small concentrations of NPs present in the skin.

Furthermore, a complex DNA-coated gold NP system for transdermal gene delivery could be developed. Although gold NPs have been widely investigated as gene-carriers,[263, 282] there is limited information about the skin application of DNA-functionalised gold NPs for gene delivery. The efficiency of this complex DNA-coated gold NP, using plasmid DNA encoding for a reporter gene, could be evaluated by either green fluorescence protein or the enzyme luciferase expression.

Appendix A Reagent suppliers and analytical equipment

Reagents were purchased from the following suppliers and used as received, without further purification: trisodium citrate, sodium tetrachloroaurate (III) dehydrate, sodium chloride, L-ascorbic acid, BSPP, CTAB, sodium borohydride and Tween20 were purchased from Sigma-Aldrich. Silver nitrate was purchased from Fisher Scientific. SH-PEG-COOH, Mw = 5000 Dalton and SH-PEG-NH_2, Mw = 5000 Dalto and were purchased from Iris Biotech GmbH. CALNN, CALNNTat and CALNNR_7 were purchased from PeptideSynthetics (Peptide Protein Research Ltd).

DMEM, RPMI medium and FBS were purchased from Life Technologies Ltd. Penicillin/Streptomycin solution, trypsin and EDTA were purchased from sigma Aldrich.

Osmium (VIII) Oxide was purchased from OXKEM Limited. Acetonitrile, uranyl acetate and Xylene were purchased from Fisher Scientific. PIPES, Mowiol, glutaraldehyde and formaldehyde were purchased from Sigma Aldrich.

0.45 μm pore size, 25 mm diameter cellulose acetate membrane syringe filter was purchased from VWR international Lda. 3.05 mm diameter Carbon coated 400 mesh Copper grids, 3.05 mm diameter Palladium coated 200 mesh Copper grids and 3.05 mm diameter 200 mesh Nickel grids were purchased from Agar Scientific.

12 well costar® transwell-clear support tissue culture treated sterile polyester membrane (0.4 um pore size, 12 mm membrane diameter), cell culture 6-well and 12-well plates were purchased from Fisher Scientific.

3M™ Micropore™ Medical Tape and O-rings (O.D.= 8 mm; I.D.= 4 mm) were purchase from amazon.co.uk.

26x76mm 1mm-1.2mm thick microscope glass slides and 22x22mm n°1 cover glasses were purchased from VWR International.

Centrifugation of gold NP samples was performed in a Heraeus Biofuse Primo (Highconic motor; maximum capacity: 6 x 50 ml; maximum speed: 10000xg;

radius: 12.4 cm) and in an Eppendorf 5417R (high-speed aerosol-tight 24-place rotor (FA45-24-11); maximum capacity: 24 x 1.5/2.0 ml; maximum speed: 25000xg; radius: 8.3 cm; temperature range from –9˚C to 40˚C).

UV-Visible spectra of colloidal gold NPs were collected using a Cary 300 Bio UV-Visible spectrophotometer over the range from 350 to 800 nm. Electrophoretic light scattering and DLS measurements were obtained with a Malvern Zetasizer Nano E0248.

Ultrathin sections were cut on a Reichurt Om-U3 ultramicrotome and the glass knifes were made with a LKB knife maker. LM images were obtained with a Nikon Eclipse 600 equipped with a Nikon Coolpix 950 digital camera. TEM images were obtained with a FEI Technai12 TEM operating at a voltage of 80 kV. TEER measurements were made with an EVOM^2, Epithelial Voltohmmeter. EDAX X-ray spectrometer was used on the EDX analysis. PL microscopy images were obtained with a PL microscope. ICP-AES measurements were made with an ICAP 6300 duo Spectrophotometer

Milli-Q water was used in all experiments.

List of Publications

Fernandes, R.; Li, M.; Dujardin, E.; Mann, S.; Kanaras, A. G. (2010). Ligand-mediated self-assembly of polymer-enveloped gold nanoparticle chains and networks. *ChemComm*, 46(40), 7602-7604.

Schulz, K. M., Abb, S., Fernandes, R., Abb, M., Kanaras, A. G., Muskens, O. L. (2012). Formation and plasmonic response of self-assembled layers of colloidal gold nanorods and branched gold nanoparticles. Langmuir, 28(24), 8874-8880.

Fairbairn, N.; Light, R. A.; Carter, R.; Fernandes, R.; Kanaras, A. G.; Elliott, T. J.; Muskens, O. L. (2012). Spatial modulation microscopy for real-time imaging of plasmonic nanoparticles and cells. *Opt Lett,* 37(15), 3015-3017.

Fairbairn, N.; Fernandes, R.; Carter, R.; Elliot, T. J.; Kanaras, A. G.; Muskens, O. L. (February 22, 2013). Single-nanoparticle detection and spectroscopy in cells using a hyperspectral darkfield imaging technique. Proc. SPIE 8595, *Colloidal Nanocrystals for Biomedical Applications VIII*, 859501

Fernandes, R.; Smyth N.; Kanaras, A. G. (2014). Interactions of gold nanoparticles with biological structures. Proc. SPIE 8955-25, *Colloidal Nanoparticles for Biomedical Applications IX*, 8955.

Fernandes, R.; Smyth, N. R.; Muskens, O. L.; Nitti, S.; Heuer-Juengemann, A.; Ardern-Jones, M.; Kanaras, A. G. (2014). Interactions of Skin with Gold Nanoparticles of Different Surface Charge, Shape and Functionality. *Small*. (Accepted)

Kymakis, E.; Spyropoulos, G.; Fernandes, R.; Kanaras, A. G.; Stratakis, E. (2014). Plasmonic bulk heterojunction solar cells: The role of nanoparticle ligand coating. (Submitted)

Bibliography

1. Labouta, H.I. & Schneider, M. Interaction of inorganic nanoparticles with the skin barrier: current status and critical review. *Nanomedicine : nanotechnology, biology, and medicine* **9**, 39-54 (2013).
2. Madison, K.C. Barrier Function of the Skin: La Raison d'Etre of the Epidermis. *J Investig Dermatol* **121**, 231-241 (2003).
3. Meigel, W.N., Gay, S. & Weber, L. Dermal architecture and collagen type distribution. *Archives of dermatological research* **259**, 1-10 (1977).
4. Fuchs, E. & Raghavan, S. Getting under the skin of epidermal morphogenesis. *Nat Rev Genet* **3**, 199-209 (2002).
5. Mackenzie, I.C. Ordered structure of the epidermis. *J Investig Dermatol* **65**, 45-51 (1975).
6. Benson, H.A. Transdermal drug delivery: penetration enhancement techniques. *Current drug delivery* **2**, 23-33 (2005).
7. Barbero, A.M. & Frasch, H.F. Transcellular route of diffusion through stratum corneum: Results from finite element models. *Journal of pharmaceutical sciences* **95**, 2186-2194 (2006).
8. Marks, R., Barton, S.P. & Edwards, C. The Physical nature of the skin. (MTP Press, Lancaster, England; Boston; 1988).
9. Boguniewicz, M. & Leung, D.Y. Atopic dermatitis: a disease of altered skin barrier and immune dysregulation. *Immunological reviews* **242**, 233-246 (2011).
10. Mattozzi, C., Richetta, A.G., Cantisani, C., Macaluso, L. & Calvieri, S. Psoriasis: new insight about pathogenesis, role of barrier organ integrity, NLR / CATERPILLER family genes and microbial flora. *The Journal of dermatology* **39**, 752-760 (2012).
11. Yosipovitch, G., Tur, E., Cohen, O. & Rusecki, Y. Skin surface pH in intertriginous areas in NIDDM patients. Possible correlation to candidal intertrigo. *Diabetes care* **16**, 560-563 (1993).
12. Biniek, K., Levi, K. & Dauskardt, R.H. Solar UV radiation reduces the barrier function of human skin. *Proceedings of the National Academy of Sciences of the United States of America* **109**, 17111-17116 (2012).
13. Levang, A.K., Zhao, K. & Singh, J. Effect of ethanol/propylene glycol on the in vitro percutaneous absorption of aspirin, biophysical changes and macroscopic barrier properties of the skin. *International journal of pharmaceutics* **181**, 255-263 (1999).
14. Varani, J. et al. Human skin in organ culture and human skin cells (keratinocytes and fibroblasts) in monolayer culture for assessment of chemically induced skin damage. *Toxicologic pathology* **35**, 693-701 (2007).
15. Walter, A. et al. Aldara activates TLR7-independent immune defence. *Nature communications* **4**, 1560 (2013).
16. Simpson, C.L., Patel, D.M. & Green, K.J. Deconstructing the skin: cytoarchitectural determinants of epidermal morphogenesis. *Nature reviews. Molecular cell biology* **12**, 565-580 (2011).
17. Anderson, J.M. & Van Itallie, C.M. Physiology and Function of the Tight Junction. *Csh Perspect Biol* **1** (2009).

18. Morita, K. & Miyachi, Y. Tight junctions in the skin. *Journal of dermatological science* **31**, 81-89 (2003).
19. Shin, K., Fogg, V.C. & Margolis, B. Tight junctions and cell polarity. *Annu Rev Cell Dev Bi* **22**, 207-235 (2006).
20. Fanning, A.S., Mitic, L.L. & Anderson, J.M. Transmembrane proteins in the tight junction barrier. *Journal of the American Society of Nephrology : JASN* **10**, 1337-1345 (1999).
21. Rodriguez-Boulan, E. & Macara, I.G. Organization and execution of the epithelial polarity programme. *Nature reviews. Molecular cell biology* **15**, 225-242 (2014).
22. Benson, K., Cramer, S. & Galla, H.J. Impedance-based cell monitoring: barrier properties and beyond. *Fluids and barriers of the CNS* **10**, 5 (2013).
23. Wegener, J., Abrams, D., Willenbrink, W., Galla, H.J. & Janshoff, A. Automated multi-well device to measure transepithelial electrical resistances under physiological conditions. *BioTechniques* **37**, 590, 592-594, 596-597 (2004).
24. Anderson, J.M. & Van Itallie, C.M. Physiology and function of the tight junction. *Cold Spring Harb Perspect Biol* **1**, a002584 (2009).
25. Dukes, J.D., Whitley, P. & Chalmers, A.D. The MDCK variety pack: choosing the right strain. *BMC cell biology* **12**, 43 (2011).
26. Crank, J. The mathematics of diffusion / by J. Crank. (Clarendon Press, Oxford [England]; 1975).
27. Moser, K., Kriwet, K., Naik, A., Kalia, Y.N. & Guy, R.H. Passive skin penetration enhancement and its quantification in vitro. *European journal of pharmaceutics and biopharmaceutics : official journal of Arbeitsgemeinschaft fur Pharmazeutische Verfahrenstechnik e.V* **52**, 103-112 (2001).
28. Savoji, H., Mehdizadeh, A. & Ramazani Saadat Abadi, A. Transdermal nitroglycerin delivery using acrylic matrices: design, formulation, and in vitro characterization. *ISRN pharmaceutics* **2014**, 493245 (2014).
29. Williams, A.C. Transdermal and Topical Drug Delivery: from Theory to Clinical Practice. (Pharmaceutical Press, London, UK; 2003).
30. Hoang, K.T. Dermal Exposure Assessment: Principles and Applications. (U.S. Environmental Protection Agency, Office of Health and Environmental Assessment, Washington, DC; 1992).
31. Labouta, H.I., Thude, S. & Schneider, M. Setup for investigating gold nanoparticle penetration through reconstructed skin and comparison to published human skin data. *Journal of biomedical optics* **18** (2013).
32. Mathur, V., Satrawala, Y. & Rajput, M. Physical and chemical penetration enhancers in transdermal drug delivery system. *Asian Journal of Pharmaceutics* **4**, 173-183 (2010).
33. Tang, H., Mitragotri, S., Blankschtein, D. & Langer, R. Theoretical description of transdermal transport of hydrophilic permeants: application to low-frequency sonophoresis. *Journal of pharmaceutical sciences* **90**, 545-568 (2001).
34. Cevc, G. Lipid vesicles and other colloids as drug carriers on the skin. *Advanced drug delivery reviews* **56**, 675-711 (2004).
35. Potts, R.O. & Francoeur, M.L. The influence of stratum corneum morphology on water permeability. *The Journal of investigative dermatology* **96**, 495-499 (1991).
36. Johnson, M.E., Blankschtein, D. & Langer, R. Evaluation of solute permeation through the stratum corneum: lateral bilayer diffusion as

the primary transport mechanism. *Journal of pharmaceutical sciences* **86**, 1162-1172 (1997).
37. Zhang, L.W., Yu, W.W., Colvin, V.L. & Monteiro-Riviere, N.A. Biological interactions of quantum dot nanoparticles in skin and in human epidermal keratinocytes. *Toxicology and applied pharmacology* **228**, 200-211 (2008).
38. Lee, S.E. et al. Penetration pathways induced by low-frequency sonophoresis with physical and chemical enhancers: iron oxide nanoparticles versus lanthanum nitrates. *The Journal of investigative dermatology* **130**, 1063-1072 (2010).
39. Lademann, J. et al. Hair follicles--an efficient storage and penetration pathway for topically applied substances. Summary of recent results obtained at the Center of Experimental and Applied Cutaneous Physiology, Charite -Universitatsmedizin Berlin, Germany. *Skin pharmacology and physiology* **21**, 150-155 (2008).
40. Baroli, B. Penetration of nanoparticles and nanomaterials in the skin: fiction or reality? *Journal of pharmaceutical sciences* **99**, 21-50 (2010).
41. Lekki, J. et al. On the follicular pathway of percutaneous uptake of nanoparticles: Ion microscopy and autoradiography studies. *Nuclear Inst. and Methods in Physics Research, B* **260**, 174-177 (2007).
42. Salmon, J.K., Armstrong, C.A. & Ansel, J.C. The skin as an immune organ. *The Western journal of medicine* **160**, 146-152 (1994).
43. Tinkle, S.S. et al. Skin as a route of exposure and sensitization in chronic beryllium disease. *Environmental health perspectives* **111**, 1202-1208 (2003).
44. Monteiro-Riviere, N.A., Nemanich, R.J., Inman, A.O., Wang, Y.Y. & Riviere, J.E. Multi-walled carbon nanotube interactions with human epidermal keratinocytes. *Toxicology letters* **155**, 377-384 (2005).
45. Sutariya, V.B. & Pathak, Y. (CRC Press, Boca Raton; 2014).
46. Kim, S. et al. Near-infrared fluorescent type II quantum dots for sentinel lymph node mapping. *Nat Biotechnol* **22**, 93-97 (2004).
47. Ohl, L. et al. CCR7 governs skin dendritic cell migration under inflammatory and steady-state conditions. *Immunity* **21**, 279-288 (2004).
48. Fuchs, E. Skin stem cells: rising to the surface. *The Journal of cell biology* **180**, 273-284 (2008).
49. Sengstock, C., Diendorf, J., Epple, M., Schildhauer, T.A. & Koller, M. Effect of silver nanoparticles on human mesenchymal stem cell differentiation. *Beilstein journal of nanotechnology* **5**, 2058-2069 (2014).
50. Samberg, M.E., Loboa, E.G., Oldenburg, S.J. & Monteiro-Riviere, N.A. Silver nanoparticles do not influence stem cell differentiation but cause minimal toxicity. *Nanomedicine (Lond)* **7**, 1197-1209 (2012).
51. Kretsos, K. & Kasting, G.B. Dermal capillary clearance: physiology and modeling. *Skin pharmacology and physiology* **18**, 55-74 (2005).
52. Nair, A., Jacob, S., Al-Dhubiab, B., Attimarad, M. & Harsha, S. Basic considerations in the dermatokinetics of topical formulations. *Brazilian Journal of Pharmaceutical Sciences* **49**, 423-434 (2013).
53. Jepps, O.G., Dancik, Y., Anissimov, Y.G. & Roberts, M.S. Modeling the human skin barrier--towards a better understanding of dermal absorption. *Advanced drug delivery reviews* **65**, 152-168 (2013).
54. Hansen, S.F. et al. Categorization framework to aid exposure assessment of nanomaterials in consumer products. *Ecotoxicology* **17**, 438-447 (2008).

55. Elder, A., Vidyasagar, S. & DeLouise, L. Physicochemical factors that affect metal and metal oxide nanoparticle passage across epithelial barriers. *Wiley interdisciplinary reviews. Nanomedicine and nanobiotechnology* **1**, 434-450 (2009).
56. Kemppainen, B.W., Reifenrath, W.G., Stafford, R.G. & Mehta, M. Methods for in vitro skin absorption studies of a lipophilic toxin produced by red tide. *Toxicology* **66**, 1-17 (1991).
57. Fielder, R.J., Gaunt, I.F., Rhodes, C., Sullivan, F.M. & Swanston, D.W. A hierarchical approach to the assessment of dermal and ocular irritancy: a report by the British Toxicology Society Working Party on Irritancy. *Human toxicology* **6**, 269-278 (1987).
58. Ghosh, P., Han, G., De, M., Kim, C.K. & Rotello, V.M. Gold nanoparticles in delivery applications. *Advanced drug delivery reviews* **60**, 1307-1315 (2008).
59. Alkilany, A.M., Thompson, L.B., Boulos, S.P., Sisco, P.N. & Murphy, C.J. Gold nanorods: their potential for photothermal therapeutics and drug delivery, tempered by the complexity of their biological interactions. *Advanced drug delivery reviews* **64**, 190-199 (2012).
60. Dreaden, E.C., Alkilany, A.M., Huang, X., Murphy, C.J. & El-Sayed, M.A. The golden age: gold nanoparticles for biomedicine. *Chemical Society reviews* **41**, 2740-2779 (2012).
61. Teow, Y., Asharani, P.V., Hande, M.P. & Valiyaveettil, S. Health impact and safety of engineered nanomaterials. *Chemical communications* **47**, 7025-7038 (2011).
62. Cross, S.E. et al. Human skin penetration of sunscreen nanoparticles: in-vitro assessment of a novel micronized zinc oxide formulation. *Skin pharmacology and physiology* **20**, 148-154 (2007).
63. Szikszai, Z. et al. Nuclear microprobe investigation of the penetration of ultrafine zinc oxide into intact and tape-stripped human skin. *Nucl Instrum Meth B* **268**, 2160-2163 (2010).
64. Menzel, F., Reinert, T., Vogt, J. & Butz, T. Investigations of percutaneous uptake of ultrafine TiO2 particles at the high energy ion nanoprobe LIPSION. *Nucl Instrum Meth B* **219**, 82-86 (2004).
65. Mortensen, L.J., Oberdorster, G., Pentland, A.P. & DeLouise, L.A. In vivo skin penetration of quantum dot nanoparticles in the murine model: The effect of UVR. *Nano letters* **8**, 2779-2787 (2008).
66. Ryman-Rasmussen, J.P., Riviere, J.E. & Monteiro-Riviere, N.A. Penetration of intact skin by quantum dots with diverse physicochemical properties. *Toxicological sciences : an official journal of the Society of Toxicology* **91**, 159-165 (2006).
67. Zhang, L.W. & Monteiro-Riviere, N.A. Assessment of quantum dot penetration into intact, tape-stripped, abraded and flexed rat skin. *Skin pharmacology and physiology* **21**, 166-180 (2008).
68. Larese, F.F. et al. Human skin penetration of silver nanoparticles through intact and damaged skin. *Toxicology* **255**, 33-37 (2009).
69. Samberg, M.E., Oldenburg, S.J. & Monteiro-Riviere, N.A. Evaluation of silver nanoparticle toxicity in skin in vivo and keratinocytes in vitro. *Environmental health perspectives* **118**, 407-413 (2010).
70. Baroli, B. et al. Penetration of metallic nanoparticles in human full-thickness skin. *The Journal of investigative dermatology* **127**, 1701-1712 (2007).

71. Sonavane, G. et al. In vitro permeation of gold nanoparticles through rat skin and rat intestine: effect of particle size. *Colloids and surfaces. B, Biointerfaces* **65**, 1-10 (2008).
72. Krishnan, G., Edwards, J., Chen, Y. & Benson, H.A. Enhanced skin permeation of naltrexone by pulsed electromagnetic fields in human skin in vitro. *Journal of pharmaceutical sciences* **99**, 2724-2731 (2010).
73. Filon, F.L. et al. Human skin penetration of gold nanoparticles through intact and damaged skin. *Nanotoxicology* **5**, 493-501 (2011).
74. Seto, J.E., Polat, B.E., Lopez, R.F., Blankschtein, D. & Langer, R. Effects of ultrasound and sodium lauryl sulfate on the transdermal delivery of hydrophilic permeants: Comparative in vitro studies with full-thickness and split-thickness pig and human skin. *Journal of controlled release : official journal of the Controlled Release Society* **145**, 26-32 (2010).
75. Labouta, H.I., el-Khordagui, L.K., Kraus, T. & Schneider, M. Mechanism and determinants of nanoparticle penetration through human skin. *Nanoscale* **3**, 4989-4999 (2011).
76. Labouta, H.I. et al. Gold nanoparticle penetration and reduced metabolism in human skin by toluene. *Pharmaceutical research* **28**, 2931-2944 (2011).
77. Labouta, H.I., El-Khordagui, L.K. & Schneider, M. Could chemical enhancement of gold nanoparticle penetration be extrapolated from established approaches for drug permeation? *Skin pharmacology and physiology* **25**, 208-218 (2012).
78. Chen, H.-Y., Zhao, Q., Su, K.-L. & Lin, Y.-C. in Nano/Micro Engineered and Molecular Systems, 2008. NEMS 2008. 3rd IEEE International Conference on 996-999 (2008).
79. Huang, Y.Z. et al. Co-administration of protein drugs with gold nanoparticles to enable percutaneous delivery. *Biomaterials* **31**, 9086-9091 (2010).
80. Zheng, D. et al. Topical delivery of siRNA-based spherical nucleic acid nanoparticle conjugates for gene regulation. *Proceedings of the National Academy of Sciences of the United States of America* **109**, 11975-11980 (2012).
81. Schulz, J. et al. Distribution of sunscreens on skin. *Advanced drug delivery reviews* **54 Suppl 1**, S157-163 (2002).
82. Dussert, A.S., Gooris, E. & Hemmerle, J. Characterization of the mineral content of a physical sunscreen emulsion and its distribution onto human stratum corneum. *International journal of cosmetic science* **19**, 119-129 (1997).
83. Jiang, S.J. et al. Biophysical and morphological changes in the stratum corneum lipids induced by UVB irradiation. *Journal of dermatological science* **44**, 29-36 (2006).
84. Dixit, N., Bali, V., Baboota, S., Ahuja, A. & Ali, J. Iontophoresis - an approach for controlled drug delivery: a review. *Current drug delivery* **4**, 1-10 (2007).
85. Ogura, M., Paliwal, S. & Mitragotri, S. Low-frequency sonophoresis: current status and future prospects. *Advanced drug delivery reviews* **60**, 1218-1223 (2008).
86. Brown, M.B., Martin, G.P., Jones, S.A. & Akomeah, F.K. Dermal and transdermal drug delivery systems: current and future prospects. *Drug delivery* **13**, 175-187 (2006).
87. Gill, H.S. et al. Selective removal of stratum corneum by microdermabrasion to increase skin permeability. *European journal of*

pharmaceutical sciences : official journal of the European Federation for Pharmaceutical Sciences **38**, 95-103 (2009).
88. Lee, W.R., Shen, S.C., Kuo-Hsien, W., Hu, C.H. & Fang, J.Y. Lasers and microdermabrasion enhance and control topical delivery of vitamin C. *The Journal of investigative dermatology* **121**, 1118-1125 (2003).
89. Thong, H.Y., Zhai, H. & Maibach, H.I. Percutaneous penetration enhancers: an overview. *Skin pharmacology and physiology* **20**, 272-282 (2007).
90. Giljohann, D.A., Seferos, D.S., Prigodich, A.E., Patel, P.C. & Mirkin, C.A. Gene regulation with polyvalent siRNA-nanoparticle conjugates. *Journal of the American Chemical Society* **131**, 2072-2073 (2009).
91. Rosi, N.L. et al. Oligonucleotide-modified gold nanoparticles for intracellular gene regulation. *Science* **312**, 1027-1030 (2006).
92. Glombitza, B. & Muller-Goymann, C.C. Influence of different ceramides on the structure of in vitro model lipid systems of the stratum corneum lipid matrix. *Chemistry and physics of lipids* **117**, 29-44 (2002).
93. Labouta, H.I., Thude, S. & Schneider, M. Setup for investigating gold nanoparticle penetration through reconstructed skin and comparison to published human skin data. *Journal of biomedical optics* **18**, 061218 (2013).
94. Nohynek, G.J., Antignac, E., Re, T. & Toutain, H. Safety assessment of personal care products/cosmetics and their ingredients. *Toxicology and applied pharmacology* **243**, 239-259 (2010).
95. Nohynek, G.J., Dufour, E.K. & Roberts, M.S. Nanotechnology, cosmetics and the skin: is there a health risk? *Skin pharmacology and physiology* **21**, 136-149 (2008).
96. Nohynek, G.J., Lademann, J., Ribaud, C. & Roberts, M.S. Grey goo on the skin? Nanotechnology, cosmetic and sunscreen safety. *Critical reviews in toxicology* **37**, 251-277 (2007).
97. Prow, T.W. et al. Nanoparticles and microparticles for skin drug delivery. *Advanced drug delivery reviews* **63**, 470-491 (2011).
98. Schneider, M., Stracke, F., Hansen, S. & Schaefer, U.F. Nanoparticles and their interactions with the dermal barrier. *Dermato-endocrinology* **1**, 197-206 (2009).
99. Semple, S. Dermal exposure to chemicals in the workplace: just how important is skin absorption? *Occupational and environmental medicine* **61**, 376-382 (2004).
100. Alkilany, A.M. & Murphy, C.J. Toxicity and cellular uptake of gold nanoparticles: what we have learned so far? *Journal of nanoparticle research : an interdisciplinary forum for nanoscale science and technology* **12**, 2313-2333 (2010).
101. Qiu, Y. et al. Surface chemistry and aspect ratio mediated cellular uptake of Au nanorods. *Biomaterials* **31**, 7606-7619 (2010).
102. Lacerda, S.H. et al. Interaction of gold nanoparticles with common human blood proteins. *ACS nano* **4**, 365-379 (2010).
103. Rausch, K., Reuter, A., Fischer, K. & Schmidt, M. Evaluation of nanoparticle aggregation in human blood serum. *Biomacromolecules* **11**, 2836-2839 (2010).
104. Maiorano, G. et al. Effects of cell culture media on the dynamic formation of protein-nanoparticle complexes and influence on the cellular response. *ACS nano* **4**, 7481-7491 (2010).
105. Verwey, E.J. Theory of the stability of lyophobic colloids. *The Journal of physical and colloid chemistry* **51**, 631-636 (1947).

106. Lundqvist, M. et al. Nanoparticle size and surface properties determine the protein corona with possible implications for biological impacts. *Proceedings of the National Academy of Sciences of the United States of America* **105**, 14265-14270 (2008).
107. Cedervall, T. et al. Detailed identification of plasma proteins adsorbed on copolymer nanoparticles. *Angewandte Chemie* **46**, 5754-5756 (2007).
108. Huang, R., Carney, R.P., Stellacci, F. & Lau, B.L. Protein-nanoparticle interactions: the effects of surface compositional and structural heterogeneity are scale dependent. *Nanoscale* **5**, 6928-6935 (2013).
109. van Landeghem, F.K. et al. Post-mortem studies in glioblastoma patients treated with thermotherapy using magnetic nanoparticles. *Biomaterials* **30**, 52-57 (2009).
110. Neubert, R.H. Potentials of new nanocarriers for dermal and transdermal drug delivery. *European journal of pharmaceutics and biopharmaceutics : official journal of Arbeitsgemeinschaft fur Pharmazeutische Verfahrenstechnik e.V* **77**, 1-2 (2011).
111. Irvine, J.D. et al. MDCK (Madin-Darby canine kidney) cells: A tool for membrane permeability screening. *Journal of pharmaceutical sciences* **88**, 28-33 (1999).
112. Liang, M. et al. Cellular uptake of densely packed polymer coatings on gold nanoparticles. *ACS nano* **4**, 403-413 (2010).
113. Lin, I.C. et al. Interaction of densely polymer-coated gold nanoparticles with epithelial Caco-2 monolayers. *Biomacromolecules* **12**, 1339-1348 (2011).
114. Chai, G.H. et al. Transport pathways of solid lipid nanoparticles across MDCK epithelial cell monolayer. *Molecular pharmaceutics* (2014).
115. Zhi-Cai, X., Yongmin, C. & Inn-Kyu, K. Immobilization of biomolecules on the surface of inorganic nanoparticles for biomedical applications. *Science and Technology of Advanced Materials* **11** (2010).
116. Guo, X. & Huang, L. Recent advances in nonviral vectors for gene delivery. *Accounts of chemical research* **45**, 971-979 (2012).
117. Murphy, C.J. et al. Anisotropic metal nanoparticles: Synthesis, assembly, and optical applications. *J Phys Chem B* **109**, 13857-13870 (2005).
118. Chen, X. & Wong, S. Cancer theranostics. (2014).
119. Jain, P.K., Huang, X., El-Sayed, I.H. & El-Sayed, M.A. Noble Metals on the Nanoscale: Optical and Photothermal Properties and Some Applications in Imaging, Sensing, Biology, and Medicine. *Accounts of chemical research* **41**, 1578-1586 (2008).
120. Sperling, R.A. & Parak, W.J. Surface modification, functionalization and bioconjugation of colloidal inorganic nanoparticles. *Philosophical transactions. Series A, Mathematical, physical, and engineering sciences* **368**, 1333-1383 (2010).
121. Delong, R.K. et al. Functionalized gold nanoparticles for the binding, stabilization, and delivery of therapeutic DNA, RNA, and other biological macromolecules. *Nanotechnology, science and applications* **3**, 53-63 (2010).
122. Han, G., Ghosh, P. & Rotello, V.M. Functionalized gold nanoparticles for drug delivery. *Nanomedicine (Lond)* **2**, 113-123 (2007).
123. Cheng, J., Gu, Y.J., Cheng, S.H. & Wong, W.T. Surface functionalized gold nanoparticles for drug delivery. *Journal of biomedical nanotechnology* **9**, 1362-1369 (2013).
124. Hunt, L.B. Gold Based Glass and Enamel Colors. *Endeavour* **5**, 61-67 (1981).

125. Freestone, I., Meeks, N., Sax, M. & Higgitt, C. The Lycurgus Cup — A Roman nanotechnology. *Gold Bull* **40**, 270-277 (2007).
126. Faraday, M. The Bakerian Lecture: Experimental Relations of Gold (and Other Metals) to Light. *Philosophical Transactions of the Royal Society of London* **147**, 145-181 (1857).
127. Turkevich, J., Stevenson, P.C. & Hillier, J. A study of the nucleation and growth processes in the synthesis of colloidal gold. *Discussions of the Faraday Society* **11**, 55-75 (1951).
128. Frens, G. Controlled Nucleation for Regulation of Particle-Size in Monodisperse Gold Suspensions. *Nature-Phys Sci* **241**, 20-22 (1973).
129. Kumar, S., Gandhi, K.S. & Kumar, R. Modeling of Formation of Gold Nanoparticles by Citrate Method. *Industrial and Engineering Chemistry Research* **46**, 3128-3136 (2006).
130. Haiss, W., Thanh, N.T.K., Aveyard, J. & Fernig, D.G. Determination of size and concentration of gold nanoparticles from UV-Vis spectra. *Anal Chem* **79**, 4215-4221 (2007).
131. Huang, X.H., Neretina, S. & El-Sayed, M.A. Gold Nanorods: From Synthesis and Properties to Biological and Biomedical Applications. *Adv Mater* **21**, 4880-4910 (2009).
132. Chen, H., Shao, L., Li, Q. & Wang, J. Gold nanorods and their plasmonic properties. *Chemical Society reviews* **42**, 2679-2724 (2013).
133. Pérez-Juste, J., Pastoriza-Santos, I., Liz-Marzán, L.M. & Mulvaney, P. Gold nanorods: Synthesis, characterization and applications. *Coordination Chemistry Reviews* **249**, 1870-1901 (2005).
134. Sau, T.K. & Murphy, C.J. Seeded high yield synthesis of short Au nanorods in aqueous solution. *Langmuir : the ACS journal of surfaces and colloids* **20**, 6414-6420 (2004).
135. Nikoobakht, B. & El-Sayed, M.A. Preparation and growth mechanism of gold nanorods (NRs) using seed-mediated growth method. *Chem Mater* **15**, 1957-1962 (2003).
136. Mie, G. Beiträge zur Optik trüber Medien, speziell kolloidaler Metallösungen. *ANDP Annalen der Physik* **330**, 377-445 (1908).
137. Johnson, P.B. & Christy, R.W. Optical Constants of the Noble Metals. *Phys Rev B* **6**, 4370-4379 (1972).
138. Link, S. & El-Sayed, M.A. Size and Temperature Dependence of the Plasmon Absorption of Colloidal Gold Nanoparticles. *The Journal of Physical Chemistry B* **103**, 4212-4217 (1999).
139. El-Brolossy, T.A. et al. Shape and size dependence of the surface plasmon resonance of gold nanoparticles studied by Photoacoustic technique. *Eur Phys J-Spec Top* **153**, 361-364 (2008).
140. Gans, R. Über die Form ultramikroskopischer Silberteilchen. *Annalen der Physik* **352**, 270-284 (1915).
141. Yu, Y.Y., Chang, S.S., Lee, C.L. & Wang, C.R.C. Gold nanorods: Electrochemical synthesis and optical properties. *J Phys Chem B* **101**, 6661-6664 (1997).
142. Karakoti, A.S., Das, S., Thevuthasan, S. & Seal, S. PEGylated inorganic nanoparticles. *Angewandte Chemie* **50**, 1980-1994 (2011).
143. Zanchet, D., Micheel, C.M., Parak, W.J., Gerion, D. & Alivisatos, A.P. Electrophoretic Isolation of Discrete Au Nanocrystal/DNA Conjugates. *Nano letters* **1**, 32-35 (2000).
144. Reinhard, B.M., Sheikholeslami, S., Mastroianni, A., Alivisatos, A.P. & Liphardt, J. Use of plasmon coupling to reveal the dynamics of DNA bending and cleavage by single EcoRV restriction enzymes. *Proceedings*

of the National Academy of Sciences of the United States of America **104**, 2667-2672 (2007).
145. Kinnear, C. et al. Gold Nanorods: Controlling Their Surface Chemistry and Complete Detoxification by a Two-Step Place Exchange. *Angewandte Chemie-International Edition* **52**, 1934-1938 (2013).
146. Davis, F.F. The origin of pegnology. *Advanced drug delivery reviews* **54**, 457-458 (2002).
147. Wang, A.Z. et al. Biofunctionalized targeted nanoparticles for therapeutic applications. *Expert opinion on biological therapy* **8**, 1063-1070 (2008).
148. Lévy, R. et al. Rational and Combinatorial Design of Peptide Capping Ligands for Gold Nanoparticles. *Journal of the American Chemical Society* **126**, 10076-10084 (2004).
149. Bellino, M.G., Calvo, E.J. & Gordillo, G. Adsorption kinetics of charged thiols on gold nanoparticles. *Physical Chemistry Chemical Physics* **6**, 424-428 (2004).
150. Gonzalez-Mariscal, L., Chavez de Ramirez, B. & Cereijido, M. Tight junction formation in cultured epithelial cells (MDCK). *The Journal of membrane biology* **86**, 113-125 (1985).
151. Simmons, N.L. Cultured Monolayers of Mdck Cells - a Novel Model System for the Study of Epithelial Development and Function. *Gen Pharmacol* **13**, 287-291 (1982).
152. Furuse, M. et al. Claudin-based tight junctions are crucial for the mammalian epidermal barrier: a lesson from claudin-1-deficient mice. *The Journal of cell biology* **156**, 1099-1111 (2002).
153. Xiong, H. & Gendelman, H.E. (2014).
154. Turkevich, J., Stevenson, P.C. & Hillier, J. The Formation of Colloidal Gold. *The Journal of Physical Chemistry* **57**, 670-673 (1953).
155. Haiss, W., Thanh, N.T., Aveyard, J. & Fernig, D.G. Determination of size and concentration of gold nanoparticles from UV-vis spectra. *Anal Chem* **79**, 4215-4221 (2007).
156. Lee, J.S., Stoeva, S.I. & Mirkin, C.A. DNA-induced size-selective separation of mixtures of gold nanoparticles. *Journal of the American Chemical Society* **128**, 8899-8903 (2006).
157. Ji, X. et al. Size control of gold nanocrystals in citrate reduction: the third role of citrate. *Journal of the American Chemical Society* **129**, 13939-13948 (2007).
158. Liu, X. et al. A study on gold nanoparticle synthesis using oleylamine as both reducing agent and protecting ligand. *Journal of nanoscience and nanotechnology* **7**, 3126-3133 (2007).
159. Kelly, S. et al. Gene transfer of HSP72 protects cornu ammonis 1 region of the hippocampus neurons from global ischemia: Influence of Bcl-2. *Ann Neurol* **52**, 160-167 (2002).
160. Polte, J. et al. Nucleation and growth of gold nanoparticles studied via in situ small angle X-ray scattering at millisecond time resolution. *ACS nano* **4**, 1076-1082 (2010).
161. Zabetakis, K., Ghann, W.E., Kumar, S. & Daniel, M.C. Effect of high gold salt concentrations on the size and polydispersity of gold nanoparticles prepared by an extended Turkevich-Frens method. *Gold Bull* **45**, 203-211 (2012).
162. Jain, P.K., Lee, K.S., El-Sayed, I.H. & El-Sayed, M.A. Calculated absorption and scattering properties of gold nanoparticles of different size, shape, and composition: Applications in biological imaging and biomedicine. *J Phys Chem B* **110**, 7238-7248 (2006).

163. Kreibig, U.V.M. Optical properties of metal clusters, Vol. 25. (Springer, Berlin; 1995).
164. Pego, P.P., L. in The supramolecular chemistry of organic-inorganic hybrid materials. (ed. K.M.n.-M.n.e. Rurack, R.) 113-154 (John Wiley & Sons, Inc, Hoboken, N.J.; 2010).
165. Cortie, M.B.M., A. in Gold chemistry : applications and future directions in the life sciences. (ed. F. Mohr) 321-343 (Wiley-VCH, Weinheim; 2009).
166. Schmid, G. & Lehnert, A. The Complexation of Gold Colloids. *Angew Chem Int Edit* **28**, 780-781 (1989).
167. Wen, F., Englert, U., Gutrath, B. & Simon, U. Crystal structure, electrochemical and optical properties of [Au-9(PPh3)(8)](NO3)(3). *Eur J Inorg Chem*, 106-111 (2008).
168. Jewell, A.D., Sykes, E.C. & Kyriakou, G. Molecular-scale surface chemistry of a common metal nanoparticle capping agent: triphenylphosphine on Au(111). *ACS nano* **6**, 3545-3552 (2012).
169. Burns, C., Spendel, W.U., Puckett, S. & Pacey, G.E. Solution ionic strength effect on gold nanoparticle solution color transition. *Talanta* **69**, 873-876 (2006).
170. Loweth, C.J., Caldwell, W.B., Peng, X.G., Alivisatos, A.P. & Schultz, P.G. DNA-based assembly of gold nanocrystals. *Angewandte Chemie-International Edition* **38**, 1808-1812 (1999).
171. Perez-Juste, J., Liz-Marzan, L.M., Carnie, S., Chan, D.Y.C. & Mulvaney, P. Electric-field-directed growth of gold nanorods in aqueous surfactant solutions. *Adv Funct Mater* **14**, 571-579 (2004).
172. Jain, R.K. Molecular regulation of vessel maturation. *Nature medicine* **9**, 685-693 (2003).
173. Chithrani, B.D., Ghazani, A.A. & Chan, W.C.W. Determining the Size and Shape Dependence of Gold Nanoparticle Uptake into Mammalian Cells. *Nano letters* **6**, 662-668 (2006).
174. Sandhu, K.K., McIntosh, C.M., Simard, J.M., Smith, S.W. & Rotello, V.M. Gold nanoparticle-mediated transfection of mammalian cells. *Bioconjugate chemistry* **13**, 3-6 (2002).
175. Woolf, T.M., Jennings, C.G., Rebagliati, M. & Melton, D.A. The stability, toxicity and effectiveness of unmodified and phosphorothioate antisense oligodeoxynucleotides in Xenopus oocytes and embryos. *Nucleic acids research* **18**, 1763-1769 (1990).
176. Tkachenko, A.G. et al. Multifunctional gold nanoparticle-peptide complexes for nuclear targeting. *Journal of the American Chemical Society* **125**, 4700-4701 (2003).
177. El-Sayed, I.H., Huang, X. & El-Sayed, M.A. Surface plasmon resonance scattering and absorption of anti-EGFR antibody conjugated gold nanoparticles in cancer diagnostics: applications in oral cancer. *Nano letters* **5**, 829-834 (2005).
178. Giljohann, D.A. et al. Gold nanoparticles for biology and medicine. *Angewandte Chemie* **49**, 3280-3294 (2010).
179. Euliss, L.E., DuPont, J.A., Gratton, S. & DeSimone, J. Imparting size, shape, and composition control of materials for nanomedicine. *Chemical Society reviews* **35**, 1095-1104 (2006).
180. Owens, D.E., 3rd & Peppas, N.A. Opsonization, biodistribution, and pharmacokinetics of polymeric nanoparticles. *International journal of pharmaceutics* **307**, 93-102 (2006).
181. Park, J.H. et al. Polymeric nanomedicine for cancer therapy. *Prog Polym Sci* **33**, 113-137 (2008).

182. Howard, M.D., Jay, M., Dziublal, T.D. & Lu, X.L. PEGylation of nanocarrier drug delivery systems: State of the art. *Journal of biomedical nanotechnology* **4**, 133-148 (2008).
183. Joralemon, M.J., McRae, S. & Emrick, T. PEGylated polymers for medicine: from conjugation to self-assembled systems. *Chemical communications* **46**, 1377-1393 (2010).
184. Jayagopal, A., Russ, P.K. & Haselton, F.R. Surface engineering of quantum dots for in vivo vascular imaging. *Bioconjugate chemistry* **18**, 1424-1433 (2007).
185. Haynes, W.M.L.D.R. CRC handbook of chemistry and physics : a ready-reference book of chemical and physical data. (CRC Press, Boca Raton, Fla.; 2011).
186. Kinnear, C. et al. Gold nanorods: controlling their surface chemistry and complete detoxification by a two-step place exchange. *Angewandte Chemie* **52**, 1934-1938 (2013).
187. Malcher, T. & Gzyl-Malcher, B. Influence of polymer-surfactant aggregates on fluid flow. *Bioelectrochemistry* **87**, 42-49 (2012).
188. Qiu, L.G., Cheng, M.J., Xie, A.J. & Shen, Y.H. Study on the viscosity of cationic gemini surfactant-nonionic polymer complex in water. *Journal of colloid and interface science* **278**, 40-43 (2004).
189. Xia, X.H. et al. Quantifying the Coverage Density of Poly(ethylene glycol) Chains on the Surface of Gold Nanostructures. *ACS nano* **6**, 512-522 (2012).
190. Khlebtsov, B.N. & Khlebtsov, N.G. On the measurement of gold nanoparticle sizes by the dynamic light scattering method. *Colloid Journal* **73**, 118-127 (2011).
191. Zimbone, M. et al. Dynamic light scattering on bioconjugated laser generated gold nanoparticles. *PloS one* **9**, e89048 (2014).
192. Kanjanawarut, R., Yuan, B. & XiaoDi, S. UV-vis spectroscopy and dynamic light scattering study of gold nanorods aggregation. *Nucleic acid therapeutics* **23**, 273-280 (2013).
193. (The American Chemical Society.
194. Berne, B.J. & Pecora, R. Dynamic light scattering : with applications to chemistry, biology, and physics. (Wiley, New York; 1976).
195. Wang, C., Chen, Y., Wang, T., Ma, Z. & Su, Z. Biorecognition-Driven Self-Assembly of Gold Nanorods: A Rapid and Sensitive Approach toward Antibody Sensing. *Chem Mater* **19**, 5809-5811 (2007).
196. Liu, H., Pierre-Pierre, N. & Huo, Q. Dynamic light scattering for gold nanorod size characterization and study of nanorodprotein interactions. *Gold Bull Gold Bulletin* **45**, 187-195 (2012).
197. Levy, R. et al. Rational and combinatorial design of peptide capping ligands for gold nanoparticles. *Journal of the American Chemical Society* **126**, 10076-10084 (2004).
198. Levy, R. Peptide-capped gold nanoparticles: Towards artificial proteins. *Chembiochem* **7**, 1141-1145 (2006).
199. Levy, R., Shaheen, U., Cesbron, Y. & See, V. Gold nanoparticles delivery in mammalian live cells: a critical review. *Nano reviews* **1** (2010).
200. Levy, R. et al. Rational and combinatorial design of peptide capping Ligands for gold nanoparticles. *Journal of the American Chemical Society* **126**, 10076-10084 (2004).
201. Levy, R. et al. A generic approach to monofunctionalized protein-like gold nanoparticles based on immobilized metal ion affinity chromatography. *Chembiochem* **7**, 592-594 (2006).

202. Copolovici, D.M., Langel, K., Eriste, E. & Langel, U. Cell-penetrating peptides: design, synthesis, and applications. *ACS nano* **8**, 1972-1994 (2014).
203. Heitz, F., Morris, M.C. & Divita, G. Twenty years of cell-penetrating peptides: from molecular mechanisms to therapeutics. *British journal of pharmacology* **157**, 195-206 (2009).
204. Desai, P., Patlolla, R.R. & Singh, M. Interaction of nanoparticles and cell-penetrating peptides with skin for transdermal drug delivery. *Mol Membr Biol* **27**, 247-259 (2010).
205. Nasrollahi, S.A., Taghibiglou, C., Azizi, E. & Farboud, E.S. Cell-penetrating peptides as a novel transdermal drug delivery system. *Chemical biology & drug design* **80**, 639-646 (2012).
206. Torchilin, V.P. Cell penetrating peptide-modified pharmaceutical nanocarriers for intracellular drug and gene delivery. *Biopolymers* **90**, 604-610 (2008).
207. Rothbard, J.B. et al. Conjugation of arginine oligomers to cyclosporin A facilitates topical delivery and inhibition of inflammation. *Nature medicine* **6**, 1253-1257 (2000).
208. Gamrad, L. et al. Charge Balancing of Model Gold-Nanoparticle-Peptide Conjugates Controlled by the Peptide's Net Charge and the Ligand to Nanoparticle Ratio. *J Phys Chem C* **118**, 10302-10313 (2014).
209. Muto, H., Yamada, K., Miyajima, K. & Mafune, F. Estimation of surface oxide on surfactant-free gold nanoparticles laser-ablated in water. *J Phys Chem C* **111**, 17221-17226 (2007).
210. Luo, F.R., Paranjpe, P.V., Guo, A., Rubin, E. & Sinko, P. Intestinal transport of irinotecan in Caco-2 cells and MDCK II cells overexpressing efflux transporters Pgp, cMOAT, and MRP1. *Drug metabolism and disposition: the biological fate of chemicals* **30**, 763-770 (2002).
211. Volpe, D.A. Drug-permeability and transporter assays in Caco-2 and MDCK cell lines. *Future medicinal chemistry* **3**, 2063-2077 (2011).
212. Xiao, Y. et al. A 96-well efflux assay to identify ABCG2 substrates using a stably transfected MDCK II cell line. *Molecular pharmaceutics* **3**, 45-54 (2006).
213. Hidalgo, I.J. Assessing the absorption of new pharmaceuticals. *Current topics in medicinal chemistry* **1**, 385-401 (2001).
214. Kitamura, S., Maeda, K., Wang, Y. & Sugiyama, Y. Involvement of multiple transporters in the hepatobiliary transport of rosuvastatin. *Drug metabolism and disposition: the biological fate of chemicals* **36**, 2014-2023 (2008).
215. Elsby, R., Surry, D.D., Smith, V.N. & Gray, A.J. Validation and application of Caco-2 assays for the in vitro evaluation of development candidate drugs as substrates or inhibitors of P-glycoprotein to support regulatory submissions. *Xenobiotica; the fate of foreign compounds in biological systems* **38**, 1140-1164 (2008).
216. Foye, W.O., Lemke, T.L. & Williams, D.A. Foye's principles of medicinal chemistry. (Lippincott Williams & Wilkins, Philadelphia; 2008).
217. Cho, M., Thompson, D., Cramer, C., Vidmar, T. & Scieszka, J. The Madin Darby Canine Kidney (MDCK) Epithelial Cell Monolayer as a Model Cellular Transport Barrier. *Pharmaceutical research* **6**, 71-77 (1989).
218. Cho, M.J., Thompson, D.P., Cramer, C.T., Vidmar, T.J. & Scieszka, J.F. The Madin Darby Canine Kidney (Mdck) Epithelial-Cell Monolayer as a Model Cellular-Transport Barrier. *Pharmaceutical research* **6**, 71-77 (1989).

219. Leung, S.S., Mijalkovic, J., Borrelli, K. & Jacobson, M.P. Testing physical models of passive membrane permeation. *Journal of chemical information and modeling* **52**, 1621-1636 (2012).
220. Rothen-Rutishauser, B., Kramer, S.D., Braun, A., Gunthert, M. & Wunderli-Allenspach, H. MDCK cell cultures as an epithelial in vitro model: Cytoskeleton and tight junctions as indicators for the definition of age-related stages by confocal microscopy. *Pharmaceutical research* **15**, 964-971 (1998).
221. Matter, K. & Balda, M.S. Functional analysis of tight junctions. *Methods* **30**, 228-234 (2003).
222. Collares-Buzato, C.B., Jepson, M.A., Simmons, N.L. & Hirst, B.H. Increased tyrosine phosphorylation causes redistribution of adherens junction and tight junction proteins and perturbs paracellular barrier function in MDCK epithelia. *European journal of cell biology* **76**, 85-92 (1998).
223. Chen, Y., Lu, Q., Schneeberger, E.E. & Goodenough, D.A. Restoration of tight junction structure and barrier function by down-regulation of the mitogen-activated protein kinase pathway in ras-transformed Madin-Darby canine kidney cells. *Molecular biology of the cell* **11**, 849-862 (2000).
224. Shibayama, M. et al. Disruption of MDCK cell tight junctions by the free-living amoeba Naegleria fowleri. *Microbiology* **159**, 392-401 (2013).
225. Lai-Cheong, J.E., Arita, K. & McGrath, J.A. Genetic diseases of junctions. *The Journal of investigative dermatology* **127**, 2713-2725 (2007).
226. Yuki, T. et al. Characterization of Tight Junctions and Their Disruption by UVB in Human Epidermis and Cultured Keratinocytes. *Journal of Investigative Dermatology* **131**, 744-752 (2011).
227. Buchert, M., Turksen, K. & Hollande, F. Methods to examine tight junction physiology in cancer stem cells: TEER, paracellular permeability, and dilution potential measurements. *Stem cell reviews* **8**, 1030-1034 (2012).
228. Mauro, F., Tejal, D. & Sangeeta, B. BioMEMS and Biomedical Nanotechnology Volume III Therapeutic Micro/Nanotechnology. (2007).
229. Loretz, B. & Bernkop-Schnurch, A. In vitro cytotoxicity testing of non-thiolated and thiolated chitosan nanoparticles for oral gene delivery. *Nanotoxicology* **1**, 139-148 (2007).
230. Ludwig, T. et al. The electrical resistance breakdown assay determines the role of proteinases in tumor cell invasion. *American journal of physiology. Renal physiology* **283**, F319-327 (2002).
231. Roman, L.M., Scharm, A. & Howell, K.E. Immunoselection of Stably Transformed Mdck Cells Expressing the Vesicular Stomatitis-Virus G-Protein at the Basolateral Surface. *Experimental cell research* **175**, 376-387 (1988).
232. Rosenblatt, J., Raff, M.C. & Cramer, L.P. An epithelial cell destined for apoptosis signals its neighbors to extrude it by an actin- and myosin-dependent mechanism. *Curr Biol* **11**, 1847-1857 (2001).
233. Yang, K. & Ma, Y.Q. Computer simulation of the translocation of nanoparticles with different shapes across a lipid bilayer. *Nature nanotechnology* **5**, 579-583 (2010).
234. Chithrani, B.D., Ghazani, A.A. & Chan, W.C. Determining the size and shape dependence of gold nanoparticle uptake into mammalian cells. *Nano letters* **6**, 662-668 (2006).

235. Truong, N.P., Whittaker, M.R., Mak, C.W. & Davis, T.P. The importance of nanoparticle shape in cancer drug delivery. *Expert opinion on drug delivery* **12**, 129-142 (2015).
236. Scott, R.C., Corrigan, M.A., Smith, F. & Mason, H. The influence of skin structure on permeability: an intersite and interspecies comparison with hydrophilic penetrants. *The Journal of investigative dermatology* **96**, 921-925 (1991).
237. Pasparakis, M., Haase, I. & Nestle, F.O. Mechanisms regulating skin immunity and inflammation. *Nature reviews. Immunology* **14**, 289-301 (2014).
238. Treuting, P.M. & Dintzis, S.M. (Academic, Oxford; 2012).
239. Egawa, G., Osawa, M., Uemura, A., Miyachi, Y. & Nishikawa, S. Transient expression of ephrin b2 in perinatal skin is required for maintenance of keratinocyte homeostasis. *The Journal of investigative dermatology* **129**, 2386-2395 (2009).
240. Hedrich, H.J. & Bullock, G.R. The laboratory mouse. (Elsevier Academic Press, Amsterdam; Boston; 2004).
241. Riviere, J.E., Bowman, K.F. & Monteiro-Riviere, N.A. On the definition of viability in isolated perfused skin preparations. *The British journal of dermatology* **116**, 739-741 (1987).
242. Monteiro-Riviere, N.A. Altered epidermal morphology secondary to lidocaine iontophoresis: in vivo and in vitro studies in porcine skin. *Fundamental and applied toxicology : official journal of the Society of Toxicology* **15**, 174-185 (1990).
243. Bommannan, D., Potts, R.O. & Guy, R.H. Examination of stratum corneum barrier function in vivo by infrared spectroscopy. *The Journal of investigative dermatology* **95**, 403-408 (1990).
244. Escobar-Chavez, J.J., Quintanar-Guerrero, D. & Ganem-Quintanar, A. In vivo skin permeation of sodium naproxen formulated in pluronic F-127 gels: effect of Azone and Transcutol. *Drug development and industrial pharmacy* **31**, 447-454 (2005).
245. Berardesca, E. & Maibach, H.I. Racial differences in pharmacodynamic response to nicotinates in vivo in human skin: black and white. *Acta dermato-venereologica* **70**, 63-66 (1990).
246. Pinkus, H. Examination of the epidermis by the strip method of removing horny layers. I. Observations on thickness of the horny layer, and on mitotic activity after stripping. *The Journal of investigative dermatology* **16**, 383-386 (1951).
247. Schwarb, F.P., Gabard, B., Rufli, T. & Surber, C. Percutaneous absorption of salicylic acid in man after topical administration of three different formulations. *Dermatology* **198**, 44-51 (1999).
248. Rougier, A., Lotte, C. & Maibach, H.I. In vivo percutaneous penetration of some organic compounds related to anatomic site in humans: predictive assessment by the stripping method. *Journal of pharmaceutical sciences* **76**, 451-454 (1987).
249. Schwindt, D.A., Wilhelm, K.P. & Maibach, H.I. Water diffusion characteristics of human stratum corneum at different anatomical sites in vivo. *The Journal of investigative dermatology* **111**, 385-389 (1998).
250. Greene, R.S., Downing, D.T., Pochi, P.E. & Strauss, J.S. Anatomical variation in the amount and composition of human skin surface lipid. *The Journal of investigative dermatology* **54**, 240-247 (1970).
251. Berardesca, E., Pirot, F., Singh, M. & Maibach, H. Differences in stratum corneum pH gradient when comparing white Caucasian and black

African-American skin. *The British journal of dermatology* **139**, 855-857 (1998).
252. Reed, J.T., Ghadially, R. & Elias, P.M. Skin type, but neither race nor gender, influence epidermal permeability barrier function. *Archives of dermatology* **131**, 1134-1138 (1995).
253. Loffler, H., Dreher, F. & Maibach, H.I. Stratum corneum adhesive tape stripping: influence of anatomical site, application pressure, duration and removal. *The British journal of dermatology* **151**, 746-752 (2004).
254. Breternitz, M., Flach, M., Prassler, J., Elsner, P. & Fluhr, J.W. Acute barrier disruption by adhesive tapes is influenced by pressure, time and anatomical location: integrity and cohesion assessed by sequential tape stripping. A randomized, controlled study. *The British journal of dermatology* **156**, 231-240 (2007).
255. Tokumura, F., Homma, T., Tomiya, T., Kobayashi, Y. & Matsuda, T. Properties of pressure-sensitive adhesive tapes with soft adhesives to human skin and their mechanism. *Skin research and technology : official journal of International Society for Bioengineering and the Skin* **13**, 211-216 (2007).
256. Weigmann, H., Lademann, J., Meffert, H., Schaefer, H. & Sterry, W. Determination of the horny layer profile by tape stripping in combination with optical spectroscopy in the visible range as a prerequisite to quantify percutaneous absorption. *Skin pharmacology and applied skin physiology* **12**, 34-45 (1999).
257. Shanmugam, S. et al. Physicochemical characterization and skin permeation of liposome formulations containing clindamycin phosphate. *Arch Pharm Res* **32**, 1067-1075 (2009).
258. Dasgupta, S., Auth, T. & Gompper, G. Shape and orientation matter for the cellular uptake of nonspherical particles. *Nano letters* **14**, 687-693 (2014).
259. Perrault, S.D., Walkey, C., Jennings, T., Fischer, H.C. & Chan, W.C. Mediating tumor targeting efficiency of nanoparticles through design. *Nano letters* **9**, 1909-1915 (2009).
260. Prow, T.W. et al. Quantum dot penetration into viable human skin. *Nanotoxicology* **6**, 173-185 (2012).
261. Russ, J.C. Fundamentals of Energy Dispersive X-ray Analysis. (Butterworth-Heinemann, 1984).
262. Chen, G., Qiu, H., Prasad, P.N. & Chen, X. Upconversion nanoparticles: design, nanochemistry, and applications in theranostics. *Chemical reviews* **114**, 5161-5214 (2014).
263. Heuer-Jungemann, A., Harimech, P.K., Brown, T. & Kanaras, A.G. Gold nanoparticles and fluorescently-labelled DNA as a platform for biological sensing. *Nanoscale* **5**, 9503-9510 (2013).
264. Vo-Dinh, T. et al. Plasmonic nanoprobes: from chemical sensing to medical diagnostics and therapy. *Nanoscale* **5**, 10127-10140 (2013).
265. Webb, J.A. & Bardhan, R. Emerging advances in nanomedicine with engineered gold nanostructures. *Nanoscale* **6**, 2502-2530 (2014).
266. Chou, L.Y., Zagorovsky, K. & Chan, W.C. DNA assembly of nanoparticle superstructures for controlled biological delivery and elimination. *Nature nanotechnology* **9**, 148-155 (2014).
267. Comin, A. & Manna, L. New materials for tunable plasmonic colloidal nanocrystals. *Chemical Society reviews* **43**, 3957-3975 (2014).
268. Heuer-Jungemann, A., Kirkwood, R., El-Sagheer, A.H., Brown, T. & Kanaras, A.G. Copper-free click chemistry as an emerging tool for the

programmed ligation of DNA-functionalised gold nanoparticles. *Nanoscale* **5**, 7209-7212 (2013).
269. Li, N., Zhao, P. & Astruc, D. Anisotropic gold nanoparticles: synthesis, properties, applications, and toxicity. *Angewandte Chemie* **53**, 1756-1789 (2014).
270. Lu, Z. & Yin, Y. Colloidal nanoparticle clusters: functional materials by design. *Chemical Society reviews* **41**, 6874-6887 (2012).
271. Luo, Z., Zheng, K. & Xie, J. Engineering ultrasmall water-soluble gold and silver nanoclusters for biomedical applications. *Chemical communications* **50**, 5143-5155 (2014).
272. Pelaz, B. et al. Tailoring the synthesis and heating ability of gold nanoprisms for bioapplications. *Langmuir : the ACS journal of surfaces and colloids* **28**, 8965-8970 (2012).
273. Kim, S.T., Saha, K., Kim, C. & Rotello, V.M. The role of surface functionality in determining nanoparticle cytotoxicity. *Accounts of chemical research* **46**, 681-691 (2013).
274. Mahmoudi, M. et al. Interaction of stable colloidal nanoparticles with cellular membranes. *Biotechnology advances* **32**, 679-692 (2014).
275. Huhn, D. et al. Polymer-coated nanoparticles interacting with proteins and cells: focusing on the sign of the net charge. *ACS nano* **7**, 3253-3263 (2013).
276. Pillai, P.P., Huda, S., Kowalczyk, B. & Grzybowski, B.A. Controlled pH stability and adjustable cellular uptake of mixed-charge nanoparticles. *Journal of the American Chemical Society* **135**, 6392-6395 (2013).
277. Walkey, C.D. et al. Protein corona fingerprinting predicts the cellular interaction of gold and silver nanoparticles. *ACS nano* **8**, 2439-2455 (2014).
278. Yang, J.A., Lohse, S.E. & Murphy, C.J. Tuning cellular response to nanoparticles via surface chemistry and aggregation. *Small* **10**, 1642-1651 (2014).
279. Zhao, F. et al. Cellular uptake, intracellular trafficking, and cytotoxicity of nanomaterials. *Small* **7**, 1322-1337 (2011).
280. Haniffa, M. et al. Differential rates of replacement of human dermal dendritic cells and macrophages during hematopoietic stem cell transplantation. *The Journal of experimental medicine* **206**, 371-385 (2009).
281. Lane, M.E. Nanoparticles and the skin--applications and limitations. *Journal of microencapsulation* **28**, 709-716 (2011).
282. Niidome, T., Nakashima, K., Takahashi, H. & Niidome, Y. Preparation of primary amine-modified gold nanoparticles and their transfection ability into cultivated cells. *Chemical communications*, 1978-1979 (2004).